

**A COMPUTATIONAL APPROACH TO THE PREDICTION OF  
WHEEL WEAR PROFILES**

by

**Bor-Tsuen Wang**

Thesis submitted to the Faculty of the  
Virginia Polytechnic Institute and State University  
in partial fulfillment of the requirements for the degree of  
Master of Science  
in  
Mechanical Engineering

APPROVED:

---

Dr. Robert H. Pries, Chairman

---

Dr. Norman S. Eiss

---

Dr. E. K. Dimitriadis

May 30, 1988

Blacksburg, Virginia

**A COMPUTATIONAL APPROACH TO THE PREDICTION OF  
WHEEL WEAR PROFILES**

by

**Bor-Tsuen Wang**

**Dr. Robert H. Fries, Chairman**

**Department of Mechanical Engineering**

**(ABSTRACT)**

Wheel wear profiles are interesting for both economic and performance reasons. A good wheel profile design should be able to resist wear and to allow stable vehicle running. The ability to resist wear reduces the wheel reprofiling and replacement cost. The ability to allow stable vehicle running is important for safety and ride quality.

In this work, a wear model based upon the work done in the wheel/rail contact patch is used to predict wheel wear profiles. The effects of train dynamic response, random rail alignment and the nonlinearity of wheel/rail contact geometry are included.

The distribution of contact patch work is obtained by a discretized method and applied to the wheel wear problem. Using the contact patch work wear model, consecutive wheel wear profiles for tread contact and slight flange contact are predicted. These analytical wear profiles match well with experimental results and other analytical approaches.

## Acknowledgements

I am greatly indebted to my advisor, Dr. Robert H. Fries, for his guidance and patient assistance. Without his invaluable directions and suggestions, I would not be able to complete this work. I am very grateful for his help.

I also thank Dr. Norman S. Eiss and Dr. E. K. Dimitriadis for serving on my graduate committee. I like to acknowledge their helpful discussion and kind support.

... deserves special thanks for his help in preparing the figures which appear in this thesis. I like to thank ..., and ... for their comments and editing on the thesis. I would like to express my gratitude to my fellows in the Mechanical Engineering Department for their friendship.

I extend my gratitude to the staff in User Services and in Writing Center for their invaluable assistance on solving the computer problems and their patience to correct my writing.

Finally, I wish to thank my parents, ... and ..., and my family for their support and encouragement from overseas.

# Table of Contents

<b>Chapter 1 : Introduction</b> .....	<b>1</b>
1.1 Wear Problem in Wheel/Rail Contact .....	1
1.2 Literature Review .....	2
1.3 Scope of the Current Work .....	7
<b>Chapter 2 : The Wheel/Rail Rolling Contact Problem</b> .....	<b>9</b>
2.1 Determination of Wheel/Rail Geometric Constraint .....	10
2.2 Definition of Creepage .....	18
2.3 The Hertzian Contact Problem .....	20
2.4 Creep Forces and Moment in Rolling Contact .....	21
2.5 Study of Slip/Adhesion Region at the Contact Patch .....	30
Summary .....	41
<b>Chapter 3 : Analytical Dynamics Model for the Study of Wear Process</b> .....	<b>42</b>
3.1 Nomenclature .....	43
3.2 Wheelset Equations of Motion .....	47
3.3 Five-Degree-of-Freedom Half-Car Model .....	49

Nonlinear Coulomb Friction .....	54
3.4 Random Rail Alignment Generation .....	59
3.5 Solution Method .....	61
3.6 Result of Dynamic Response .....	65
Summary .....	69
<b>Chapter 4 : Wear Prediction in Wheel/Rail Rolling Contact .....</b>	<b>73</b>
4.1 Wear Models .....	74
Archard's Model .....	74
Contact Patch Work Model .....	74
4.2 Application of Contact Patch Work Model to Wheel/Rail Rolling Contact .....	75
Computation of Work Done in the Contact Patch .....	75
Computation of Wear Volume .....	79
Application to Wheel/Rail Rolling Contact Problem .....	80
4.3 Expression of Wear Rate .....	84
4.4 Relation Between Archard's Model and Contact Patch Work Model .....	85
Summary .....	90
<b>Chapter 5 : Wear Computation Method and Results .....</b>	<b>92</b>
5.1 Wear Computation method .....	93
5.2 Wear in Tread Contact .....	95
5.3 Wear in Flange Contact .....	103
Summary .....	112
<b>Chapter 6 : Conclusion and Recommendation .....</b>	<b>114</b>
6.1 Conclusion .....	114
6.2 Recommendations .....	116

<b>Appendix A. Derivation of Equations of Motion for a Wheelset</b> .....	<b>118</b>
A.1 Nomenclature .....	118
A.2 Coordinate System of the Wheelset .....	120
A.3 Wheelset Equations .....	123
<b>Appendix B. Derivation of Creepage and Spin for a Wheelset</b> .....	<b>134</b>
<b>Appendix C. Derivation of Equations of Motion for the 5 d.o.f. Half-Car Model</b> .....	<b>139</b>
Kinetic Energy .....	140
Potential Energy .....	142
Dissipative Energy .....	143
Generalized Force .....	145
<b>References:</b> .....	<b>151</b>
<b>Vita</b> .....	<b>158</b>

## List of Illustrations

Figure 1. Wheel/rail tribosystem (Kalousek et al., 1983) . . . . .	3
Figure 2. Summary of wear indexes (Nagurka, 1982) . . . . .	6
Figure 3. AAR 1:20 wheel profile (Cooperrider et al., 1981) . . . . .	11
Figure 4. Heumann wheel profile (Elkins et al., 1986) . . . . .	12
Figure 5. 132-RE rail profile (AREA, 1984) . . . . .	13
Figure 6. Wheel/rail contact relationships . . . . .	14
Figure 7. Effect of lateral and yaw displacement on wheel/rail contact . . . . .	15
Figure 8. Wheel/rail geometric constraint functions (WHRAILA by Heller and Cooperrider, 1977a) . . . . .	16
Figure 9. Wheel/rail geometry constraint functions (continue) . . . . .	17
Figure 10. Force and moment acting on contact area, . . . . .	23
Figure 11. Local creep force and slip at the contact patch . . . . .	31
Figure 12. Slip/adhesion region related to creep force (Nagurka, 1983) . . . . .	33
Figure 13. Slip/adhesion regions for zero spin creepage . . . . .	34
Figure 14. Slip/adhesion regions for zero lateral creepage . . . . .	35
Figure 15. Slip/adhesion regions for zero longitudinal creepage . . . . .	36
Figure 16. Slip/adhesion regions for pure spin creepage . . . . .	38
Figure 17. Distribution of creep force/moment, slip/spin, and work done for partial slip example . . . . .	39
Figure 18. Distribution of creep force/moment, slip/spin, and work done for full slip example . . . . .	40
Figure 19. Rear view of a wheelset . . . . .	48

Figure 20. Configuration of the 80-ton open hopper car .....	50
Figure 21. Schematic of 5 d.o.f. half-car model .....	51
Figure 22. Characteristic curve for Coulomb friction .....	55
Figure 23. Scheme of slider model for rotation Coulomb friction .....	56
Figure 24. Illustration of truck irregularity (Garg and Dukkipati, 1984) .....	60
Figure 25. Truck lateral displacement and rail lateral alignment (45 mph) .....	66
Figure 26. Front and rear wheelset lateral displacements (45 mph) .....	67
Figure 27. Vertical displacement and roll angle of the wheelset (45 mph) .....	68
Figure 28. Truck lateral displacement and rail lateral alignment (80 mph) .....	70
Figure 29. Front and rear wheelset lateral displacements (80 mph) .....	71
Figure 30. Illustration of the subscript of contact patch for wheel/rail contact .....	81
Figure 31. Range of wear coefficient for typical wear mechanisms (Rabinowicz, 1980) ..	86
Figure 32. A collection of wear index coefficient and wear coefficient .....	89
Figure 33. Flow chart of the simulation of wheel wear process .....	93
Figure 34. The lateral position of wheelsets and final wheel wear profiles (45,AAR,empty,T)	96
Figure 35. The consecutive wear profiles of the left wheels (45,AAR,empty,T) .....	97
Figure 36. The consecutive wear profiles of the right wheels (45,AAR,empty,T) .....	98
Figure 37. The consecutive wheel wear profiles of Davila's prediction (Davila, 1986) ...	99
Figure 38. Summary of the results .....	101
Figure 39. The consecutive wear profiles of the right wheels (60,AAR,empty,T) .....	102
Figure 40. The lateral position of wheelsets and final wheel wear profiles (60,HEU,empty,T) .....	104
Figure 41. The consecutive wear profiles of the left wheels (60,HEU,empty,T) .....	105
Figure 42. The consecutive wear profiles of the right wheels (60,HEU,empty,T) .....	106
Figure 43. The lateral position of wheelsets and final wheel wear profiles (45,AAR,empty,F) .....	108
Figure 44. The consecutive wear profiles of the left wheels (45,AAR,empty,F) .....	109
Figure 45. The consecutive wear profiles of the right wheels (45,AAR,empty,F) .....	110
Figure 46. The experimental wear profiles of AAR wheels (Marcotte et al., 1980) .....	111

Figure 47. Coordinate system of wheelset ..... 121  
Figure 48. Contact patch coordinate system ..... 122

# **Chapter 1 : Introduction**

## **1.1 Wear Problem in Wheel/Rail Contact**

The wear problem in wheel/rail contact has been of concern for a long time. The cost of wheel and rail replacement due to wear is substantial. According to Jamison (1982), about \$600 million per year are spent on the replacement of rail in American. Roney (1983) studied the economic aspects of rail wear on Canadian railways and estimated the expense to be \$300 million per year. In addition, he reported the wheel reprofiling and replacement costs to be \$125 million annually. Wheel wears in Roney's study included flange wear, tread shelling, and tread wear.

In addition to the economic aspects of the wear problem, the dynamic performance of rail vehicles is significantly affected by the profiles of wheels and rails. In rail vehicles, the car lateral stability, suspension design, security against derailment, and fatigue or fracture of wheels and rails are related to wheel/rail geometry. Hence, it is of importance to be able to predict wheel/rail wear profiles.

## 1.2 Literature Review

The wear in wheel/rail systems is complex, and its behavior depends on many parameters. A systems approach to the wear problem has been introduced by Czichos (1980). He divided the tribo-technical system into three components, system structure, input operating variables, and system outputs. Furthermore, Kalousek et al. (1983) proposes a typical wheel/rail tribosystem (Fig. 1) for general study that includes the following:

- Input parameters
  - Operational condition : axle load, car type, truck type, travelling speed.
  - Contact : wheel/rail profile, creep force/moment, creepage/spin.
  - Materials : metallurgy, hardness.
  - Rheological : lubricant, roughness.
- Systems Envelope
  - Wheelset
  - Rail
  - Lubricant in the interface
- Output Parameters
  - Wear form : adhesive wear, abrasive wear, surface fatigue wear.
  - Longitudinal and transverse cracks
  - corrugations
  - plastic deformation

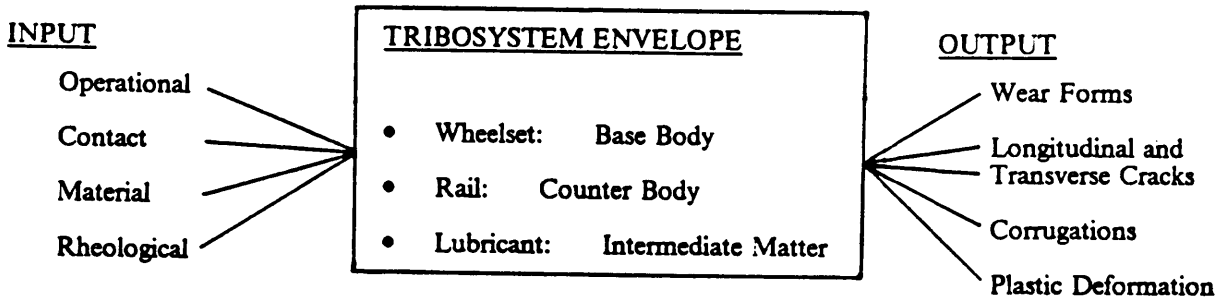


Figure 1. Wheel/rail tribosystem (Kalousek et al., 1983)

Many investigators have researched wheel/rail wear both experimentally and analytically. Bolton and Clayton (1984) identified three wear regimes and examined the effects of wheel/rail metallurgy on the wear process. In their categorization, type I wear is due to oxide and metallic flake formation. Also, type I wear is independent of creepage, but it varies with normal load. Type II wear includes fracture and plastic deformation, and it depends on both contact stress and creepage. Wear rate has the form

$$\frac{W}{Ad} = K_1 \frac{T\gamma}{A} + K_2 \quad (1.1)$$

where

- $W$  = wear volume
- $A$  = contact area
- $d$  = distance rolled
- $T$  = creep force
- $\gamma$  = creepage
- $K_1, K_2$  = constants

Type III wear occurs with the more severe contact condition, such as high creepages or loads. Type III wear is also described by eq. (1.1).

Elkins et al. (1983) carried out a series of wheel wear experiments and studied wear by varying operation conditions, axle load and truck design, and wheel materials. They found that wear increases with axle load and that the radial truck design has a better resistance of wear than the traditional three-piece truck designs. They suggested the same wear equation as eq.(1.1) but without  $K_2$ .

Contact conditions, such as tangential force and surface conditions, also affect wheel wear. Kumar et al. (1984) studied the effects of contact conditions on wear, including lateral force,

and they found that wear increases with lateral load. In eq.(1.1), the creep force,  $T$ , contains the components of longitudinal and lateral creep forces and moment.

Additionally, Kumar et al. (1985) tested the effect of surface conditions on wear by controlling creepage and with and without sand. The wear rate with sand is larger than the wear rate without sand.

Lubricants are usually used to reduce flange wear. Olver et al. (1985) studied lubricated rolling contact and concluded that the delamination wear theory is the best approach for lubricated rolling contact. They also indicated that wear is caused by plastic deformation, fatigue cracking, ductile extrusion and fracture.

In order to predict wheel/rail wear, many wear indices have been developed. A wear index is a characteristic number that is proportional to the wear rate. Fig. 2 shows the wear indices tabulated by Nagurka et al. (1982). A few additional entries identified by the symbol \* have been added to Fig. 2.

Marcotte et al. (1978) and Ghonem (1981) used the angle-of-attack, which is wheelset yaw angle as a wear index. They reported that wear rate increases with angle-of-attack. When angle-of-attack is zero, the prediction of wear rate tends to zero. However, the wear rate is not zero even with zero angle-of-attack, so the angle-of-attack fails to predict wear rate for this case.

Since the slip and creep forces contribute to the wheel/rail wear, considering the normal and flange forces or the creepage independently is not proper. The contact patch work,  $(T\gamma)$  a recently developed and experimentally supported wear index, has been suggested as a wear index. In this wear model, wear is proportional to the energy dissipated in the contact patch during rolling with slip.

Wear Index		Source
$\psi_w$	angle of attack	(Newland, 1969)
		(Boocock, 1969)
		(Marcotte et al., 1978)*
		(Ghonem and Kalousek, 1981)*
$\xi_i$	creepage	
$F_f$	flange force	
$F_f \psi_w$	flange wear index	(Marcotte et al., 1981)
$\mu_f F_f \sqrt{\left(\frac{\Delta_z}{r_T}\right)^2 + (\psi_w \tan \delta_f)^2}$	two-point flange wear index	(Marcotte et al., 1981)
$V \xi_R$	tread wear index	(Doyle, 1979)
$W_1 = \vec{F} \cdot \vec{\xi}$	contact patch work	(Elkins et al., 1979)
		(Kumar et al., 1984, 1985)*
$W_2 = \frac{W_1}{A_r}$	$\frac{\text{contact patch work}}{\text{contact area}}$	(Bolton, 1980, 1984)
		(Clayton et al., 1983)*
		(McEwen and Harvey, 1985)*
$W_v = \frac{B h_1 A_r S}{d_c}$	wear volume	(Kalkstein and Zaremba, 1981)

where

- $\mu_f$  = coefficient of flange friction
- $\Delta_z$  = vertical distance between points of flange and tread contact
- $r_T$  = rolling radius for tread contact
- $\delta_f$  = contact angle at contact patch for flange contact
- $V$  = external vertical load
- $\xi_R$  = resultant creepage
- $B$  = proportionality constant
- $h_1$  = thickness of wear particles
- $S$  = sliding distance
- $d_c$  = critical plastic displacement

**Figure 2. Summary of wear indexes (Nagurka, 1982)**

A number of investigators, such as (Clayton et al., 1983), (Bolton et al., 1984), and (McEwen and Harvey 1985), used  $\frac{T\gamma}{A}$  as a wear index, which is shown in eq. (1.1). Their experiments show that wear rate is linearly dependent on  $\frac{T\gamma}{A}$ . Similar results are presented by Kumar et al. (1984,1985). They also showed that using  $\frac{T\gamma}{A}$  is a good approach to predict wear rate and called this relation the wear-work principle. This wear equation is the same as eq.(1.1) except that  $K_2$  is omitted. This thesis uses the name contact patch work as was suggested by Elkins and Eickhoff, (1979).

Knothe and Hung (1985) applied the concept of the contact patch work model and assumed a sinusoidal wheelset motion to predict the wheel wear rate. Davila (1986) also used the contact patch work model. He included vehicle dynamic response and random rail irregularity, and he assumed a parabolic distribution of wear across the wheel profile.

### **1.3 Scope of the Current Work**

For the purpose of predicting wheel wear using a more realistic approach, the current work uses the contact patch work model and including the following:

1. actual distribution of work done at the contact patch
2. nonlinearity of wheel/rail contact geometry
3. random rail alignment irregularities
4. vehicle dynamic response
5. the effect of wheel wear profile changes during running

In addition, the relationship between the contact patch work model for rolling contact with slip and Archard's (1953) wear model for sliding motion is derived.

Chapter 2 discusses rail vehicle contact mechanics, including wheel/rail contact geometry, definition of creepage and determination of creep forces and moment. Chapter 3 deals with railway vehicle dynamics. A wheelset dynamic model is introduced, then a 5-degree-of-freedom half-car model is presented. Chapter 3 also discusses the irregularities of the track.

Chapter 4 describes the contact patch work model and its application to wheel wear prediction. Chapter 5 presents the simulation method and results. Chapter 6 contains conclusions and recommendation.

## **Chapter 2 : The Wheel/Rail Rolling Contact Problem**

For any discussion of the wear problem in rolling contact, the contact mechanics problem should be understood first. The wheel and rail geometry affects the interfacial force between the wheel and rail, and it therefore has a significant effect on wheelset dynamic behavior. This chapter includes discussions of wheel/rail contact geometry and also the influence of creepages on creep forces and moment.

Section 2.1 discusses the wheel/rail geometric contact problem. A program called WHRAILA (Heller and Cooperrider, 1977a) is introduced to calculate the geometric constraint functions, including the roll angle of wheelset, contact angle, and rolling radii, in terms of the lateral displacement of the wheelset. These geometric constraints are necessary for calculating the creepages and the dynamic response of the wheelset.

Next, the definition of the creepage is presented. The creepages cause in plane forces during rolling contact, and they are important in both railway vehicle dynamics and wear in rolling contact.

Kalker's simplified theory in rolling contact, based on the Hertzian contact, is presented as a method to obtain the creep force and moment. A program called FASTSIM (Kalker, 1982), is

modified to obtain the creep moment and local creep quantities, including forces, moment, and creepages.

Finally, a study of the slip/adhesion region at the contact patch is presented. It will become clear later that it is necessary to distinguish the slip and adhesion regions and to determine the slip velocity which is used to calculate the contact patch work. This is discussed further in chapter 4.

## 2.1 Determination of Wheel/Rail Geometric Constraint

The geometries of wheel and rail have a dominant effect on rail vehicle behavior. The contact stress and frictional forces depend upon the wheel/rail geometry, especially the rolling radii and the wheel/rail contact angle. Consequently, the dynamic behavior and the security against derailment are also dependant upon the wheel/rail geometry. Therefore, the profile of wheel and rail and the wheel/rail kinematic constraints are of interest. The profiles of an AAR 1:20 wheel (Cooperrider et al., 1981) and a Heumann wheel (Elkins et al., 1986) and a 132-RE rail (AREA, 1984), which are used in this works are shown in Fig. 3 to Fig. 5 respectively. Fig. 6 defines the terminology of wheel/rail contact.

The wheel/rail geometric constraint relationships are a function of the lateral distance from the wheelset centerline to the track centerline,  $y_w$ , and the yaw angular rotation of the wheelset about the vertical axis,  $\psi_w$ , as shown in Fig. 7. The influence of the wheelset yaw angle,  $\psi_w$ , is small, so  $\psi_w$  can be neglected in finding the contact position of the wheel and rail and other geometry constraint functions.

WHRAILA is a FORTRAN program developed by Heller and Cooperrider (1977a). It is widely used to calculate the wheel and rail geometric constraints. Fig. 8 and Fig. 9 are the output from WHRAILA for an AAR 1:20 wheel and a 132-RE rail. In these figures, the contact position

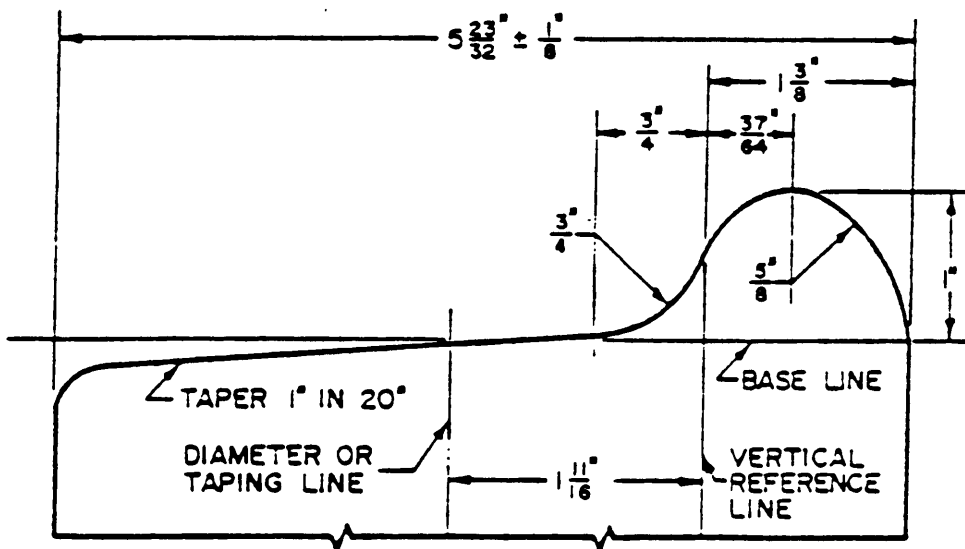


Figure 3. AAR 1:20 wheel profile (Cooperrider et al., 1981)

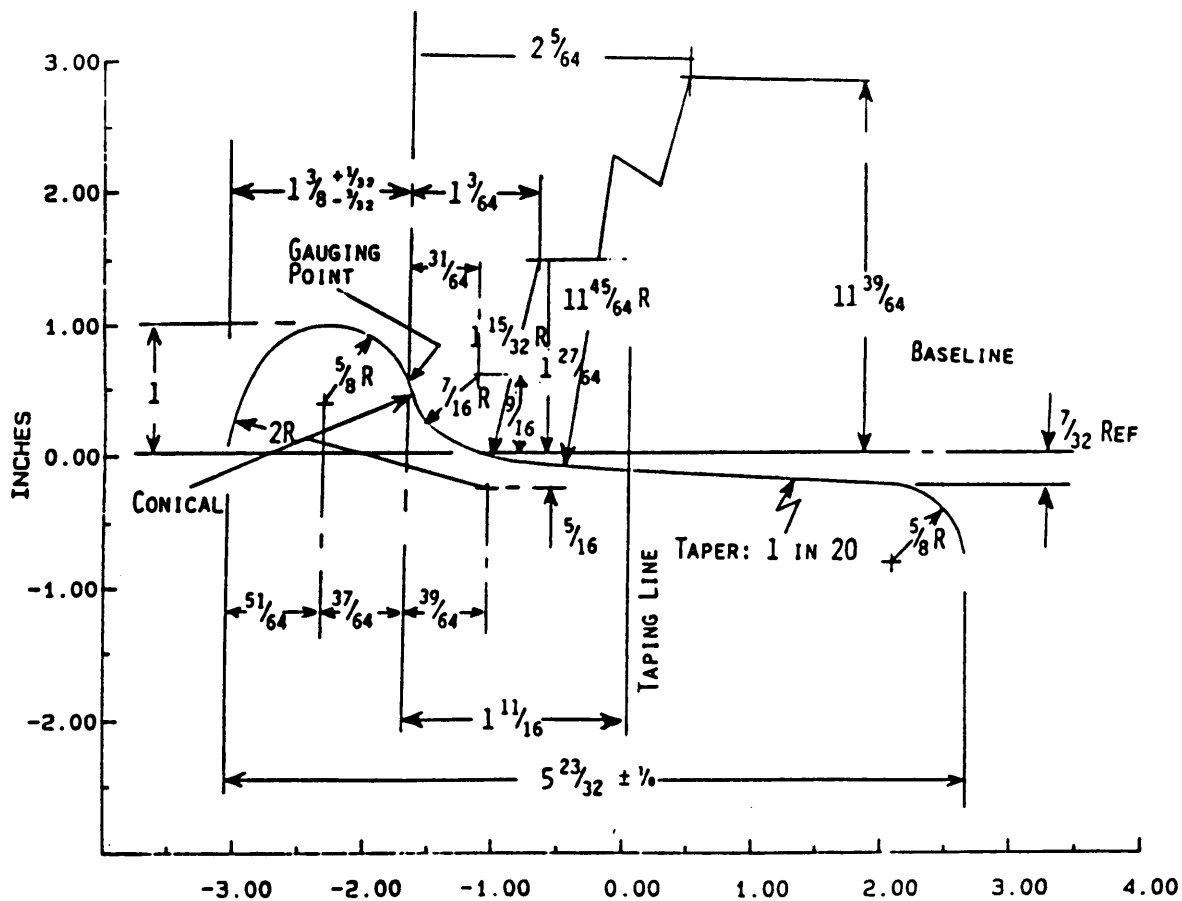


Figure 4. Heumann wheel profile (Elkins et al., 1986)

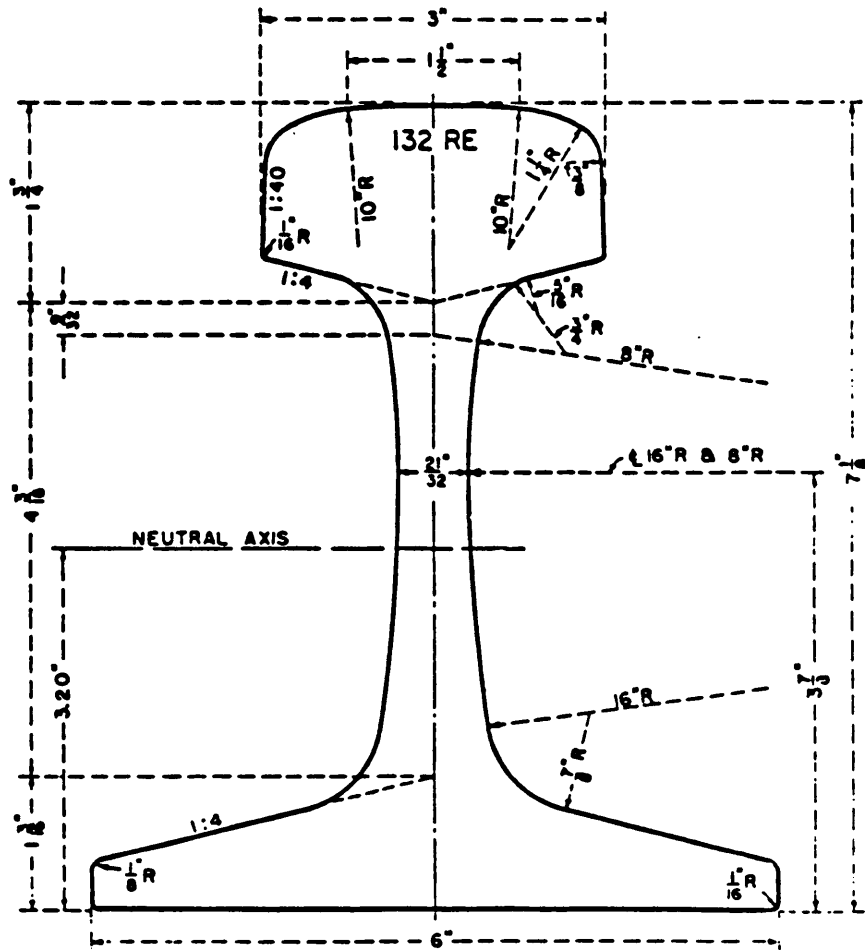
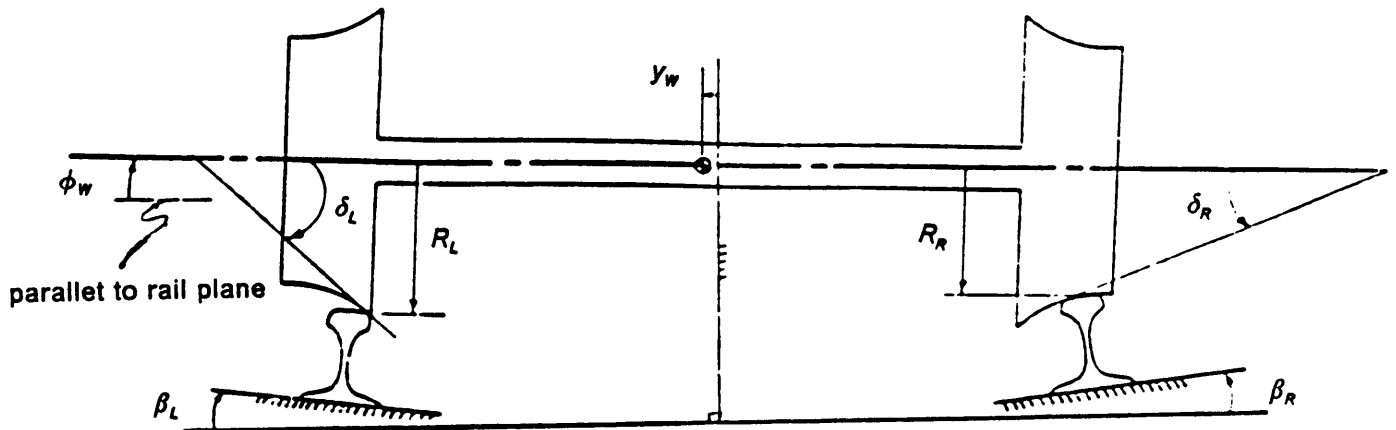
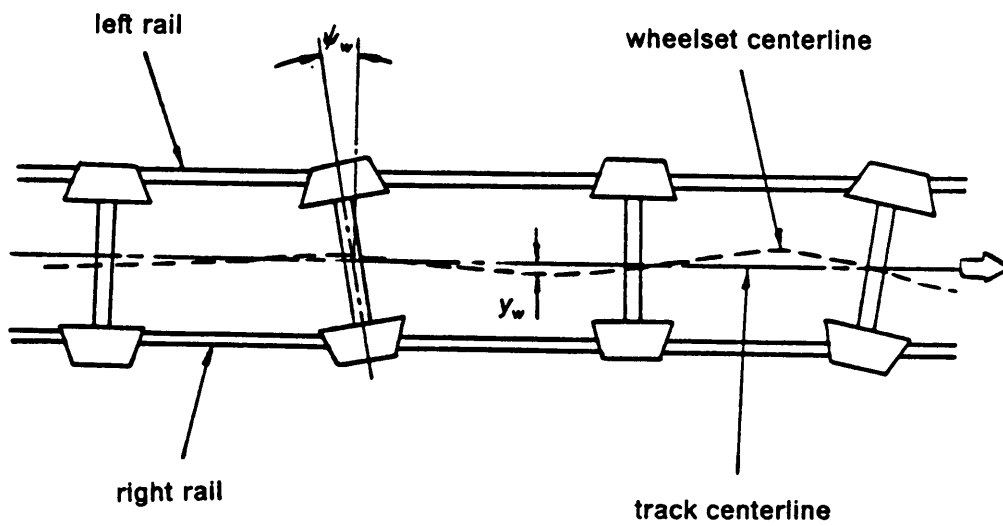


Figure 5. 132-RE rail profile (AREA, 1984)

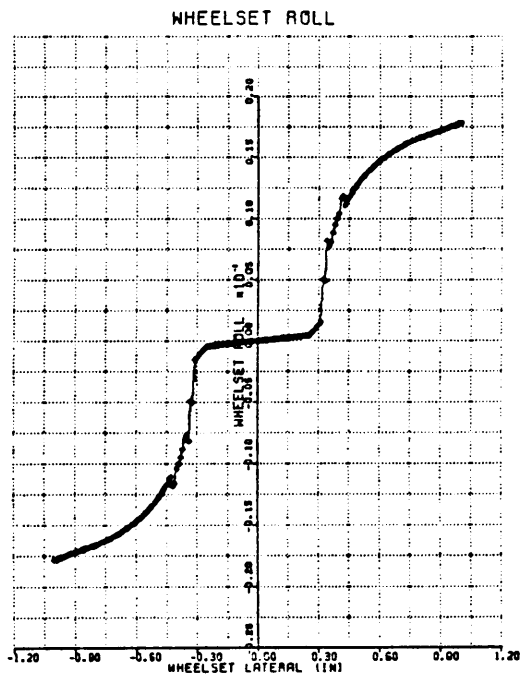


- $y_w$  = wheelset lateral displacement
- $\phi_w$  = wheelset roll angle
- $\delta_L$  = contact angle of the left wheel and rail
- $\delta_R$  = contact angle of the right wheel and rail
- $\beta_L$  = left rail cant angle
- $\beta_R$  = right rail cant angle
- $R_L$  = rolling radius of left wheel at the contact point
- $R_R$  = rolling radius of right wheel at the contact point

Figure 6. Wheel/rail contact relationships



**Figure 7. Effect of lateral and yaw displacement on wheel/rail contact**



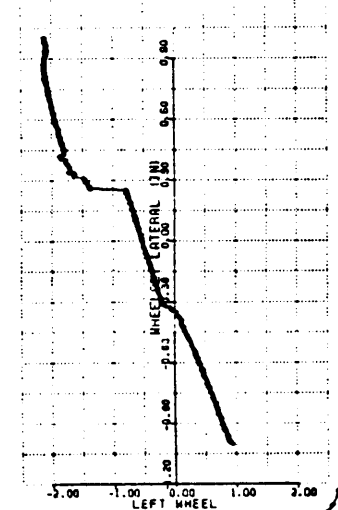
RIGHT SIDE

NEW AAR 1:20 WHEEL (MATH)  
 132-RE RAIL (THEORETICAL)  
 RAIL CANT -0.025

LEFT SIDE

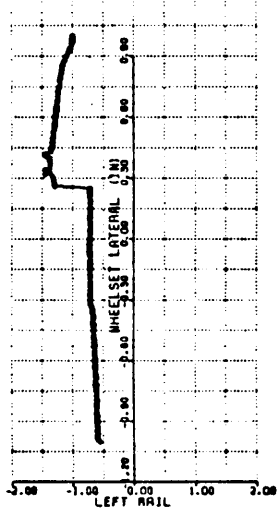
NEW AAR 1:20 WHEEL (MATH)  
 132-RE RAIL (THEORETICAL)  
 RAIL CANT -0.025

WHEEL CONTACT POSITION



NEW AAR 1:20 WHEEL (MATH)

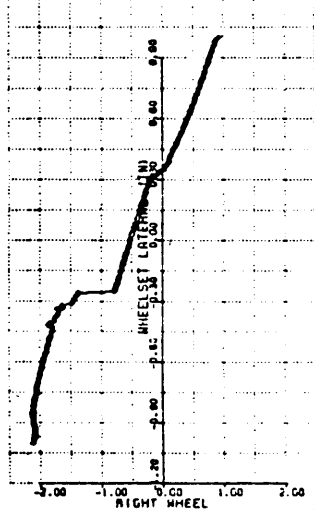
RAIL CONTACT POSITION



132-RE RAIL (THEORETICAL)

RAIL CANT FOR LEFT RAIL -0.025

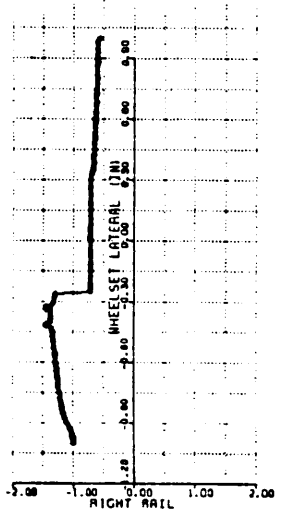
WHEEL CONTACT POSITION



NEW AAR 1:20 WHEEL (MATH)

WHEEL GAUGE 53.0  
 RAIL GAUGE 56.5

RAIL CONTACT POSITION



132-RE RAIL (THEORETICAL)

RAIL CANT FOR RIGHT RAIL -0.025

Figure 8. Wheel/rail geometric constraint functions (WHRAILA by Heller and Cooperrider, 1977a)

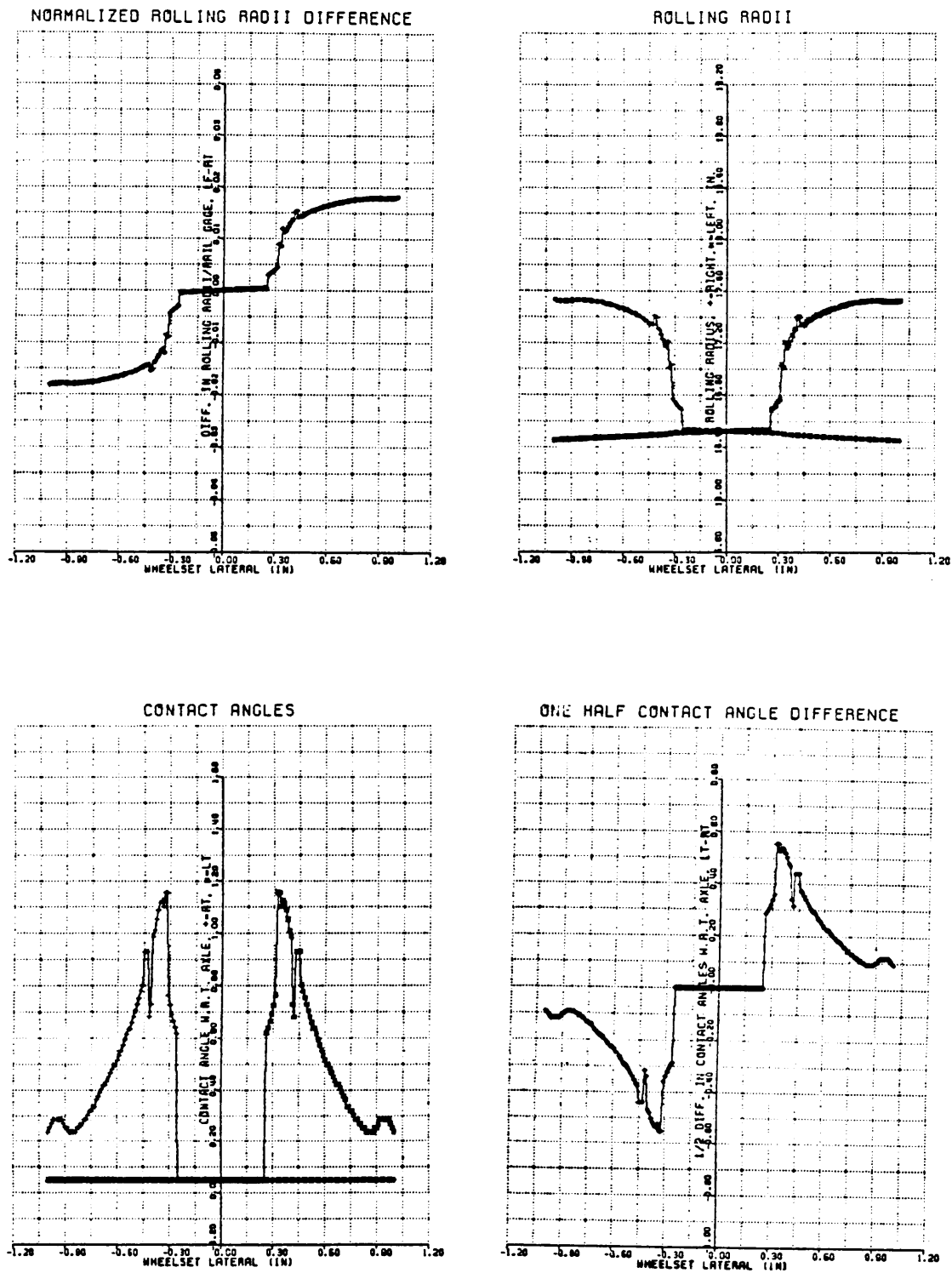


Figure 9. Wheel/rail geometry constraint functions (continue)

of the wheel and rail, roll angle, contact angle, and rolling radii are given in terms of the wheelset lateral displacement,  $y_w$ . It is noted that flange contact occurs when the wheelset lateral displacement is more than  $\pm 0.29$  in.

## 2.2 Definition of Creepage

In rolling contact with slip, the interfacial force and moment between the wheel and rail are functions of creepages. Therefore, the derivation of the creepage expressions is a fundamental issue. The longitudinal ( $\xi_x$ ), lateral ( $\xi_y$ ), and spin ( $\xi_{SP}$ ) creepages are defined as

$$\xi_x = \frac{V_{xW} - V_{xT}}{V} \quad (2.1)$$

$$\xi_y = \frac{V_{yW} - V_{yT}}{V} \quad (2.2)$$

$$\xi_{SP} = \frac{\omega_{zW} - \omega_{zT}}{V} \quad (2.3)$$

where

- $V_{xW}$  = longitudinal velocity of wheel at the contact point
- $V_{xT}$  = longitudinal velocity of rail at the contact point
- $V_{yW}$  = lateral velocity of wheel at the contact point
- $V_{yT}$  = lateral velocity of rail at the contact point
- $\omega_{zW}$  = angular velocity of wheel at the contact point
- $\omega_{zT}$  = angular velocity of rail at the contact point
- $V$  = nominal velocity

A complete derivation of the creepage expressions is shown in Appendix B. By assuming small angles and neglecting higher-order terms, the creepages for the left wheel in the wheelset coordinates which are defined in Fig. 47 are

$$\xi'_{XL} = \frac{1}{V} \left\{ V \left[ 1 - \left( \frac{R_L}{R_0} \right) \right] - \dot{\beta} R_L - A \dot{\psi} \right\} \quad (2.4)$$

$$\xi'_{YL} = \frac{1}{V} \{ \dot{y} + R_L \dot{\phi} - V \psi \} \quad (2.5)$$

$$\xi'_{SPL} = \frac{1}{V} \{ \dot{\psi} - \Omega \delta_L \} \quad (2.6)$$

The creepages for the right wheel in the wheelset coordinates are

$$\xi'_{XR} = \frac{1}{V} \left\{ V \left[ 1 - \left( \frac{R_R}{R_0} \right) \right] - \dot{\beta} R_R + A \dot{\psi} \right\} \quad (2.7)$$

$$\xi'_{YR} = \frac{1}{V} \{ \dot{y} + R_R \dot{\phi} - V \psi \} \quad (2.8)$$

$$\xi'_{SPR} = \frac{1}{V} \{ \dot{\psi} + \Omega \delta_R \} \quad (2.9)$$

where

- $R_0$  = nominal rolling radius of the wheels
- $R_R$  = rolling radius of right wheel at the contact point
- $R_L$  = rolling radius of left wheel at the contact point
- $A$  = half wheel gauge
- $\Omega$  = nominal angular velocity
- $\dot{y}$  = wheelset lateral velocity
- $\dot{\psi}$  = wheelset yaw angular velocity
- $\dot{\phi}$  = wheelset roll angular velocity
- $\dot{\beta}$  = perturbation of wheelset spin angular velocity

These creepage expressions are used to obtain inputs for the FASTSIM program, which computes the contact forces and creep distributions. The wheelset spin perturbation velocity,  $\dot{\beta}$ , was initially not included in the analysis. However, early results showed that the creepages calculated when  $\dot{\beta}$  was omitted were incorrect. Therefore the spin perturbation angular velocity was included in this work.

## 2.3 The Hertzian Contact Problem

In wheel/rail contact problems, it is usually acceptable to apply the Hertzian contact theory to obtain the area of the contact patch. This approximation is routinely made by rail vehicle dynamicists. The determination of the creep forces and moment by the simplified theory (Kalker, 1982) is based on the Hertzian contact theory. Simplified theory is discussed in the next section.

According to Hertzian contact theory (Timoshenko and Goodier, 1970), the contact patch is an ellipse with the ratio of the semiaxes ( $\frac{a}{b}$ ), where  $a$  and  $b$  are functions of normal force, curvatures, Young's modulus and Poisson's ratio of the contact bodies. The basic assumptions of the Hertzian contact theory are summarized as follows:

- homogeneous, isotropic and perfectly elastic materials
- contact surfaces are ideally smooth
- curvatures of contact bodies are constant
- no slips between contact bodies
- no hydrodynamic film between the interactive surface, i.e., dry surfaces

Since Hertzian contact theory is well known and well documented, the details are not included here.

## 2.4 Creep Forces and Moment in Rolling Contact

The literature is rich with work on the rolling contact problem. A few of the more important contributions are summarized here. In one of the earliest contributions, Carter (1926) published a solution to the problem of two-dimensional rolling with slip. He considered the problem of traction between cylinders, and he included only longitudinal creepage.

Vermeulen and Johnson (1964) solved the rolling contact problem for three-dimensional bodies in contact including both the longitudinal and lateral creepage, but excluding the spin creepage.

Kalker (1967a) took lateral creepage into account, and he obtained a simple approximate solution of the rolling contact problem. Later, he obtained a solution for the case of general creepage including spin (Kalker, 1967b). Kalker's linear theory, which assumes the existence of vanishingly small creepages and slip areas in the contact patch, provides the correct relationship between creepages and creep forces for small creepages. Because of its simplicity, the linear theory has been widely adopted by researchers in rail vehicle dynamics.

More recently, Kalker (1982) developed a fast algorithm, called FASTSIM, that is based upon the simplified theory. In Kalker's simplified theory, a linear relationship is assumed between the local traction and the local material elastic displacement. FASTSIM computes the creep forces but not creep moment. In most rail vehicle work, the moment is relatively unimportant.

A number of rail vehicle dynamicists use a heuristic creep force model because of its simplicity and speed of computation. The heuristic model uses the creep coefficients from Kalker's (1967a) linear theory, and the form of the creep force saturation curve from the Vermeulen and Johnson (1964) work. Shen et al. (1983) documented this model and compared

its accuracy to computations based upon Kalker's FASTSIM algorithm and another algorithm called DUVOROL that was formulated by Kalker and Tjoeng (Shen et al., 1983).

Generally speaking, it is not necessary to obtain the distribution of creep force and moment in the contact patch. Only the resultant force and moment are usually needed to implement dynamics models. In this work, the local creep force and moment are required so as to calculate the distribution of the work done in the contact patch, and a wear model is employed that postulates wear to be proportional to the work done between the contacting surfaces.

In this section the program FASTSIM and a recent modification (Wang and Fries, 1988a) to it are discussed. FASTSIM has been modified to compute the creep moment and also the creep force, moment and slip velocity distributions within the contact patch.

Consider a wheel rolling over a rail at a constant speed,  $V$ , as shown in Fig. 10. The contact patch is an ellipse with the ratio of the semiaxes  $(\frac{a}{b})$ , according to the Hertzian contact theory. The creep forces and moment can be obtained by integrating the shear pressures  $(P_x, P_y)$  over the contact area. Eq.(2.12) has been added to Kalker's original work in FASTSIM.

$$F_x \equiv \iint_S P_x(x,y) dx dy \quad (2.10)$$

$$F_y \equiv \iint_S P_y(x,y) dx dy \quad (2.11)$$

$$M_z \equiv \iint_S [P_y(x,y) x - P_x(x,y) y] dx dy \quad (2.12)$$

where

$F_x$  = longitudinal creep force

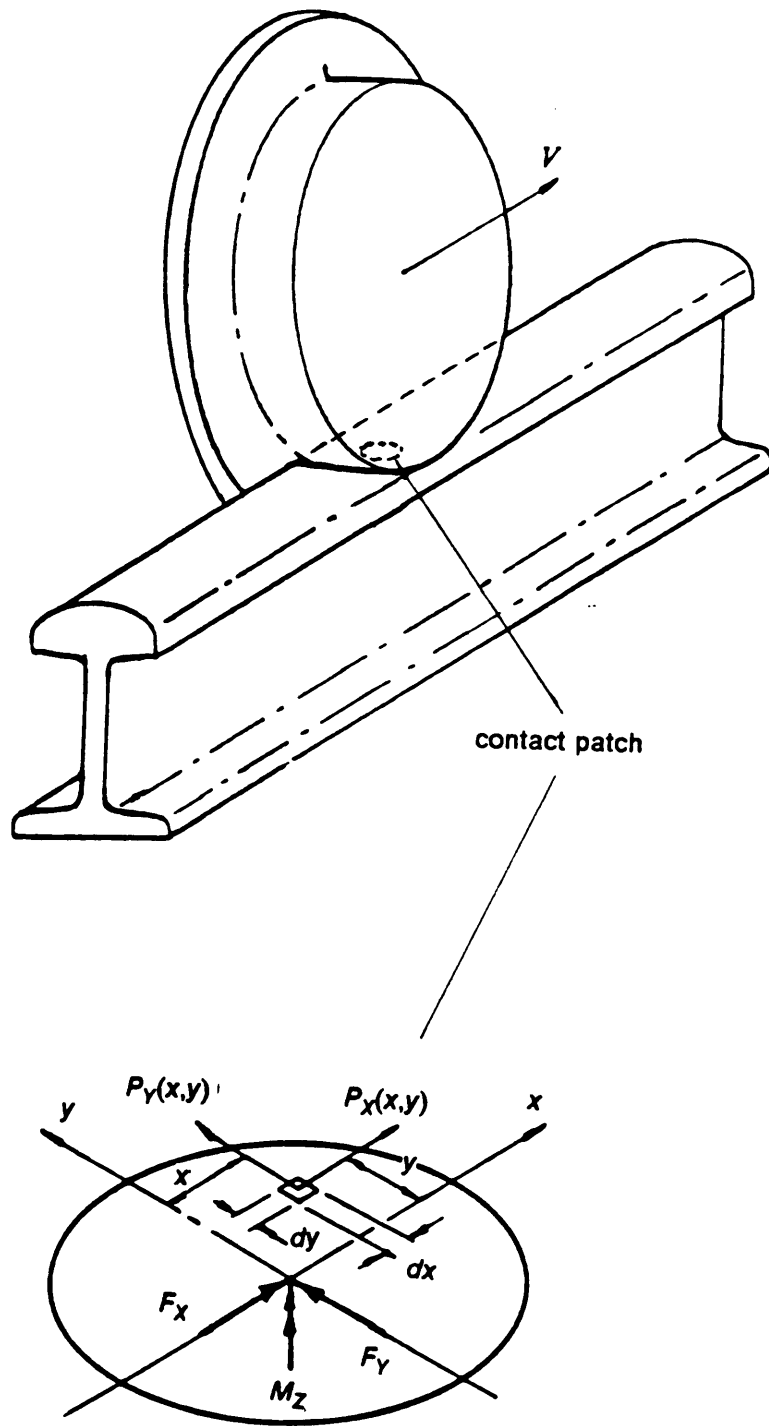


Figure 10. Force and moment acting on contact area,  $S$

- $F_y$  = lateral creep force  
 $M_z$  = creep moment  
 $P_x$  = longitudinal shear pressure  
 $P_y$  = lateral shear pressure  
 $P_z$  = normal pressure  
 $S$  = the region of the elliptical contact patch

and

$$S = \left\{ (x,y) \mid \left(\frac{x}{a}\right)^2 + \left(\frac{y}{b}\right)^2 \leq 1 \right\} \quad (2.13)$$

The velocities of the particles at the surface of either the wheel or rail can be expressed as

$$U_x(x,y) = V + \delta V_x - \omega_z y - \frac{d\hat{u}_x}{dt} \quad (2.14)$$

$$U_y(x,y) = \delta V_y + \omega_z x - \frac{d\hat{u}_y}{dt} \quad (2.15)$$

where

- $U_x, U_y$  = the velocities of the particles at the surface of the contact patch  
 $\delta V_x, \delta V_y$  = creep (slip) velocities  
 $\omega_z$  = spin angular velocity  
 $\hat{u}_x, \hat{u}_y$  = tangential elastic deformation

Since  $\hat{u}_x = \hat{u}_x(x,y,t)$  and  $\hat{u}_y = \hat{u}_y(x,y,t)$ , the exact derivatives of  $\hat{u}_x$  and  $\hat{u}_y$  are

$$\frac{d\hat{u}_x}{dt} = \frac{\partial \hat{u}_x}{\partial x} \frac{\partial x}{\partial t} + \frac{\partial \hat{u}_x}{\partial y} \frac{\partial y}{\partial t} + \frac{\partial \hat{u}_x}{\partial t} \frac{\partial t}{\partial t} \quad (2.16)$$

$$\frac{d\hat{u}_y}{dt} = \frac{\partial \hat{u}_y}{\partial x} \frac{\partial x}{\partial t} + \frac{\partial \hat{u}_y}{\partial y} \frac{\partial y}{\partial t} + \frac{\partial \hat{u}_y}{\partial t} \frac{\partial t}{\partial t} \quad (2.17)$$

where

$$\frac{d\hat{u}_x}{dt}, \frac{d\hat{u}_y}{dt} = \text{tangential elastic deformation velocity at a surface point (x,y)}$$

Because the lateral velocity is zero, and longitudinal velocity is  $V$ , eq. (2.16) and (2.17) become

$$\frac{d\hat{u}_x}{dt} = V \frac{\partial \hat{u}_x}{\partial x} + \frac{\partial \hat{u}_x}{\partial t} \quad (2.18)$$

$$\frac{d\hat{u}_y}{dt} = V \frac{\partial \hat{u}_y}{\partial x} + \frac{\partial \hat{u}_y}{\partial t} \quad (2.19)$$

By substituting the deformed velocity, eq.(2.14) and (2.15) become

$$U_x(x,y) = V + \delta V_x - \omega_z y - \left( V \frac{\partial \hat{u}_x}{\partial x} + \frac{\partial \hat{u}_x}{\partial t} \right) \quad (2.20)$$

$$U_y(x,y) = \delta V_y + \omega_z x - \left( V \frac{\partial \hat{u}_y}{\partial x} + \frac{\partial \hat{u}_y}{\partial t} \right) \quad (2.21)$$

For the case of steady rolling,  $\left( \frac{\partial \hat{u}_x}{\partial t} = 0, \frac{\partial \hat{u}_y}{\partial t} = 0 \right)$ , the micro-slip velocity of the contact patch at position  $(x,y)$  between wheel and rail can be obtained by

$$W_x = (\delta V_{xW} - \delta V_{xT}) - (\omega_{zW} - \omega_{zT}) y - V \left( \frac{\partial \hat{u}_{xW}}{\partial x} - \frac{\partial \hat{u}_{xT}}{\partial x} \right) \quad (2.22)$$

$$W_y = (\delta V_{yW} - \delta V_{yT}) + (\omega_{zW} - \omega_{zT}) x - V \left( \frac{\partial \hat{u}_{yW}}{\partial x} - \frac{\partial \hat{u}_{yT}}{\partial x} \right) \quad (2.23)$$

where

$W_x, W_y$  = micro-slip velocities of the particles at the surface of the contact patch

$\delta V_{xW}, \delta V_{yW}$  = creep (slip) velocities for wheel

$\delta V_{xT}, \delta V_{yT}$  = creep (slip) velocities for rail

$\omega_{zW}$  = spin angular velocity of wheel

$\omega_{zT}$  = spin angular velocity of rail

By dividing by nominal velocity,  $V$ , and substituting the creepage definition, eq. (2.22) and (2.23) become

$$\frac{W_x}{V} = \xi_x - \xi_{SP} y - \frac{\partial u_x}{\partial x} \quad (2.24)$$

$$\frac{W_y}{V} = \xi_y - \xi_{SP} x - \frac{\partial u_y}{\partial x} \quad (2.25)$$

where

- $V$  = nominal velocity
- $W_x$  = longitudinal slip velocity at (x,y)
- $W_y$  = lateral slip velocity at (x,y)
- $u_x$  =  $\hat{u}_{xw} - \hat{u}_{xt}$   
= difference of longitudinal elastic displacement of wheel and rail at (x,y)
- $u_y$  =  $\hat{u}_{yw} - \hat{u}_{yt}$   
= difference of lateral elastic displacement of wheel and rail at (x,y)
- $\xi_x$  = longitudinal creepage
- $\xi_y$  = lateral creepage
- $\xi_{SP}$  = spin creepage

Notice that  $W_x$  and  $W_y$  include the rigid body motions consisting of the translational motion in the x and y direction ( $\xi_x$ ,  $\xi_y$ ), the rotational motion in the z direction ( $\xi_{SP} y$ ,  $\xi_{SP} x$ ), and the elastic displacements ( $\frac{\partial u_x}{\partial x}$ ,  $\frac{\partial u_y}{\partial x}$ ).

In the simplified theory (Kalker, 1982) for an anisotropic relation, Kalker assumed

$$u_x = L P_x \quad (2.26)$$

$$u_y = L P_y \quad (2.27)$$

where

$L$  = some constant

By substituting eq. (2.26) and (2.27) and dividing by  $L$ , the normalized slip equations, (2.24) and (2.25), become

$$\frac{W_X}{VL} = \frac{\xi_X}{L} - \frac{\xi_{SPY}}{L} - \frac{\partial P_X}{\partial x} \quad (2.28)$$

$$\frac{W_Y}{VL} = \frac{\xi_Y}{L} + \frac{\xi_{SPX}}{L} - \frac{\partial P_Y}{\partial x} \quad (2.29)$$

Furthermore,

$$\frac{W_X}{VL_1} = \frac{\xi_X}{L_1} - \frac{\xi_{SPY}}{L_3} - \frac{\partial P_X}{\partial x} \quad (2.30)$$

$$\frac{W_Y}{VL_2} = \frac{\xi_Y}{L_2} + \frac{\xi_{SPX}}{L_3} - \frac{\partial P_Y}{\partial x} \quad (2.31)$$

where  $L_1$ ,  $L_2$ , and  $L_3$  are determined from Kalker's linear theory (1967a),

$$L_1 = \frac{8a}{3C_{11}G} \quad (2.32)$$

$$L_2 = \frac{8a}{3C_{12}G} \quad (2.33)$$

$$L_3 = \frac{\pi a \sqrt{\frac{a}{b}}}{4C_{23}G} \quad (2.34)$$

where

- $a$  = length of longitudinal semi-axis of elliptical contact patch
- $b$  = length of lateral semi-axis of elliptical contact patch
- $G$  = shear modulus of the contact bodies
- $C_{ij}$  = the creepage and spin coefficients ( Kalker, 1979)

According to Kalker's suggestion (1982), the variables are nondimensionalized to implement the calculation of the creep forces and moment in the program FASTSIM.

$$\begin{aligned} X' &= \frac{x}{a} & P'_{X'} &= \frac{P_X}{\mu Z_0} \\ Y' &= \frac{y}{b} & P'_{Y'} &= \frac{P_Y}{\mu Z_0} \\ Z' &= \frac{P_Z}{Z_0} \end{aligned} \tag{2.35}$$

$$Z_0 = \frac{N}{abN'} \tag{2.36}$$

$$N = \iint_S P_Z dx dy \tag{2.37}$$

$$N' = \iint_{S'} Z' dX' dY' = \iint_{S'} (1 - X'^2 - Y'^2) dX' dY' = \frac{\pi}{2} \tag{2.38}$$

$$S' = \{(X', Y') \mid X'^2 + Y'^2 \leq 1\} \tag{2.39}$$

where

$N$  = normal force

$\mu$  = coefficient of friction

$(..)'$  = some nondimensional quantity

By substituting the above nondimensional quantities, the slip equations (2.30) and (2.31) become

$$W'_X = \xi'_X - Y' \xi'_{SP_X} - \frac{\partial P'_X}{\partial X'} \quad (2.40)$$

$$W'_Y = \xi'_Y + X' \xi'_{SP_Y} - \frac{\partial P'_Y}{\partial X'} \quad (2.41)$$

where

$$W'_X = \frac{aW_X}{\mu Z_0 V L_1} \quad (2.42)$$

$$W'_Y = \frac{aW_Y}{\mu Z_0 V L_2} \quad (2.43)$$

$$\xi'_X = \frac{a\xi_X}{\mu Z_0 L_1} \quad (2.44)$$

$$\xi'_Y = \frac{a\xi_Y}{\mu Z_0 L_2} \quad (2.45)$$

$$\xi'_{SP_X} = \frac{ab\xi_{SP}}{\mu Z_0 L_3} \quad (2.46)$$

$$\xi'_{SP_Y} = \frac{a^2\xi_{SP}}{\mu Z_0 L_3} \quad (2.47)$$

From eq. (2.10) - (2.12), the normalized forces and moment can be obtained.

$$F'_X \equiv \iint_{S'} P'_X(X', Y') dX' dY' = \frac{1}{abZ_0\mu} F_X \quad (2.48)$$

$$F'_Y \equiv \iint_{S'} P'_Y(X', Y') dX' dY' = \frac{1}{abZ_0\mu} F_Y \quad (2.49)$$

$$M'_Z \equiv \iint_{S'} \{P'_Y(X', Y') a X' - P'_X(X', Y') b Y'\} dX' dY' = \frac{1}{abZ_0\mu} M_Z \quad (2.50)$$

FASTSIM (Kalker, 1982) used eq. (2.48) and (2.49) and the nondimensionalized quantities described above to compute the nondimensionalized lateral and longitudinal creep forces. Eq. (2.50) was added to the FASTSIM code to compute the nondimensionalized spin moment (Wang and Fries, 1988a). Note that  $M'_Z$  in eq. (2.50) is different from the nondimensionalized moment used by Kalker (1967c). The dimensional forces and moment are computed by

$$F_X = \frac{2}{\pi} \mu P F'_X \quad (2.51)$$

$$F_Y = \frac{2}{\pi} \mu P F'_Y \quad (2.52)$$

$$M_Z = \frac{2}{\pi} \mu P M'_Z \quad (2.53)$$

In addition to the creep forces,  $(F_X, F_Y)$ , and creep moment,  $M_Z$ , the local creep forces and moment at each subarea,  $(F_{X_{ij}}, F_{Y_{ij}}, M_{Z_{ij}})$ , and the local normalized slips  $(\frac{W_x}{V}|_{ij}, \frac{W_y}{V}|_{ij})$ , and spin  $(\frac{\Omega}{V}|_{ij})$  shown in Fig. 11 are computed by the modified FASTSIM.

## 2.5 Study of Slip/Adhesion Region at the Contact Patch

The contact patch is divided into the slip and adhesion regions, and no relative motion occurs between the contacting bodies in the adhesion region. From Coulomb law, the slip and adhesion regions are given by

$$S_{\text{slip}} = \{(x,y) | (P_X(x,y), P_Y(x,y)) > \mu P_Z\} \quad (2.54)$$

$$S_{\text{adh}} = \{(x,y) | (P_X(x,y), P_Y(x,y)) \leq \mu P_Z\} \quad (2.55)$$

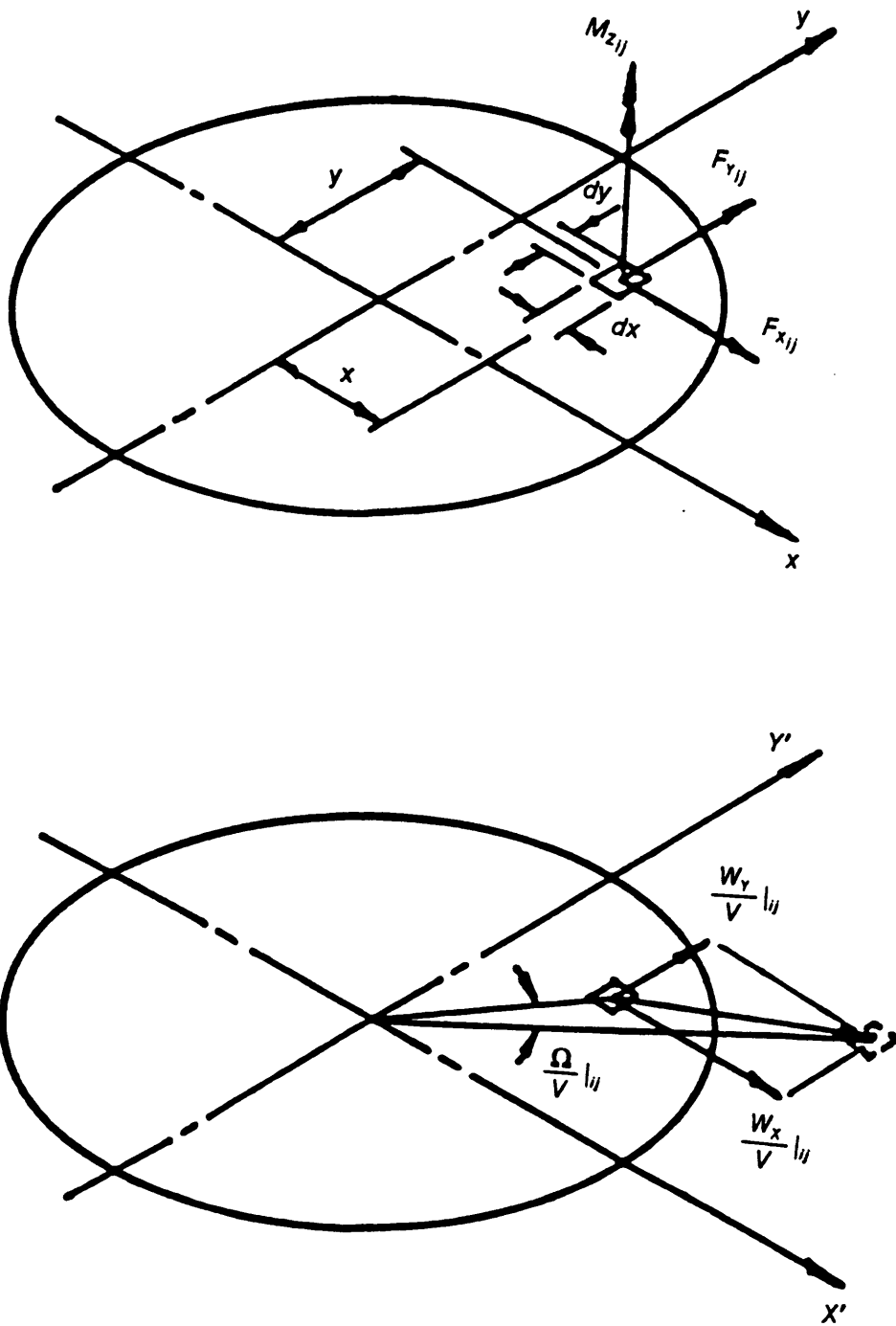


Figure 11. Local creep force and slip at the contact patch

where

$S_{\text{slip}}$  = slip region

$S_{\text{adh}}$  = adhesion region

The slip and adhesion regions are easily found using eq. (2.54) and (2.55). A general view of slip and adhesion regions is shown in Fig. 12.

A number of factors affect the size and the distribution of the slip and adhesion regions. When the load, the geometry and materials of the contacting bodies, and the coefficient of friction are fixed, the influence of creepage alone on the slip and adhesion regions can be observed. For wear work, the locations of the slip and adhesion regions are important because no energy is dissipated in the adhesion region.

Figure 13 shows the distribution of slip and adhesion in a contact patch with  $a/b = 2$ . The slip region is crosshatched, the adhesion region is clear, and rolling is in the x-direction. The spin creepage is zero for Fig. 13. When the lateral and longitudinal creepages are increased, the slip region maintains symmetry with respect to the x-axis. With increased creepage, the slip region moves forward in the contact patch until the creepages are high enough that the slip region encompasses the entire region.

Figure 14 shows the distribution of slip and adhesion for the same conditions as Fig. 13 except that the lateral creepage is zero, and cases of small and large spin creepage are shown. The presence of spin creepage causes asymmetry of the slip and adhesion regions. The large spin case has sufficient spin creepage that the slip region nearly covers the contact patch. For small spin, the slip region is thicker on the negative side of the y-axis.

Figure 15 shows the distribution of slip and adhesion for the same conditions as Fig. 13 except that the longitudinal creepage is zero, and cases of small and large spin creepage are shown. For small spin creepage, the development of slip region is similar to the pure creepage case.

Resultant  
Creep Force

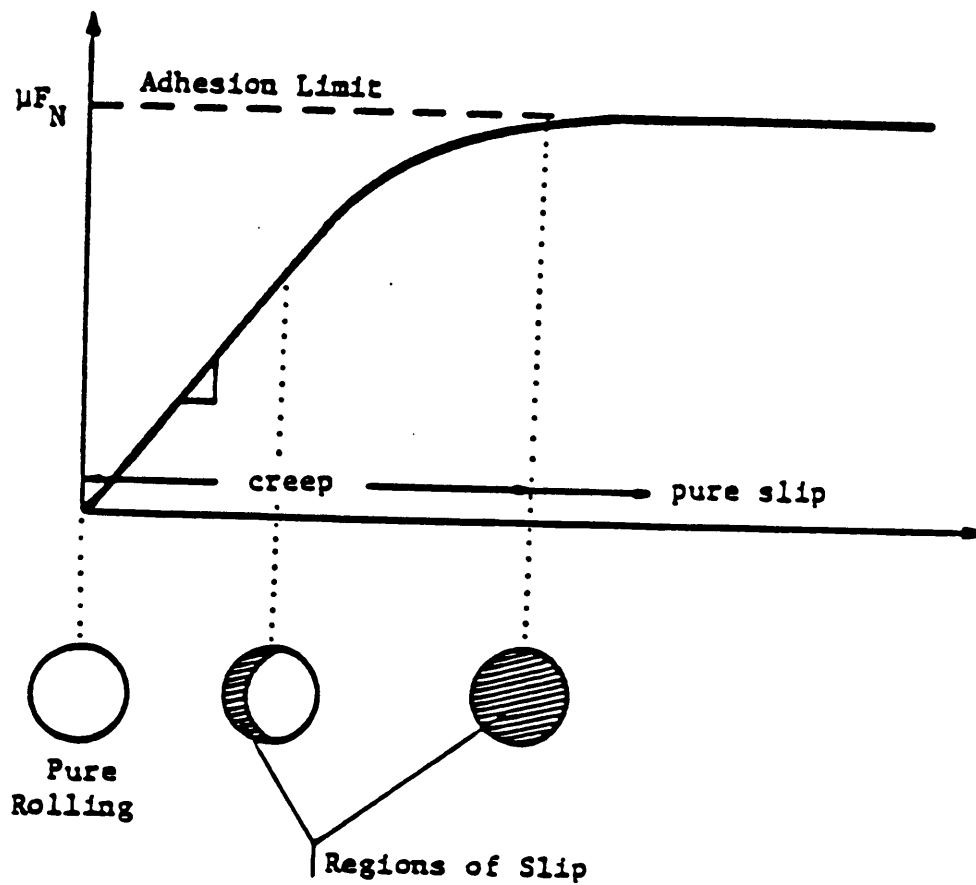


Figure 12. Slip/adhesion region related to creep force (Nagurka, 1983)

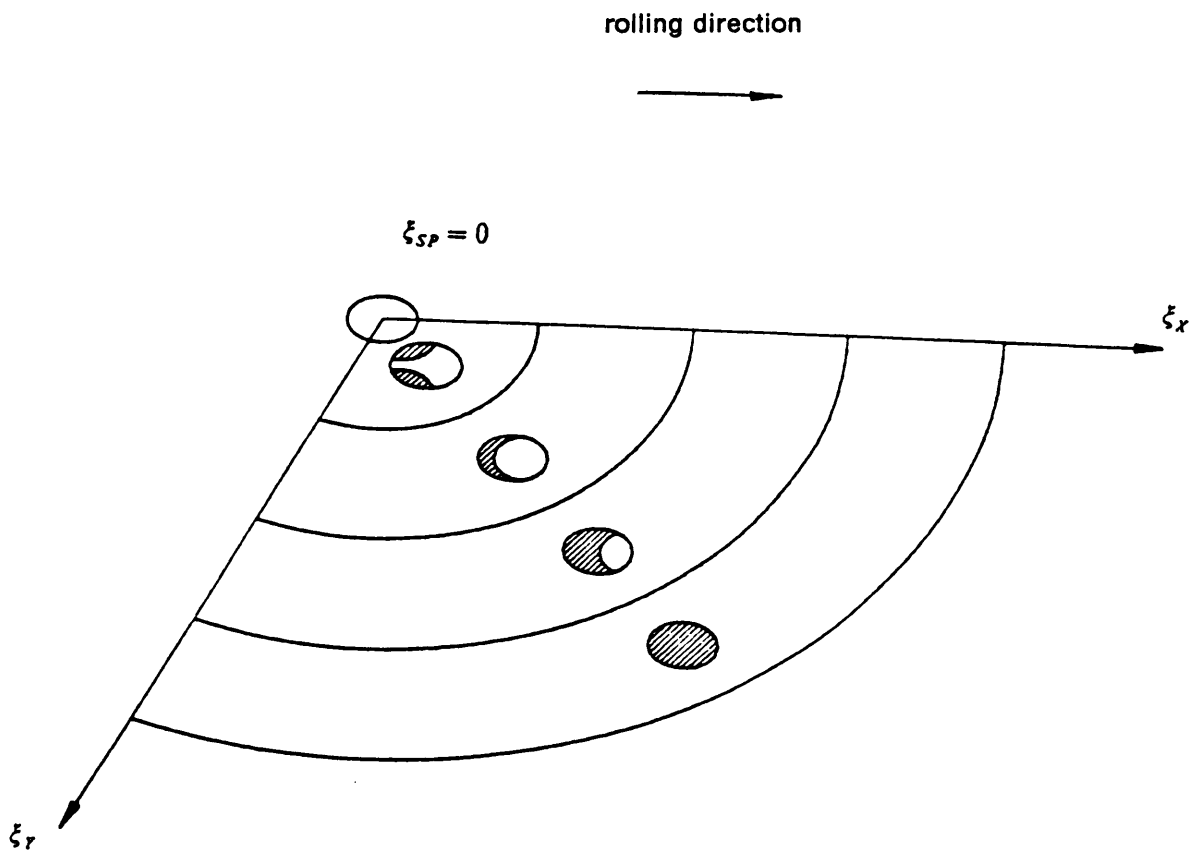


Figure 13. Slip/adhesion regions for zero spin creepage

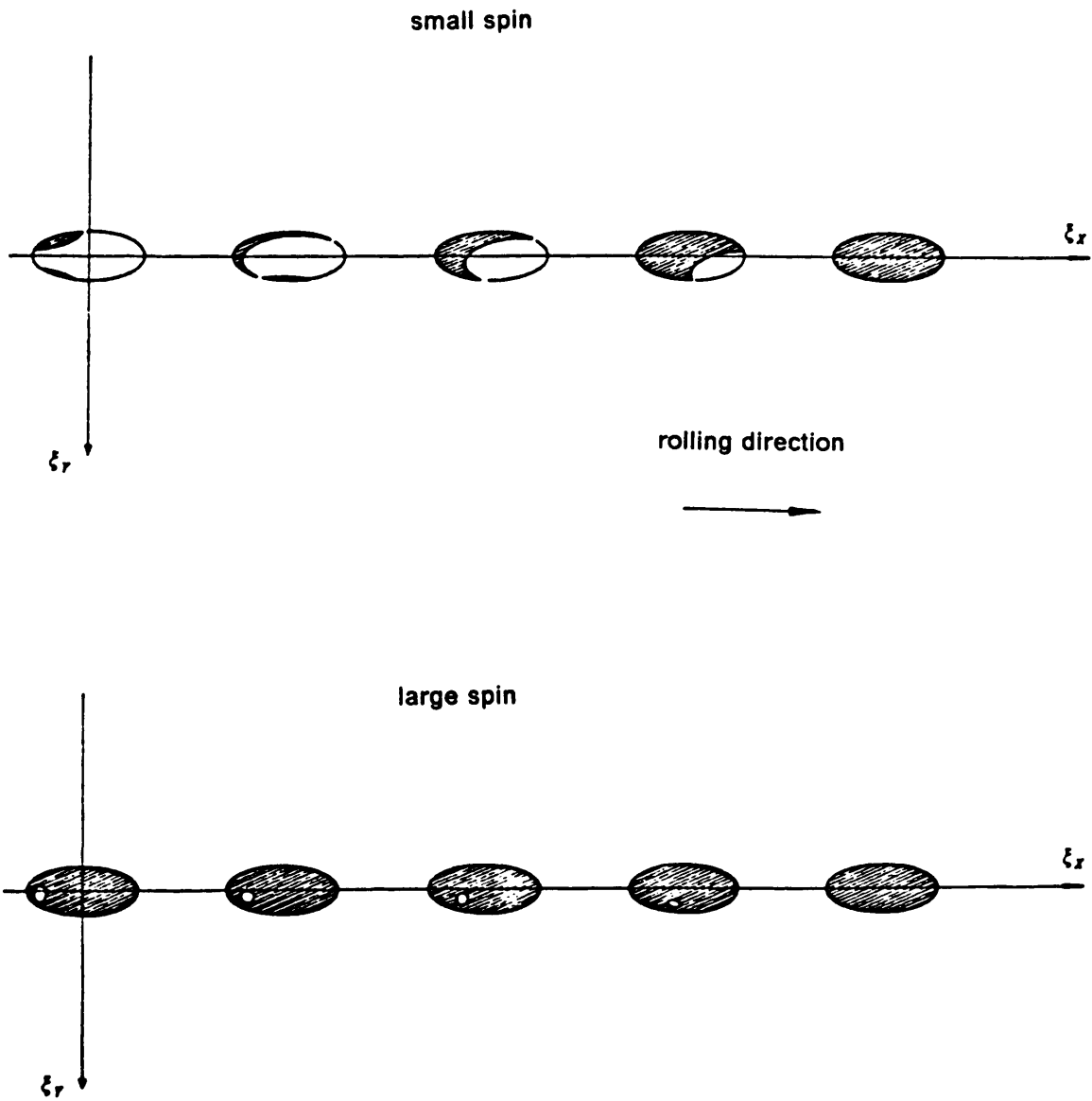
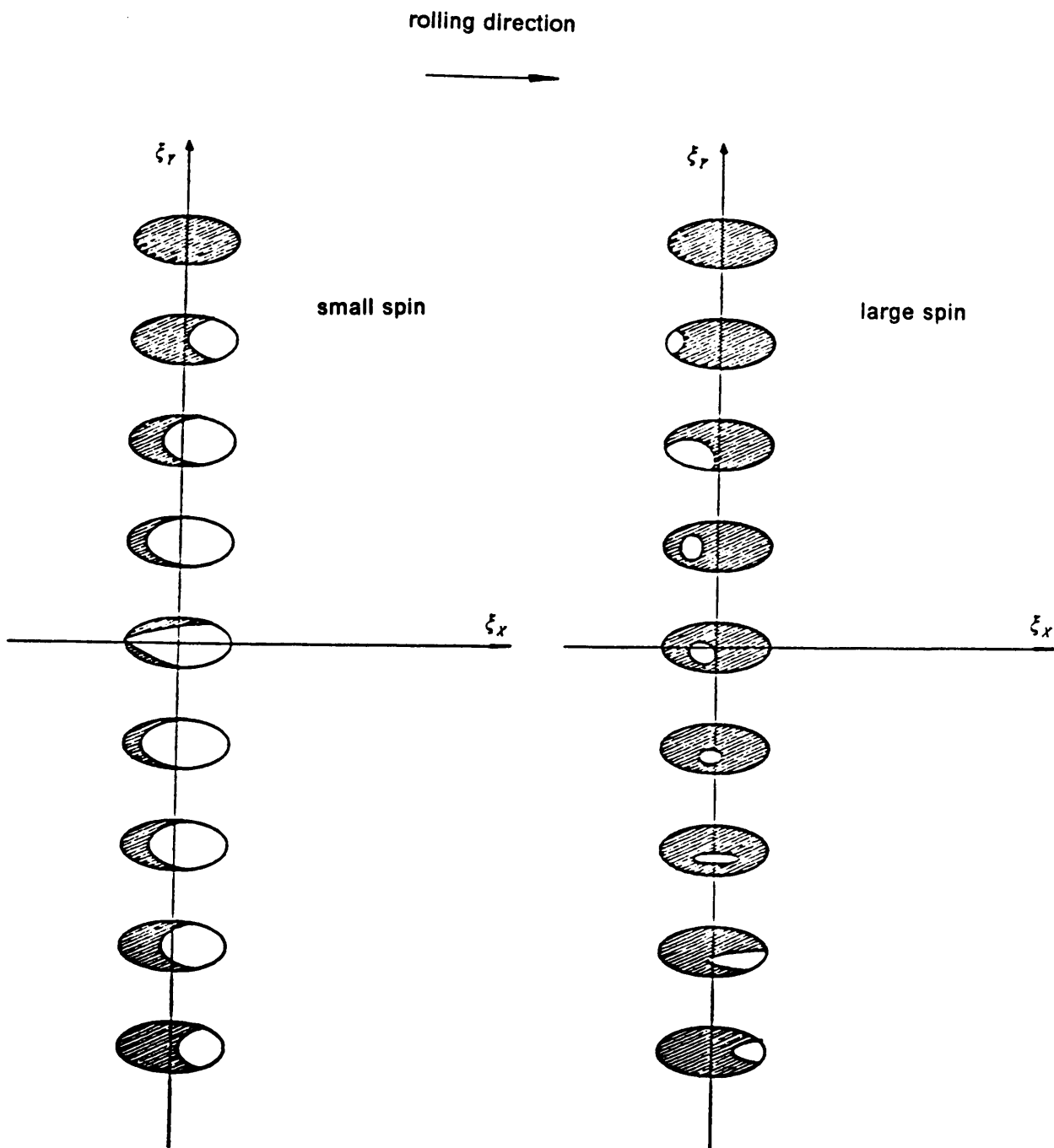


Figure 14. Slip/adhesion regions for zero lateral creepage



**Figure 15. Slip/adhesion regions for zero longitudinal creepage**

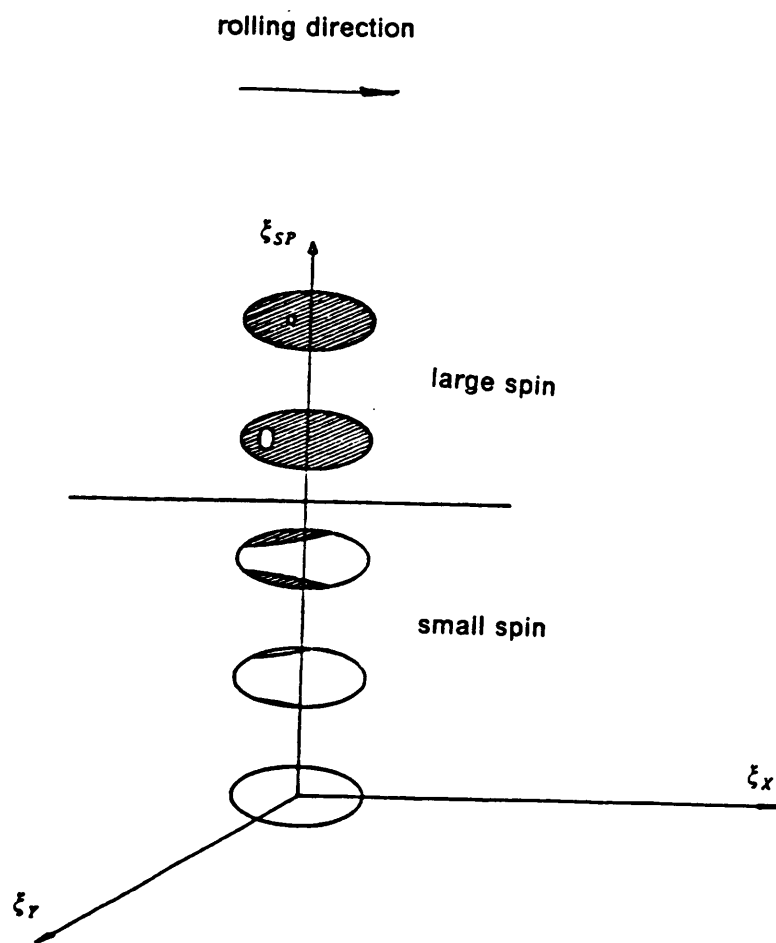
For large spin creepage, only a small region of adhesion exists. This adhesion region migrates around in the contact patch depending on the amount of lateral creepage present. It is at the trailing end of the contact patch for large lateral creepage, and at the leading edge of the contact patch for large negative lateral creepage.

Figure 16 shows the distribution of slip and adhesion for the same conditions as Fig. 13 except that the longitudinal and lateral creepages are zero. The slip and adhesion regions are symmetrical with respect to the x-axis for all cases in Fig. 16. For the small spin creepage case, the slip regions are at the edges of the contact patch. For the large spin creepage case, only a small region of adhesion exists. This adhesion region becomes progressively smaller as the spin creepage increases.

In order to visualize the distributions of creep force, moment, slip and work done at the contact patch, these quantities are plotted on 3-dimensional plots. Figures 17 and 18 show two typical cases. In these figures, the regions of slip and adhesion are shown in the upper left plot. The dots indicate regions of slip, so the direction of contact patch velocity vector is to the left. The upper right plot shows the contact patch work distribution. The remaining plots show the local creep force and creepage distributions within the contact patch.

The slip region shown in Fig. 17 results from positive longitudinal, lateral, and spin creepages. The slip region covers the trailing portion of the contact patch. The work is zero in the adhesion region and positive in the slip region, as expected. The longitudinal and lateral forces are about 2800 and 3800 lb respectively, and the spin moment is about 2 ft-lb. Obviously, the net contribution of the spin moment is small, but the spin creepage causes the slip region to be asymmetrical as shown.

Figure 18 shows results of a case with longitudinal creepage equal to zero. The lateral and spin creepages are sufficiently high to cause slip in the entire contact patch. The longitudinal and lateral creep forces are 0 and about 3300 lb respectively, and the spin moment is about

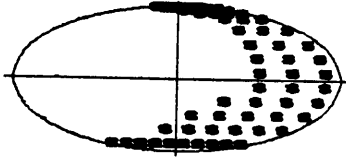


**Figure 16. Slip/adhesion regions for pure spin creepage**

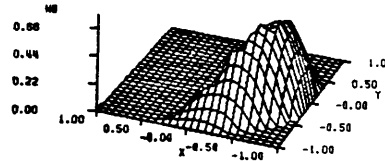
Longitudinal Creepage = 0.0019  
 Lateral Creepage = 0.0011  
 Spin Creepage = 0.1440 (1/FT)

A/B = 2.0  
 Friction Coef. = 0.6  
 Normal Force = 10000.0 (lb)

Slip/Adhesion Region at the Normalized Contact Patch

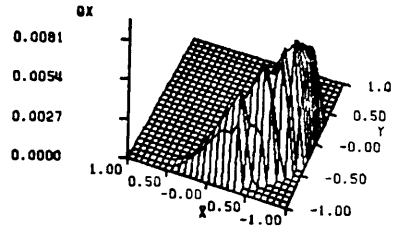
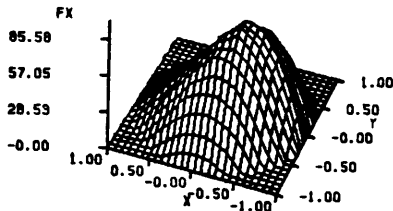


Work Done Distribution at the Normalized Contact Patch  
Wd = 9.796 (lb-ft)



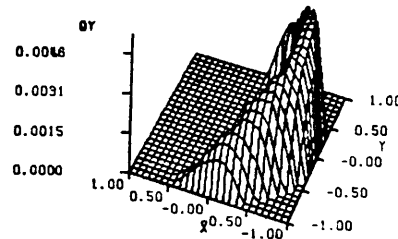
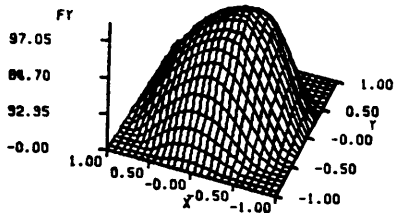
Longitudinal Creep Force Distribution at the Normalized Contact Patch  
Fx = 2780.860 (lb)

Longitudinal slip Distribution at the Normalized Contact Patch



Lateral Creep Force Distribution at the Normalized Contact Patch  
Fy = 3788.320 (lb)

Lateral Slip Distribution at the Normalized Contact Patch



Creep Moment Distribution at the Normalized Contact Patch  
Mz = 2.365 (lb-ft)

Spin Distribution At The Normalized Contact Patch

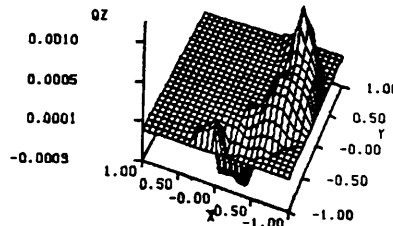
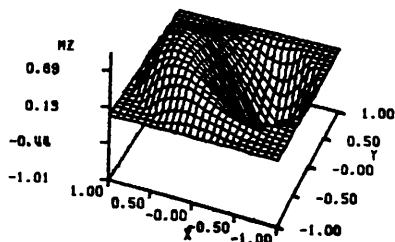
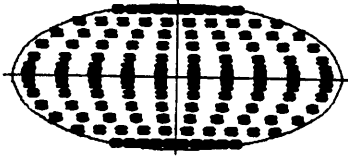


Figure 17. Distribution of creep force/moment, slip/spin, and work done for partial slip example

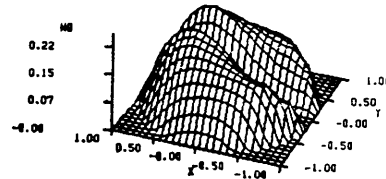
Longitudinal Creepage = 0.0000  
 Lateral Creepage = 0.0022  
 Spin Creepage = 0.5760 (1/FT)

A/B = 18  
 Friction Coef. = 0.6  
 Normal Force = 6345.8 (lb)

Slip/Adhesion Region at the Normalized Contact Patch

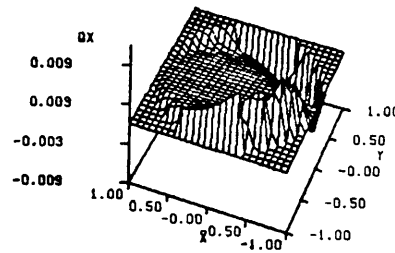
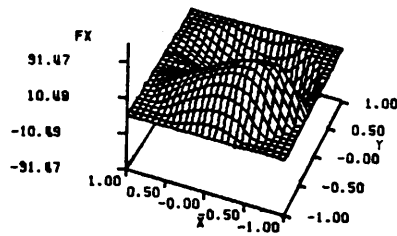


Work Done Distribution at the Normalized Contact Patch  
Wd = 12.906 (lb-ft)



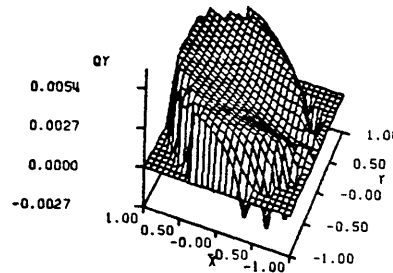
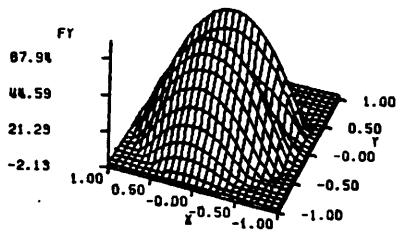
Longitudinal Creep Force Distribution at the Normalized Contact Patch  
Fx = 0.000 (lb)

Longitudinal slip Distribution at the Normalized Contact Patch



Lateral Creep Force Distribution at the Normalized Contact Patch  
Fy = 3255.332 (lb)

Lateral Slip Distribution at the Normalized Contact Patch



Creep Moment Distribution at the Normalized Contact Patch  
Mz = 9.971 (lb-ft)

Spin Distribution At The Normalized Contact Patch

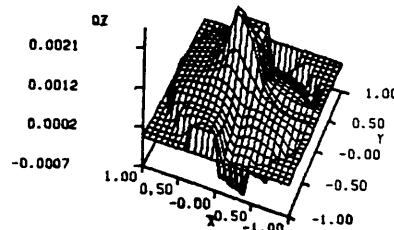
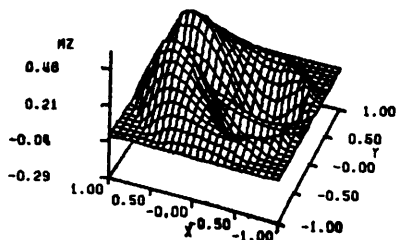


Figure 18. Distribution of creep force/moment, slip/spin, and work done for full slip example

10 ft-lb. Even though the net longitudinal force is zero, the longitudinal force distribution is not zero, as shown in the figure.

### **Summary**

1. This chapter discusses the wheel/rail rolling contact mechanics.
2. The concept of creepage is presented for rolling contact with slip and spin. The creepage expressions for a wheelset are presented.
3. Hertzian contact theory is introduced and used to calculate the contact area and contact stresses in the wheel/rail contact.
4. Kalker's simplified theory to determine the creep force and moment is discussed. Because the contact forces and moment are the external forces and moment acting on train, they are needed in the solutions of rail vehicle dynamics problem.
5. Several three-dimensional plots for the distribution of creep force, creep moment, slip, spin and work done have been presented for the typical cases of the wheel/rail rolling contact. These plots help to visualize the force, slip, and work distributions within the contact patch.
6. A series of plots shows how the slip and adhesion regions depend upon various combinations of longitudinal, lateral, and spin creepages.
7. The work presented in this chapter provides the basis for the wear computations discussed in chapter 4.

## **Chapter 3 : Analytical Dynamics Model for the Study of Wear Process**

Truck or car dynamic response is a problem that causes considerable concern. When the wear problem is treated, the effect of dynamic response is significant, because the dynamic response affects the wheel/rail contact position. The influence of the wheel/rail contact position on wear was introduced in chapter 2 and will be discussed further in Chapter 4. This chapter concentrates on the vehicle dynamics problem that must be solved in order to predict wheel wear.

In railway vehicle dynamics, people are interested in lateral stability and vertical response on tangent track or curved track. Garg and Dukkipati (1984) presented several dynamic models for different purposes. A 25-degree-of-freedom linear model was developed to investigate the hunting behavior of a freight car on tangent track. A 15-degree-of-freedom linear model was considered for the lateral stability of a passenger car on tangent track.

Usually, a car body is supported by two trucks each having two wheelsets. A wheelset is the basic component of a truck. The equations of motion of wheelset are derived in Appendix A and summarized in this chapter. The lateral and yaw equations are used to determine the

external force and moment, and the spin equation is used to obtain perturbation spin angle response.

For the purpose of investigating wheel wear, a 5-degree-of-freedom nonlinear half-car model is chosen to predict the truck motion on tangent track, and to obtain the contact position of the wheel on the rail and other wheel/rail geometric constraint functions which are discussed in Chapter 2. A complete description of the 5-degree-of-freedom half-car model is presented, and the equations of motion are summarized. See Appendix C for the derivation.

Track irregularity has a significant effect on truck response. A mathematical model generates random rail alignment as a position input for the system. In addition, the nonlinear Coulomb friction moment at the vehicle centerplate is simulated by a slider model as proposed by Heller et al.(1977b) for modeling Coulomb friction.

Finally, Runge-Kutta numerical integration is used to solve the nonlinear differential equations, and the dynamic response of the 5-degree-of-freedom half-car model is presented. In addition, The hunting phenomenon in railway dynamics is introduced.

### 3.1 Nomenclature

The nomenclature used in the development of the equations of motion is as follows:

$M_w$	=	mass of wheelset (slugs) (two for each truck)
$M_f$	=	mass of sideframe (slugs) (two for each truck)
$M_b$	=	mass of bolster (slugs) (one for each truck)
$M_c$	=	mass of car body (slugs)
$I_{wz}$	=	mass moment of inertia of wheelset in yaw direction (slugs-ft <sup>2</sup> )
$I_{fz}$	=	mass moment of inertia of sideframe in yaw direction (slugs-ft <sup>2</sup> )
$I_{bx}$	=	mass moment of inertia of bolster in roll direction (slugs-ft <sup>2</sup> )

$I_{Bz}$	=	mass moment of inertia of bolster in yaw direction (slugs-ft <sup>2</sup> )
$I_{Cx}$	=	mass moment of inertia of car body in roll direction (slugs-ft <sup>2</sup> )
$I_{Cz}$	=	mass moment of inertia of car body in yaw direction (slugs-ft <sup>2</sup> )
$K_{By}$	=	lateral spring stiffness of suspension (lb/ft)
$K_{Bz}$	=	vertical spring stiffness of suspension (lb/ft)
$K_{B\psi}$	=	yaw spring stiffness of suspension (lb/rad)
$K_{C\psi}$	=	yaw spring stiffness of car body (lb/rad)
$C_{By}$	=	lateral damping of suspension (lb-sec/ft)
$C_{Bz}$	=	vertical damping of suspension (lb-sec/ft)
$C_{B\psi}$	=	yaw damping of suspension (lb-ft-sec/rad)
$C_{C\psi}$	=	yaw damping of car body (lb-ft-sec/rad)
$H_1$	=	distance from c.g. of car body to wheelset c.g. (ft)
$H_2$	=	distance from c.g. of car body to bolster c.g. (ft)
$L$	=	half length between front and rear wheelsets (ft)
$D$	=	half length between right and left side frame (ft)
$A$	=	half wheel gauge (ft)
$V$	=	train velocity (mph)
$Y_T$	=	truck lateral displacement (ft)
$\Psi_T$	=	truck yaw angle (rad)
$\Psi_W$	=	truck warp angle (rad)
$Y_C$	=	car body lateral displacement (in)
$\Phi_C$	=	car body roll angle (rad)
$\dot{Y}_T$	=	truck lateral velocity (in/sec)
$\dot{\Psi}_T$	=	truck yaw angular velocity (rad/sec)
$\dot{\Psi}_W$	=	truck warp angular velocity (rad/sec)
$\dot{Y}_C$	=	car body lateral velocity (in/sec)
$\dot{\Phi}_C$	=	car body roll angular velocity (rad/sec)
$\zeta_x$	=	longitudinal creepage

$\xi_Y$	=	lateral creepage
$\xi_{SP}$	=	spin creepage (1/ft)
$R_R$	=	radius of right wheel at contact point (in)
$R_L$	=	radius of left wheel at contact point (in)
$R_0$	=	nominal radius of wheelset (in)
$\delta_R$	=	right contact angle (rad)
$\delta_L$	=	left contact angle (rad)
$\bar{\Phi}_W$	=	average wheelset roll angle (rad)
$\bar{Z}_W$	=	average wheelset vertical displacement (ft)
$\dot{\bar{\Phi}}_W$	=	average wheelset roll angular velocity (rad/sec)
$\dot{\bar{Z}}_W$	=	average wheelset vertical velocity (ft/sec)

### **Coordinates**

$X$	=	longitudinal direction
$Y$	=	lateral direction
$Z$	=	vertical direction
$\Phi$	=	roll angle
$\Theta$	=	pitch angle
$\Psi$	=	yaw angle

### **Subscript**

$W$	=	wheelset
$B$	=	bolster
$F$	=	sideframe
$C$	=	car body
$R$	=	right wheel
$L$	=	left wheel
$f$	=	front wheelset
$r$	=	rear wheelset

### **Subscript sequence**

$F_{XRF}$	=	force at X-direction on right-front wheel
$K_{BZ}$	=	bolster spring stiffness at Z-direction
$I_{BZ}$	=	mass moment of inertia of bolster at Z-direction

### 3.2 Wheelset Equations of Motion

The wheelset is a basic and important dynamic component of a truck. There are six degrees of freedom,

- $x$  = longitudinal displacement of wheelset mass center
- $y$  = lateral displacement of wheelset mass center
- $z$  = vertical displacement of wheelset mass center
- $\phi$  = roll angle of wheelset
- $\beta$  = perturbation spin angle of wheelset
- $\psi$  = yaw angle of wheelset

The rear view of a wheelset is shown in Fig. 19, and the derivation of the wheelset equations of motion are presented in Appendix A. A summary of the wheelset equations of motion are included here:

#### longitudinal equation

$$M\ddot{x} = F_{XL} + F_{XR} + N_{XL} + N_{XR} + F_{XS} \quad (3.1)$$

#### lateral equation

$$M\ddot{y} = F_{YL} + F_{YR} + N_{YL} + N_{YR} + F_{YS} \quad (3.2)$$

#### vertical equation

$$M\ddot{z} = F_{ZL} + F_{ZR} + N_{ZL} + N_{ZR} + F_{ZS} \quad (3.3)$$

#### roll equation

$$I_{WX}\ddot{\phi} - I_{WY}\Omega\dot{\psi} = R_{YR}(F_{ZR} + N_{ZR}) - R_{ZR}(F_{YR} + N_{YR}) + R_{YL}(F_{ZL} + N_{ZL}) - R_{ZL}(F_{YL} + N_{YL}) \\ + M_{XL} + M_{XR} + M_{XS} \quad (3.4)$$

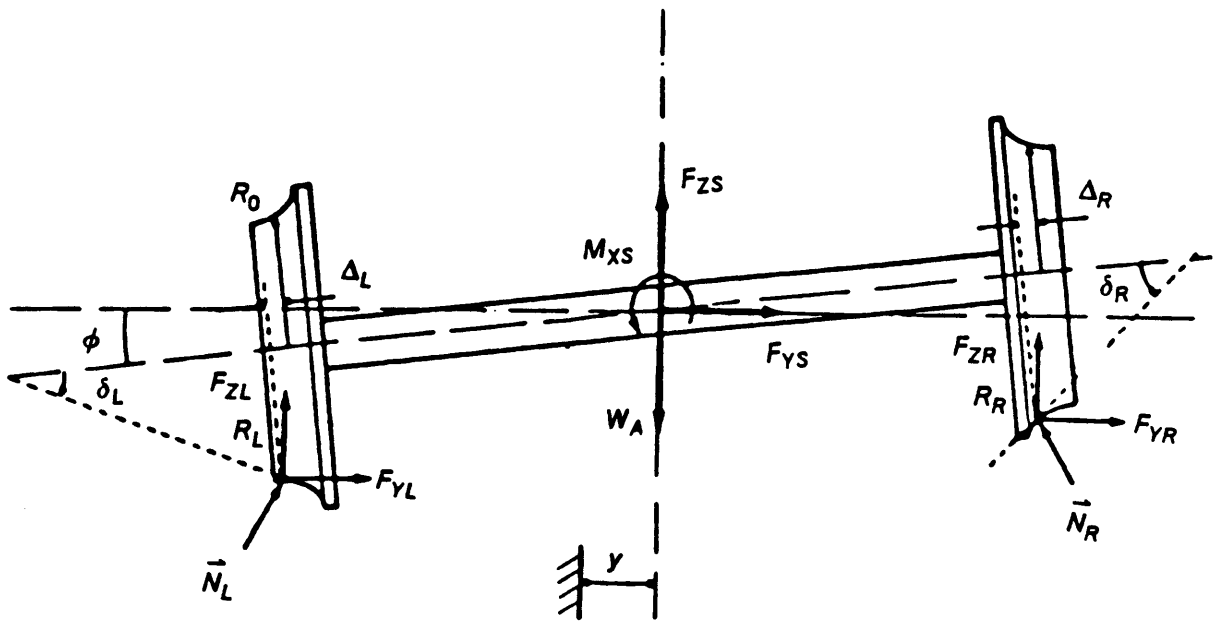


Figure 19. Rear view of a wheelset

**spin equation**

$$I_{WY}\ddot{\beta} = R_{ZR}(F_{XR} + N_{XR}) - R_{XR}(F_{ZR} + N_{ZR}) + R_{ZL}(F_{XL} + N_{XL}) - R_{XL}(F_{ZL} + N_{ZL}) \\ + M_{YL} + M_{YR} + M_{YS} \quad (3.5)$$

**yaw equation**

$$I_{WZ}\ddot{\psi} + I_{WY}\Omega\dot{\phi} = R_{YR}(F_{YR} + N_{YR}) - R_{YR}(F_{XR} + N_{XR}) + R_{XL}(F_{YL} + N_{YL}) - R_{YL}(F_{XL} + N_{XL}) \\ + M_{ZL} + M_{ZR} + M_{ZS} \quad (3.6)$$

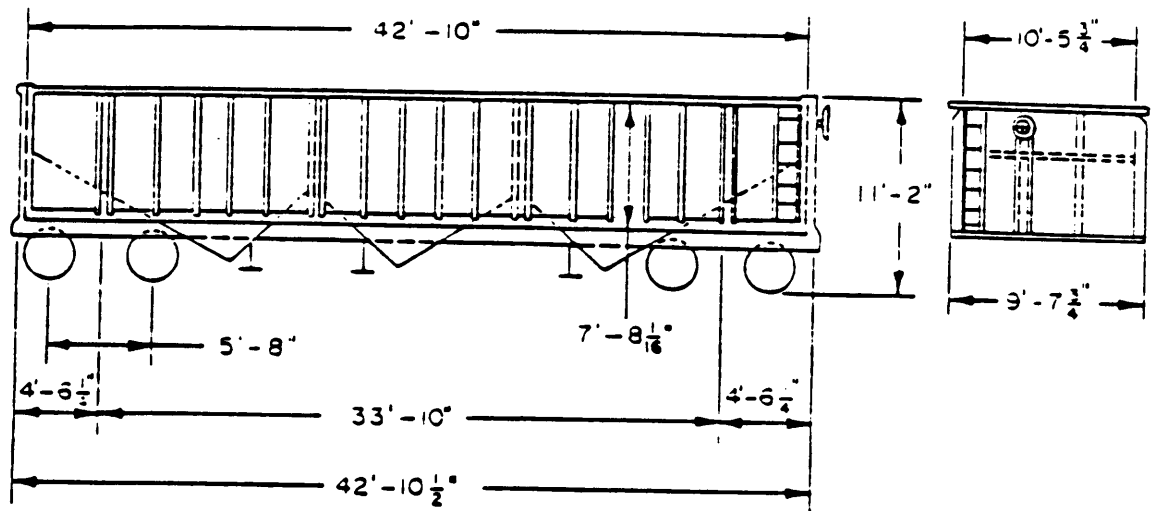
### 3.3 Five-Degree-of-Freedom Half-Car Model

A realistic simulation of truck dynamics is required for this work. The suspension system is modeled by equivalent suspension elements. The configuration of a half-car is adopted from the 80-ton open hopper car (Davila, 1986) shown in Fig. 20.

The 5 degrees of freedom are

- $Y_T$  = truck lateral displacement
- $\Psi_T$  = truck yaw angle
- $\Psi_W$  = truck warp angle
- $Y_C$  = car body lateral displacement
- $\Phi_C$  = car body roll angle

The schematic of the 5-degree-of-freedom half-car model are shown in Fig. 21. There are three degrees of freedom (lateral, yaw, and warp) for the truck, and two degrees of freedom (lateral and roll) for the half-car. Fig. 21 also defines a few other parameters that appear in the equations of motion. Assuming the vertical motion is small, it can be neglected as will be shown later. The wheelset external forces (A.75) and moments (A.76) for the front and rear



$M_w$	=	76.600 (slugs), mass of wheelset (two for each truck)
$M_f$	=	24.000 (slugs), mass of sideframe (two for each truck)
$M_b$	=	36.100 (slugs), mass of bolster (one for each truck)
$M_c$	=	1102.000 (slugs), mass of car body
$I_{wv}$	=	53.100 (slugs-ft <sup>2</sup> ), mass inertia of wheelset in spin direction
$I_{wz}$	=	448.500 (slugs-ft <sup>2</sup> ), mass inertia of wheelset in yaw direction
$I_{fz}$	=	77.600 (slugs-ft <sup>2</sup> ), mass inertia of sideframe in yaw direction
$I_{bx}$	=	178.600 (slugs-ft <sup>2</sup> ), mass inertia of bolster in roll direction
$I_{bz}$	=	178.600 (slugs-ft <sup>2</sup> ), mass inertia of bolster in yaw direction
$I_{cx}$	=	13000.000 (slugs-ft <sup>2</sup> ), mass inertia of car body in roll direction
$I_{cz}$	=	234000.000 (slugs-ft <sup>2</sup> ), mass inertia of car body in yaw direction
$K_{by}$	=	0.61930E+05 (lb/ft), lateral spring stiffness of suspension
$K_{bz}$	=	0.25715E+06 (lb/ft), vertical spring stiffness of suspension
$K_{b\psi}$	=	0.37290E+07 (lb-ft/rad), yaw spring stiffness of suspension
$K_{\theta}$	=	0.50000E+08 (lb-ft/rad), Rotation spring stiffness of centerplate (Fig. 23)
$F_{\theta}$	=	606.000 (lb-ft), breakout friction moment of centerplate
$C_{by}$	=	0.43248E+05 (lb-sec/ft), lateral damping coefficient of suspension
$C_{bz}$	=	0.40803E+05 (lb-sec/ft), vertical damping coefficient of suspension
$C_{b\psi}$	=	0.80854E+05 (lb-ft-sec/rad), yaw damping coefficient of suspension
$C_{c\psi}$	=	0.12280E+05 (lb-ft-sec/rad), yaw damping coefficient of centerplate
$H_1$	=	2.994 (ft), distance from c.g. of carbody to wheelset center line
$H_2$	=	2.994 (ft), distance from c.g. of carbody to c.g. of bolster
$L$	=	2.833 (ft), half length between front and rear wheelsets
$D$	=	3.250 (ft), half length between right and left sideframe
$A$	=	2.208 (ft), half wheel gauge

Figure 20. Configuration of the 80-ton open hopper car

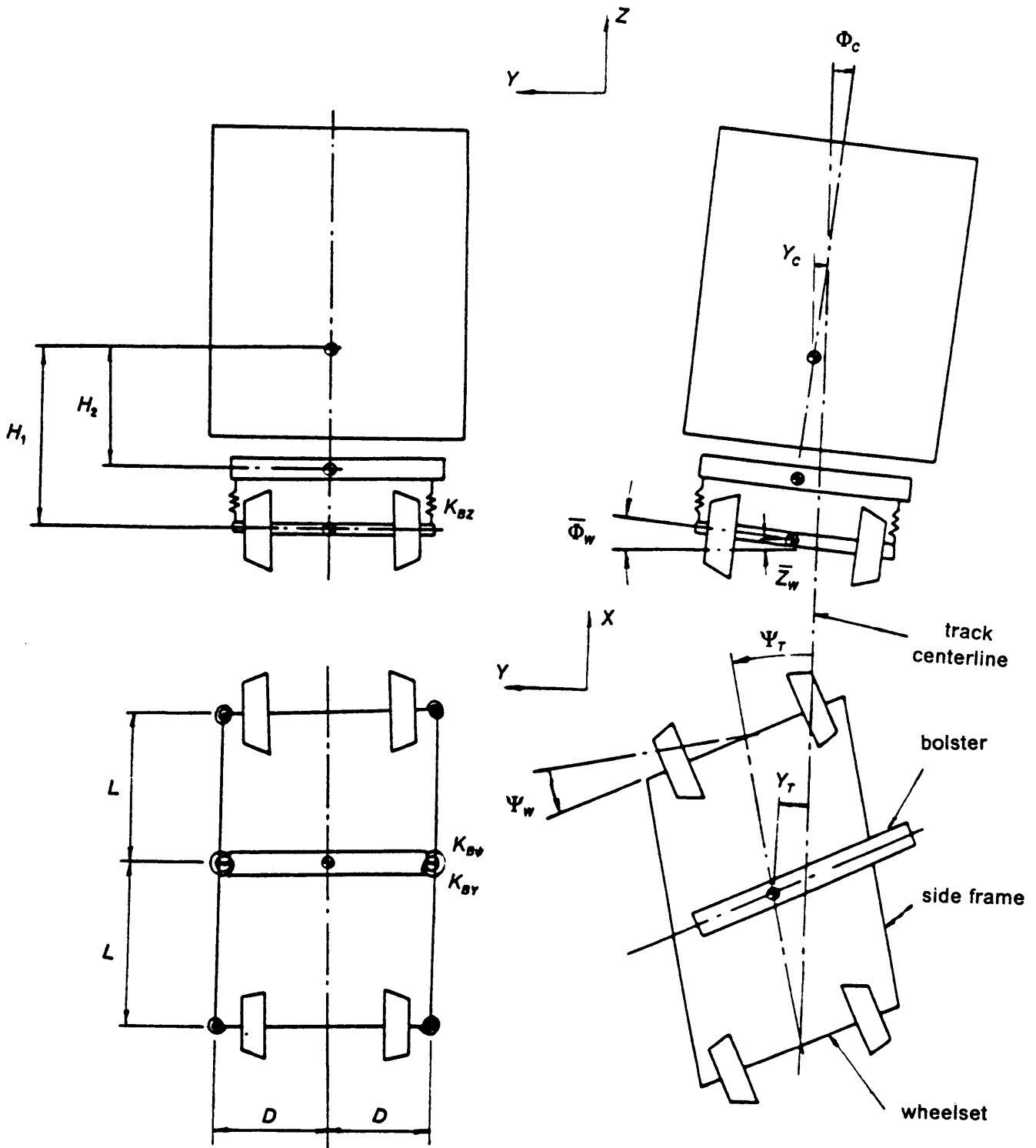


Figure 21. Schematic of 5 d.o.f. half-car model

wheelsets are obtained from the lateral and yaw equations of motion. By omitting the high order terms, the wheelset external forces become

$$F_f = (F'_{XLf} + F'_{XRf})(\Psi_W + \Psi_T) + (F'_{YLf} + F'_{YRf}) - W_A \left( \frac{\delta_{Lf} - \delta_{Rf}}{2} + \Phi_{Wf} \right) \quad (3.7)$$

$$F_r = (F'_{XLr} + F'_{XRr})(\Psi_W + \Psi_T) + (F'_{YLr} + F'_{YRr}) - W_A \left( \frac{\delta_{Lr} - \delta_{Rr}}{2} + \Phi_{Wr} \right) \quad (3.8)$$

where

- $F_f$  = front-wheelset external force
- $F_r$  = rear-wheelset external force
- $F'_{XLf}$  = left-front wheel creep force at X-direction
- $F'_{YLf}$  = left-front wheel creep force at Y-direction
- $F'_{XRf}$  = right-front wheel creep force at X-direction
- $F'_{YRf}$  = right-front wheel creep force at Y-direction
- $F'_{XLr}$  = left-rear wheel creep force at X-direction
- $F'_{YLr}$  = left-rear wheel creep force at Y-direction
- $F'_{XRr}$  = right-rear wheel creep force at X-direction
- $F'_{YRr}$  = right-rear wheel creep force at Y-direction
- $W_A$  = load of front wheelset (nearly one-fourth total weight)
- $\delta_{Lf}$  = left-front wheel contact angle
- $\delta_{Rf}$  = right-front wheel contact angle
- $\delta_{Lr}$  = left-rear wheel contact angle
- $\delta_{Rr}$  = right-rear wheel contact angle
- $\Phi_{Wf}$  = front wheelset roll angle
- $\Phi_{Wr}$  = rear wheelset roll angle

and the wheelset external moments become

$$M_f = A(F'_{XRf} - F'_{XLf}) + (F'_{XRf}\Delta_{Rf} + F'_{XLf}\Delta_{Lf}) - (F'_{YRf}R_{Rf} + F'_{YLf}R_{Lf})\Phi_{Wf}$$

$$+ M'_{ZLf} + M'_{ZRf} \quad (3.9)$$

$$M_r = A(F'_{XRr} - F'_{XLr}) + (F'_{XRr}\Delta_{Rr} + F'_{XLr}\Delta_{Lr}) - (F'_{XRr}R_{RR} + F'_{XLr}R_{LR})\Phi_{Wr}$$

$$+ M'_{ZLr} + M'_{ZRr} \quad (3.10)$$

where

- $M_f$  = front-wheelset external moment
- $M_r$  = rear-wheelset external moment
- $M'_{ZLf}$  = left-front wheel creep moment at Z-direction
- $M'_{ZRf}$  = right-front wheel creep moment at Z-direction
- $M'_{ZLr}$  = left-rear wheel creep moment at Z-direction
- $M'_{ZRr}$  = right-rear wheel creep moment at Z-direction
- $\Delta_{Lf}$  = distance from tapeline to contact point for left-front wheel
- $\Delta_{Rf}$  = distance from tapeline to contact point for right-front wheel
- $\Delta_{Lr}$  = distance from tapeline to contact point for left-rear wheel
- $\Delta_{Rr}$  = distance from tapeline to contact point for right-rear wheel
- $A$  = half wheel gauge

The equations of motion for the 5-degree-of-freedom half-car model are derived in Appendix C and summarized as follows:

$$\begin{bmatrix} M_T & 0 & 0 & 0 & 0 \\ 0 & I_{TT} & I_{TW} & 0 & 0 \\ 0 & I_{TW} & I_{WW} & 0 & 0 \\ 0 & 0 & 0 & M_{BC} & M_B H_2 \\ 0 & 0 & 0 & M_B H_2 & I_{CC} \end{bmatrix} \begin{bmatrix} \ddot{Y}_T \\ \ddot{\Psi}_T \\ \ddot{\Psi}_W \\ \ddot{Y}_C \\ \ddot{\Phi}_C \end{bmatrix}$$

$$\begin{aligned}
& + \begin{bmatrix} 2C_{BY} & 0 & 0 & -2C_{BY} & -2C_{BY}H_2 \\ 0 & C_{C\Psi} & C_{C\Psi} & 0 & 0 \\ 0 & C_{C\Psi} & C_{BC} & 0 & 0 \\ -2C_{BY} & 0 & 0 & 2C_{BY} & 2C_{BY}H_2 \\ -2C_{BY}H_2 & 0 & 0 & 2C_{BY}H_2 & C_{CC} \end{bmatrix} \begin{bmatrix} \dot{Y}_T \\ \dot{\Psi}_T \\ \dot{\Psi}_W \\ \dot{Y}_C \\ \dot{\Phi}_C \end{bmatrix} \\
& + \begin{bmatrix} 2K_{BY} & 0 & 0 & -2K_{BY} & -2K_{BY}H_2 \\ 0 & K_{C\Psi} & K_{C\Psi} & 0 & 0 \\ 0 & K_{C\Psi} & K_{BC} & 0 & 0 \\ -2K_{BY} & 0 & 0 & 2K_{BY} & 2K_{BY}H_2 \\ -2K_{BY}H_2 & 0 & 0 & 2K_{BY}H_2 & K_{CC} \end{bmatrix} \begin{bmatrix} Y_T \\ \Psi_T \\ \Psi_W \\ Y_C \\ \Phi_C \end{bmatrix} \\
& = \begin{bmatrix} F_f + F_r \\ M_f + M_r + (F_f - F_r)L \\ M_f + M_r \\ 0 \\ 2C_{BZ}D^2\dot{\Phi}_W + 2K_{BZ}D^2\bar{\Phi}_W \end{bmatrix} \tag{3.11}
\end{aligned}$$

### ***Nonlinear Coulomb Friction***

The damping in the centerplate is provided by dry or Coulomb friction. A slider model for Coulomb friction moment is developed to simulate the Coulomb friction nonlinearity (Heller et al., 1977b) The realistic characteristic curve is shown in Fig. 22. The top of Fig. 22 is the ideal characteristic curve of Coulomb friction, and the bottom is the characteristic curve of the slider model. The schematic of the slider model for Coulomb friction moment is presented in Fig. 23. The model includes an inertialess rotational slider and a stiff rotational spring. The slider model is valid for the entire frequency without accuracy problems near resonance and

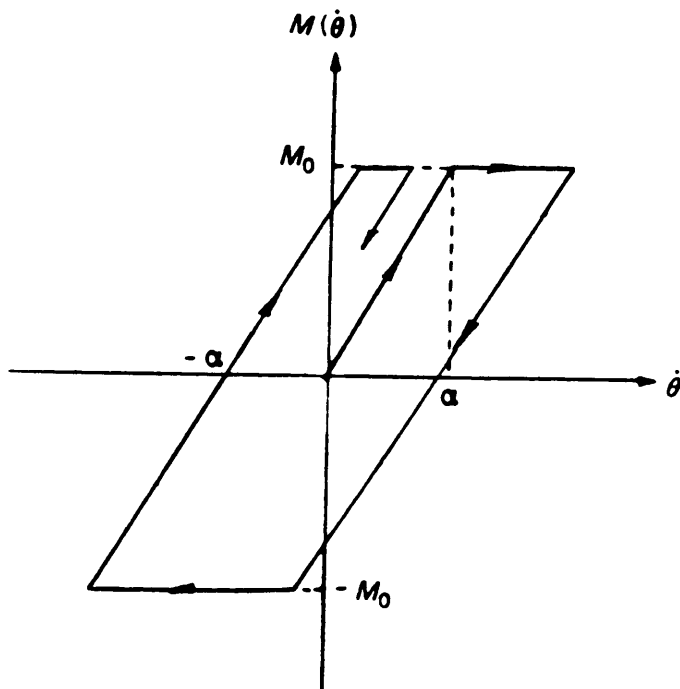
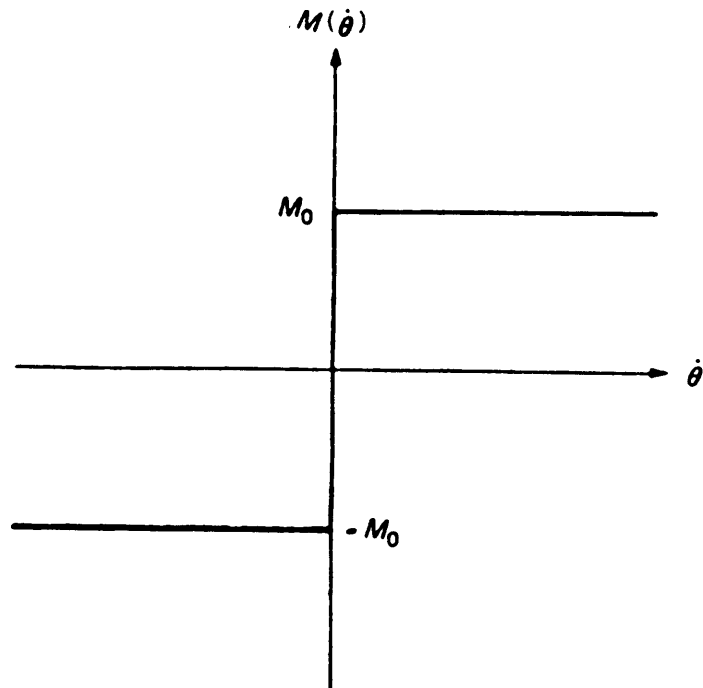
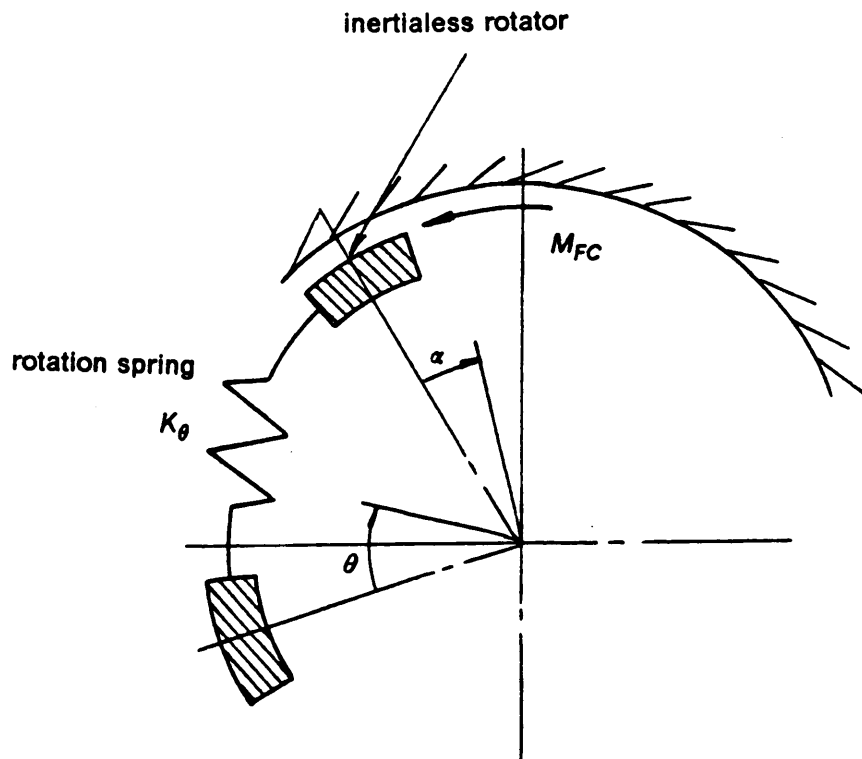


Figure 22. Characteristic curve for Coulomb friction



**Figure 23. Scheme of slider model for rotation Coulomb friction**

does not require integration step changes as model parameters change. The characteristics of the model are verified by Heller et al. (1977b).

The characteristics are

$$\text{if } |M| < M_0, \text{ then } \dot{\alpha} = 0 \quad (3.12)$$

$$\text{if } |M| \geq M_0, \text{ then } \dot{\alpha} = \dot{\theta} \quad (3.13)$$

where

$M$  = friction moment for centerplate

$M_0$  = breakout friction moment

$\alpha$  = rotation angle of inertialess body,  $I_1$

$\theta$  = rotation angle between car body and centerplate

In order to determine  $\alpha$ , further restrictions, when  $|M| \geq M_0$ , are

$$\text{if } \dot{\alpha} = \dot{\theta} > 0, \text{ then } \alpha = \theta - \frac{M_0}{K_\theta} \quad (3.14)$$

$$\text{if } \dot{\alpha} = \dot{\theta} < 0, \text{ then } \alpha = \theta + \frac{M_0}{K_\theta} \quad (3.15)$$

$$\text{if } \dot{\alpha} = \dot{\theta} = 0, \text{ then } \alpha = \theta \quad (3.16)$$

such that the Coulomb friction moment becomes

$$M_{FC} = K_\theta(\alpha - \theta) \quad (3.17)$$

where

$M_{FC}$  = Coulomb friction moment for centerplate

$K_\theta$  = equivalent yaw spring stiffness for centerplate

By substituting Coulomb friction moment into eq. (3.11), the equations of motion become

$$\begin{aligned}
 & \begin{bmatrix} M_T & 0 & 0 & 0 & 0 \\ 0 & I_{TT} & I_{TW} & 0 & 0 \\ 0 & I_{TW} & I_{WW} & 0 & 0 \\ 0 & 0 & 0 & M_{BC} & M_B H_2 \\ 0 & 0 & 0 & M_B H_2 & I_{CC} \end{bmatrix} \begin{bmatrix} \ddot{Y}_T \\ \ddot{\Psi}_T \\ \ddot{\Psi}_W \\ \ddot{Y}_C \\ \ddot{\Phi}_C \end{bmatrix} \\
 & + \begin{bmatrix} 2C_{BY} & 0 & 0 & -2C_{BY} & -2C_{BY}H_2 \\ 0 & C_{C\Psi} & C_{C\Psi} & 0 & 0 \\ 0 & C_{C\Psi} & C_{BC} & 0 & 0 \\ -2C_{BY} & 0 & 0 & 2C_{BY} & 2C_{BY}H_2 \\ -2C_{BY}H_2 & 0 & 0 & 2C_{BY}H_2 & C_{CC} \end{bmatrix} \begin{bmatrix} \dot{Y}_T \\ \dot{\Psi}_T \\ \dot{\Psi}_W \\ \dot{Y}_C \\ \dot{\Phi}_C \end{bmatrix} \\
 & + \begin{bmatrix} 2K_{BY} & 0 & 0 & -2K_{BY} & -2K_{BY}H_2 \\ 0 & 0 & 0 & 0 & 0 \\ 0 & 0 & K_{B\Psi} & 0 & 0 \\ -2K_{BY} & 0 & 0 & 2K_{BY} & 2K_{BY}H_2 \\ -2K_{BY}H_2 & 0 & 0 & 2K_{BY}H_2 & K_{CC} \end{bmatrix} \begin{bmatrix} Y_T \\ \Psi_T \\ \Psi_W \\ Y_C \\ \Phi_C \end{bmatrix} \\
 & = \begin{bmatrix} F_f + F_r \\ M_f + M_r + (F_f - F_r)L + M_{FC} \\ M_f + M_r + M_{FC} \\ 0 \\ 2C_{BZ}D^2\dot{\Phi}_W + 2K_{BZ}D^2\overline{\Phi}_W \end{bmatrix} \tag{3.18}
 \end{aligned}$$

### 3.4 Random Rail Alignment Generation

There are four important irregularities in track geometry, gauge, crosslevel, lateral alignment, and vertical surface profile. The definitions are as follows:

**gauge** horizontal distance between two rails measured between the heads of rail in the plane  $\frac{5}{8}$  in. below the top of the rail

**crosslevel** difference between the elevation of two rails

**lateral alignment** average of the lateral positions of two rails

**vertical surface profile** average of elevation of two rails

These definitions are illustrated in Fig. 24. Many mathematical models have been developed to describe these irregularity properties. White et al. (1978) used a PSD model for both lateral alignment and vertical surface profile. Detwiler and Nagurka (1983) used a PSD model for lateral alignment, gauge, and crosslevel. More recently, Fries and Coffey (1986) have developed a state-space approach to simulate the vertical and crosslevel rail irregularities.

In this work, only the lateral alignment irregularity is taken into account, since the lateral response is required when considering the wear problem. The gauge, crosslevel and vertical surface profiles are assumed uniform. The rail lateral alignment provides the input to the 5-degree-of-freedom half-car model. The PSD model for lateral alignment (White et al., 1978) is given by

$$S(\Omega_s) = \frac{A_A \Omega_c^2}{(\Omega_s^2 + \Omega_r^2)(\Omega_s^2 + \Omega_c^2)} \quad (3.19)$$

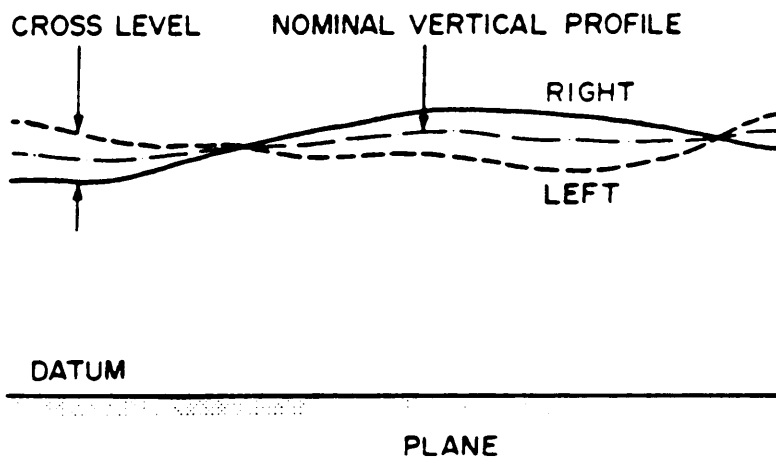
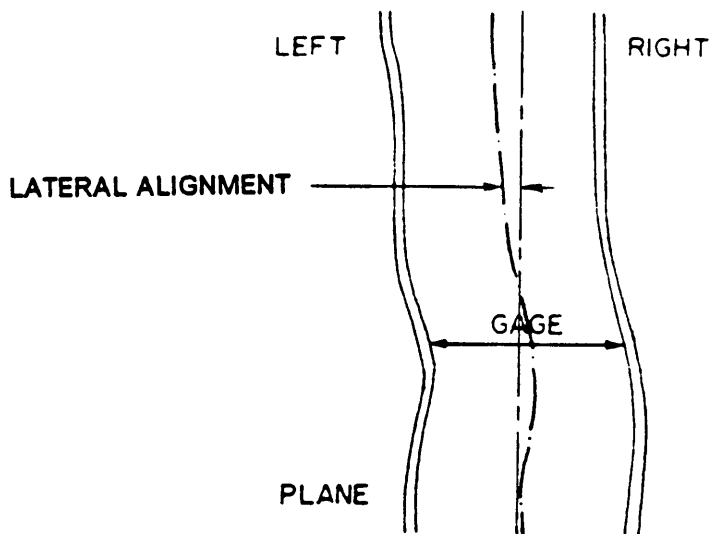


Figure 24. Illustration of track irregularity (Garg and Dukkipati, 1984)

where

- $S(\Omega_s)$  = lateral alignment power spectral density,  $\frac{\text{ft}^2}{\text{rad/ft}}$
- $\Omega_s$  = spatial frequency,  $\frac{2\pi}{\lambda}$
- $\lambda$  = wavelength
- $\Omega_c$  = critical wave number corresponding to a 25-ft wavelength,  
 $\Omega_c = \frac{2\pi}{25} \left( \frac{\text{rad}}{\text{ft}} \right)$
- $\Omega_r$  = critical wave number corresponding to a 1000-ft,  $\Omega_r = \frac{2\pi}{1000} \left( \frac{\text{rad}}{\text{ft}} \right)$
- $A_A$  = scale factor for lateral alignment (ft)
- class 4 :  $A_A = 4.429 \times 10^{-5}$  (ft)
- class 5 :  $A_A = 1.102 \times 10^{-5}$  (ft)
- class 6 :  $A_A = 4.921 \times 10^{-6}$  (ft)

This model was implemented in the algorithm developed by Fries and Coffey (1987) for use in this work.

### 3.5 Solution Method

In general, the equations of motion for a multiple-degree-of-freedom system have the form

$$[M] \{\ddot{X}\} + [C] \{\dot{X}\} + [K] \{X\} = \{F(t)\} \quad (3.20)$$

where

- $[M]$  = mass matrix
- $[C]$  = damping matrix
- $[K]$  = spring matrix
- $\{X\}$  = displacement vector
- $\{\dot{X}\}$  = velocity vector
- $\{\ddot{X}\}$  = acceleration vector
- $\{F(t)\}$  = force vector

This form is expressed in equation (3.18). Because the equations of motion include the non-linear Coulomb friction moment, ( $M_{Fc}$ ), the linear approaches, such as Laplace Transformation, are not suitable. The most common method used to solve this problem is the Runge-Kutta method. In order to apply the Runge-Kutta method, the equations of motion are manipulated into simultaneous first-order ordinary differential equations. The general forms are

$$\begin{aligned} \frac{dy_1}{dx} &= f_1(x, y_1, y_2, \dots, y_n) \\ \frac{dy_2}{dx} &= f_2(x, y_1, y_2, \dots, y_n) \\ &\vdots \\ \frac{dy_n}{dx} &= f_n(x, y_1, y_2, \dots, y_n) \end{aligned} \tag{3.21}$$

with initial conditions given at a common point,  $x_0$

$$\begin{aligned} y_1(x_0) &= y_{1,0} \\ y_2(x_0) &= y_{2,0} \\ &\vdots \\ y_n(x_0) &= y_{n,0} \end{aligned} \tag{3.22}$$

An IMSL subroutine named DVERK (IMSL, 1982), which implements a sixth order Runge-Kutta solver, has been used to solve the differential equations in this work.

For the numerical solution, the five second-order differential equations are transformed into ten first-order simultaneous differential equations. Let

$$\begin{aligned}
Z_1 &= Y_T & Z_6 &= \dot{Y}_T \\
Z_2 &= \Psi_T & Z_7 &= \dot{\Psi}_T \\
Z_3 &= \Psi_W & Z_8 &= \dot{\Psi}_W \\
Z_4 &= Y_C & Z_9 &= \dot{Y}_C \\
Z_5 &= \Phi_C & Z_{10} &= \dot{\Phi}_C
\end{aligned} \tag{3.23}$$

then, the equations become

$$\begin{aligned}
\dot{Z}_8 &= \frac{1}{M_T} \{ F_{Yfr} - W_A \Phi_{(r+n)} - 2C_{BY}(Z_8 - H_2 Z_{10} - Z_9) \\
&\quad - 2K_{BY}(Z_1 - H_2 Z_5 - Z_4) + F_{Xfr}(Z_2 + Z_3) \}
\end{aligned} \tag{3.24}$$

$$I_{TT}\dot{Z}_7 + I_{TW}\dot{Z}_8 = Q_1 \tag{3.25}$$

$$I_{TW}\dot{Z}_7 + I_{WW}\dot{Z}_8 = Q_2 \tag{3.26}$$

$$M_{BC}\dot{Z}_9 + M_B H_2 \dot{Z}_{10} = S_1 \tag{3.27}$$

$$M_B H_2 \dot{Z}_9 + I_{CC}\dot{Z}_{10} = S_2 \tag{3.28}$$

where

$$\begin{aligned}
Q_1 &= (AF_{X(R-L)} + LF_{Y(r-n)} + W_A \Phi_{(r-n)} + F_\Delta - F_\Phi + M_{Zfr}) \\
&\quad + (M_{FF} - K_{C\Psi})(Z_2 + Z_3) + M_{FC}
\end{aligned} \tag{3.29}$$

$$\begin{aligned}
Q_2 &= (AF_{X(R-L)} + F_\Delta - F_\Phi + M_{Zfr}) - C_{B\Psi}Z_8 - K_{C\Psi}Z_2 - K_{BC}Z_3 \\
&\quad M_{fr}(Z_2 + Z_3) + M_{FC}
\end{aligned} \tag{3.30}$$

$$S_1 = 2C_{BY}(Z_8 - H_2Z_{10} - Z_9) + 2K_{BY}(Z_1 - H_2Z_5 - Z_4) \quad (3.31)$$

$$S_2 = (2C_{BZ}D^2\bar{\Phi}_W + 2K_{BZ}D^2\bar{\Phi}_W) - 2C_{BY}H_2(Z_9 - Z_6) - C_{CC}Z_{10} \\ - 2K_{BY}H_2(Z_4 - Z_1) - K_{CC}Z_5 \quad (3.32)$$

Therefore,  $\dot{Z}_7$ ,  $\dot{Z}_8$ ,  $\dot{Z}_9$  and  $\dot{Z}_{10}$  can be solved in terms of  $(Z_1, Z_2, \dots, Z_{10})$ , so that the simultaneously differential equations similar to (3.21) are

$$\dot{Z}_1 = Z_6 \quad (3.33)$$

$$\dot{Z}_2 = Z_7 \quad (3.34)$$

$$\dot{Z}_3 = Z_8 \quad (3.35)$$

$$\dot{Z}_4 = Z_9 \quad (3.36)$$

$$\dot{Z}_5 = Z_{10} \quad (3.37)$$

$$\dot{Z}_6 = \frac{1}{M_T} \{F_{Yfr} - W_A\Phi_{(r+\eta)} - 2C_{BY}(Z_8 - H_2Z_{10} - Z_9) \\ - 2K_{BY}(Z_1 - H_2Z_5 - Z_4) + F_{Xfr}(Z_2 + Z_3)\} \quad (3.38)$$

$$\dot{Z}_7 = \frac{(Q_1I_{WW} - Q_2I_{TW})}{\Delta_1} \quad (3.39)$$

$$\dot{Z}_8 = \frac{(Q_2I_{TT} - Q_1I_{TW})}{\Delta_1} \quad (3.40)$$

$$\dot{Z}_9 = \frac{(S_1I_{CC} - S_2M_BH_2)}{\Delta_2} \quad (3.41)$$

$$\dot{Z}_{10} = \frac{(S_2M_{BC} - S_1M_BH_2)}{\Delta_2} \quad (3.42)$$

where

$$\Delta_1 = \begin{vmatrix} I_{TT} & I_{TW} \\ I_{TW} & I_{WW} \end{vmatrix} = I_{TT}I_{WW} - I_{TW}^2 \quad (3.43)$$

$$\Delta_2 = \begin{vmatrix} M_{BC} & M_B H_2 \\ M_B H_2 & I_{CC} \end{vmatrix} = M_{BC}I_{CC} - (M_B H_2)^2 \quad (3.44)$$

and the initial condition for  $t_0 = 0$

$$\dot{z}_1(0) = 0 \quad (3.45)$$

$$\dot{z}_2(0) = 0 \quad (3.46)$$

⋮

$$\dot{z}_{10}(0) = 0 \quad (3.47)$$

### 3.6 Result of Dynamic Response

Two cases of dynamics response of the 5-degree-of-freedom nonlinear half-car model are presented. Figure 25, 26 and 27 show the time domain response of the empty car running at the speed of 45 mph (66 fps). Fig. 25 shows the truck lateral displacement and the rail lateral alignment. The two thin curves are the rail lateral alignments for the front and rear wheelset and the thick curve is the truck lateral displacement. The rail random lateral alignments vary along the rail centerline, which is straight, and the truck lateral displacement generally follows the rail alignments.

### Truck Lateral Displacement ( in ) & Rail Lateral Alignment ( in )

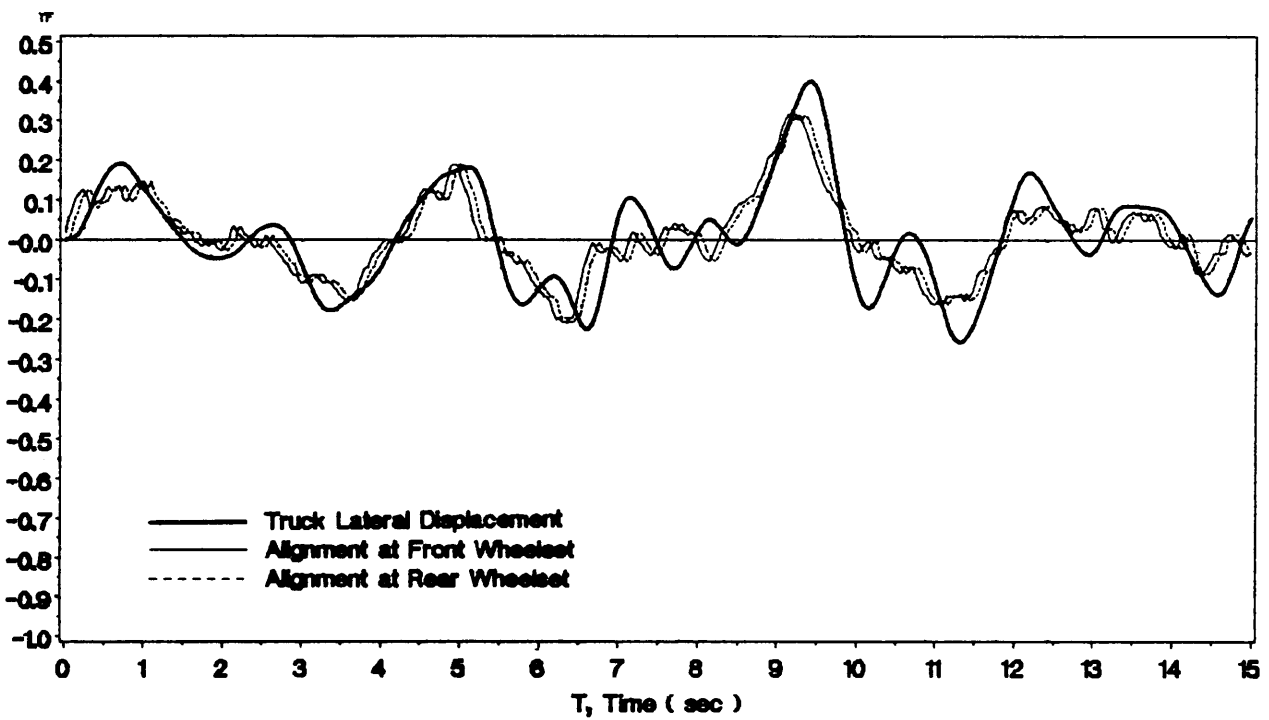


Figure 25. Truck lateral displacement and rail lateral alignment (45 mph)

### Front/Rear Wheelset Lateral Displacement ( in )

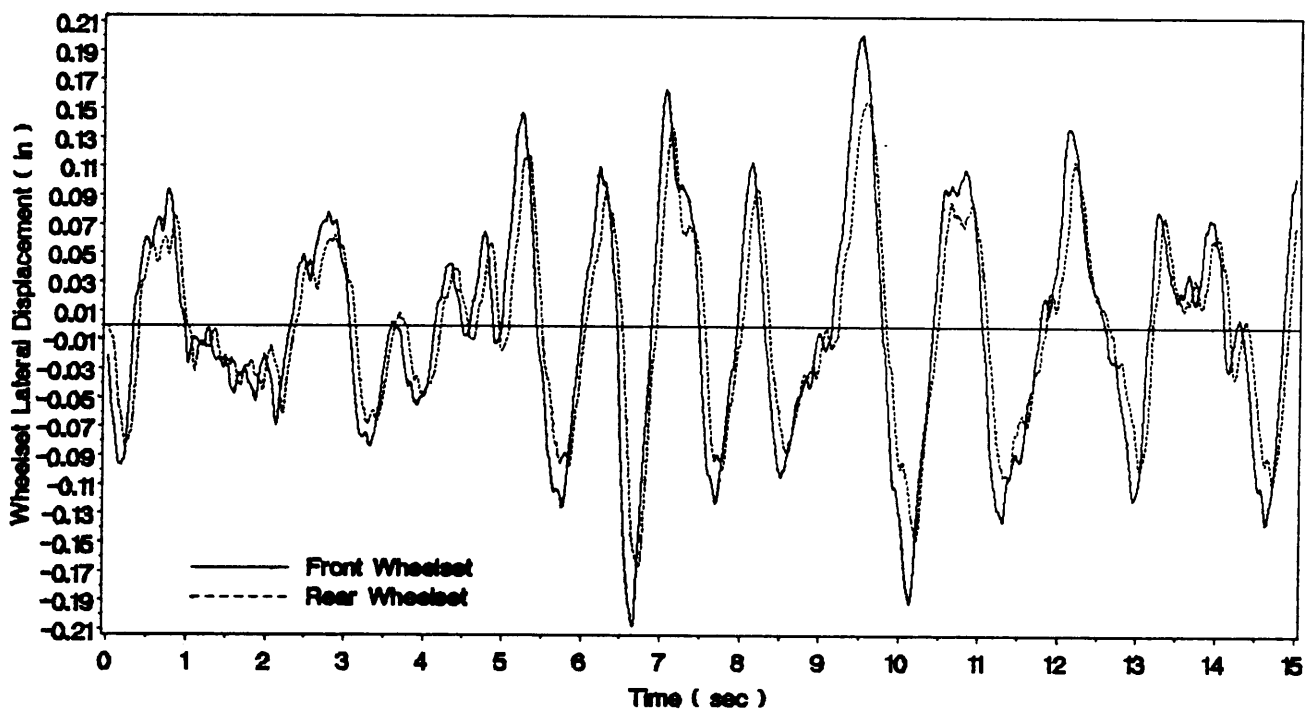


Figure 26. Front and rear wheelset lateral displacements (45 mph)

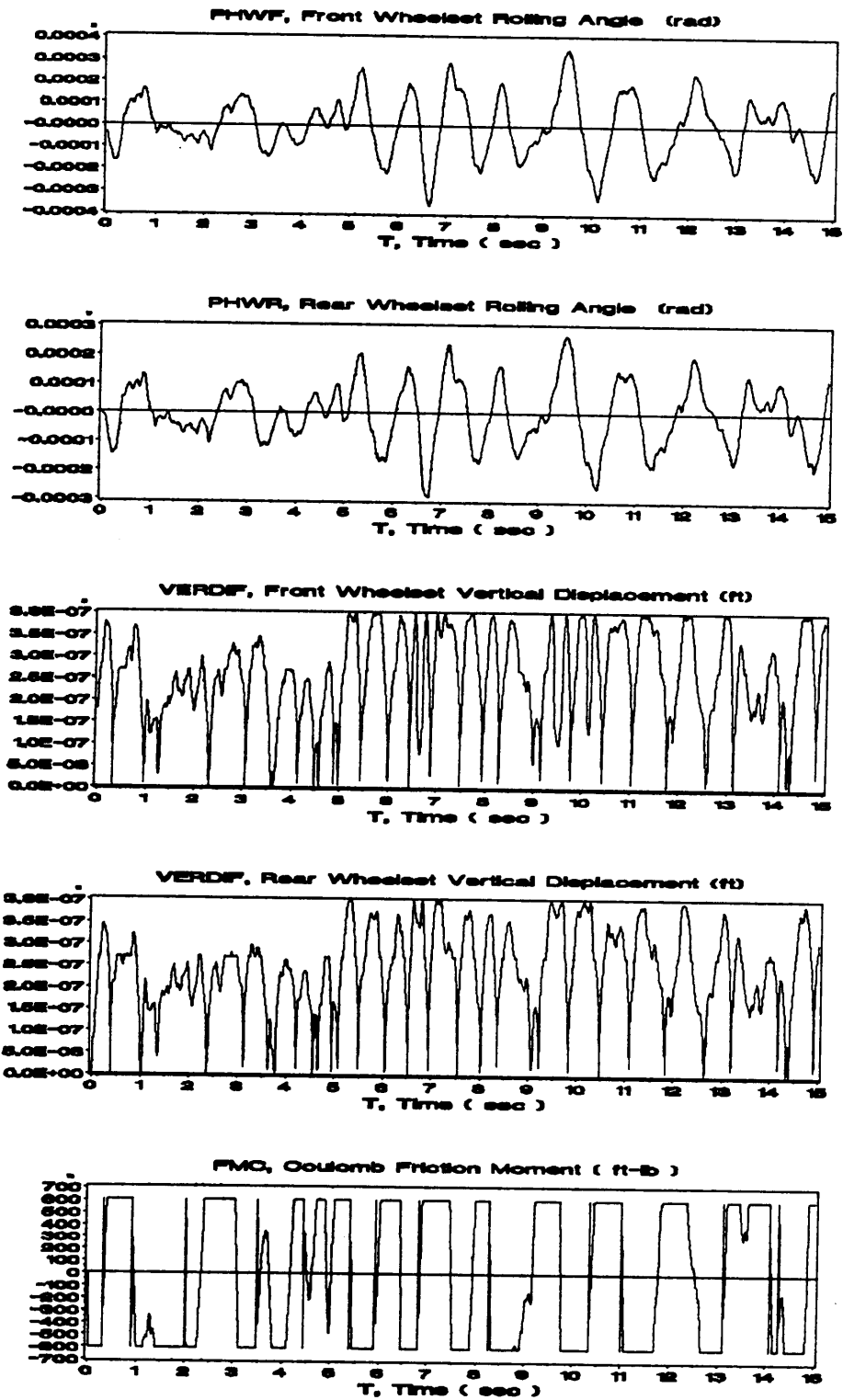


Figure 27. Vertical displacement and roll angle of the wheelset (45 mph)

Previously, Fig. 8 shows that flange contact first occurs at about 0.29 in. Fig. 26 shows both the front and rear wheelset lateral displacements. Since the wheelset lateral displacement is not more than  $\pm 0.21$  in., no flange contact occurs in this case. In Fig. 27, the upper two figures are the wheelset roll angle responses. These quantities are the order of  $10^{-4}$  rad. The middle two figures of Fig. 27 are the vertical displacement response of the wheelset. These quantities are the order of  $10^{-7}$  ft. Both the rolling angle and vertical displacement of the wheelsets are relatively small, so their effect on dynamics response is negligible. The bottom figure of Fig. 27 is the Coulomb friction moment in the centerplate between the car body and bolster. The breakout friction moment is 606 (ft-lb) which is the moment required to cause relative motion between the carbody and the centerplate.

Another case for empty car running at the speed of 80 mph (117.3 fps) is shown on Fig. 28 and Fig. 29. Fig. 28 shows the truck lateral displacement exhibiting hunting. Hunting is a sustained limit cycle oscillation that occurs when the vehicle travels at speeds in excess of the hunting threshold speed. Fig. 29 shows the wheelset lateral displacement. Slight flange contact exists for several time intervals in this case, because the wheelset lateral displacement is more than 0.29 in.

### **Summary**

1. The wheelset is a basic dynamic component of all railway vehicles. The equations of motion of a wheelset are derived in Appendix A and summarized in this chapter. The lateral and yaw equations are used to obtain the external force and moment which act on the wheelset.
2. A slider model simulates Coulomb friction moment at the centerplate in the half-car model.

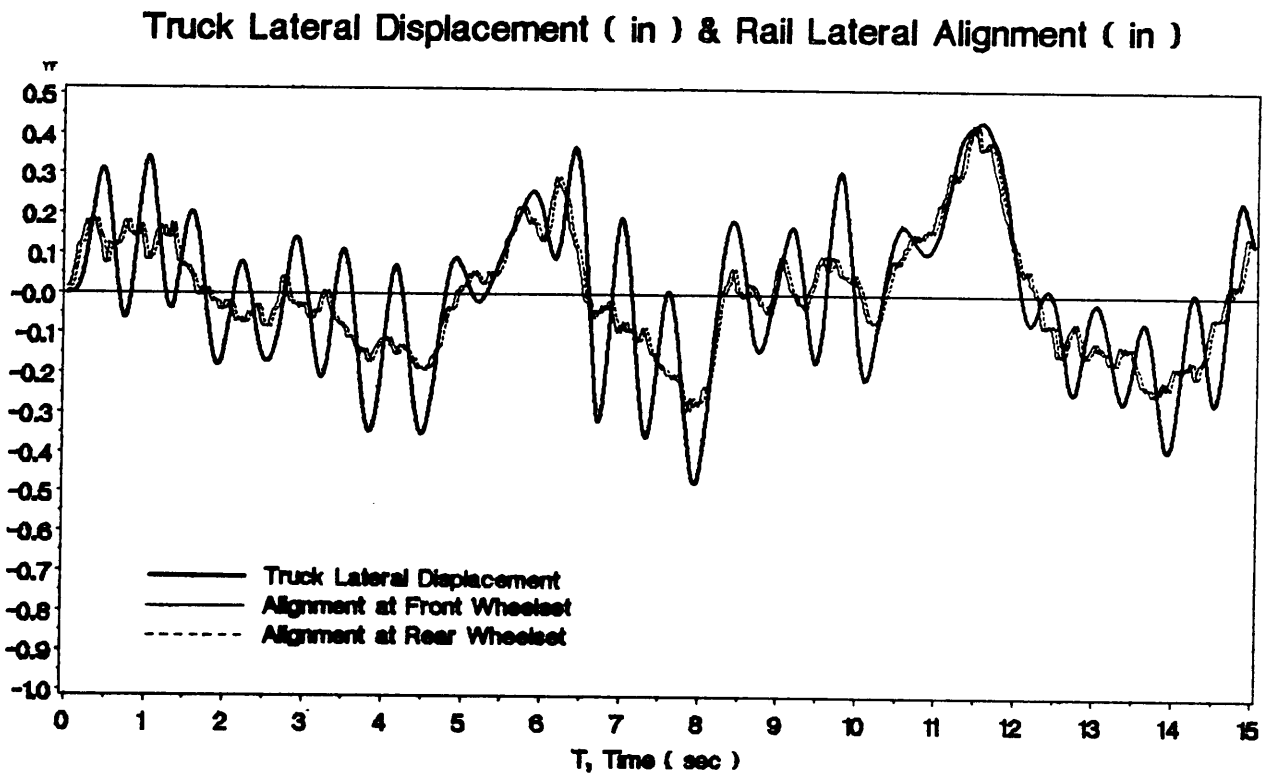


**Figure 28. Truck lateral displacement and rail lateral alignment (80 mph)**

### Front/Rear Wheelset Lateral Displacement ( in )

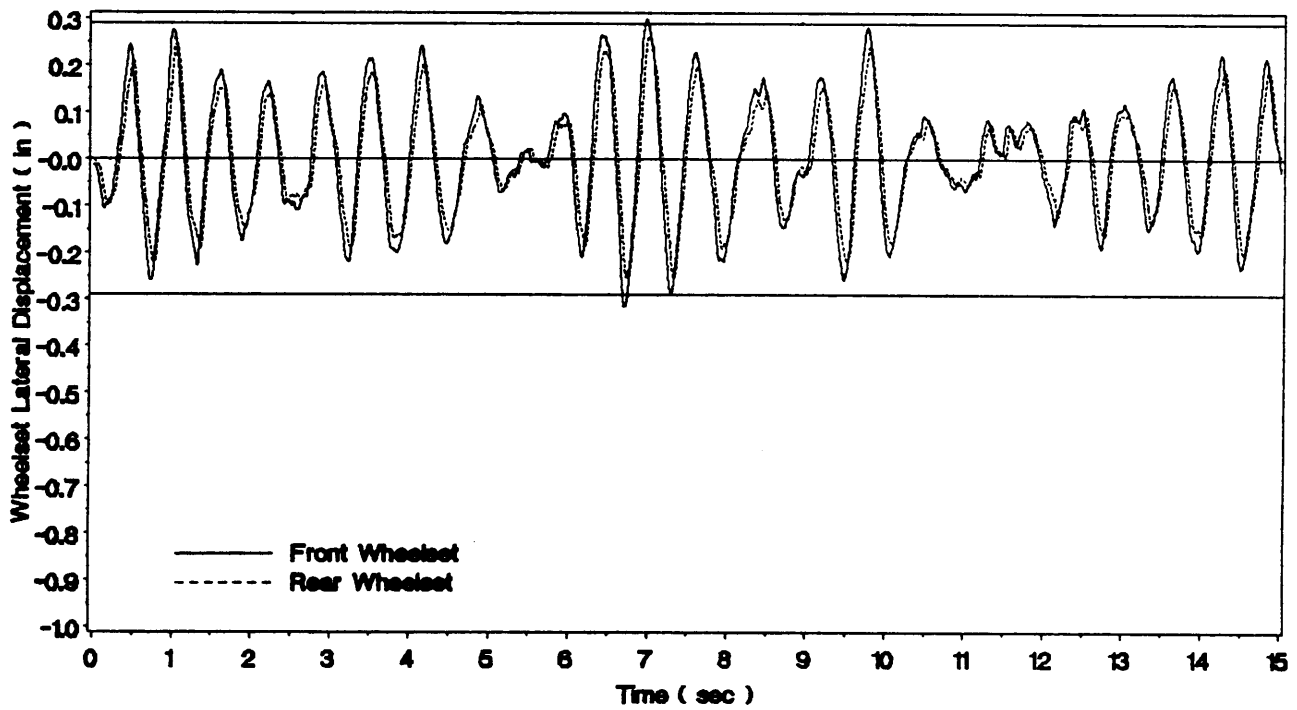


Figure 29. Front and rear wheelset lateral displacements (80 mph)

3. Random rail irregularities provide the input to the model, but only the lateral alignment is considered in the simulation because the lateral response is of importance in the wear problem.
4. The Runge-Kutta method is applied to solve the simultaneously differential equations of the system.
5. Two cases of dynamic response of the 5-degree-of-freedom half-car model show normal operation and hunting which occurs at high train speed.

# **Chapter 4 : Wear Prediction in Wheel/Rail Rolling Contact**

The wear mechanism found in wheel/rail rolling contact is complex, including adhesion wear, abrasive wear, surface fatigue wear, cracks and plastic deformation. The purpose of this chapter is not to distinguish the wear mechanism but to develop an algorithm to predict wheel wear profile by using the contact patch work wear model.

The basic assumption of the contact patch work model is that the wear is proportional to the energy dissipation or work done in the contact patch. Recently, the idea of the contact patch work model have been widely accepted in predicting the wear of wheel/rail rolling contact because it agrees well with experimental results.

This chapter discusses both Archard's model and the contact patch work model. The application of the contact patch work wear model to wheel/rail rolling contact is introduced to simulate the wheel wear and to obtain wheel wear profile and its wear rate. The relationship between the contact patch work model for wheel/rail rolling contact and Archard's model for the sliding contact is derived. The wear index coefficient for the contact patch work model and the wear coefficient for Archard's model are related to each other.

## 4.1 Wear Models

### *Archard's Model*

Archard's model, developed by Archard (1953), states that wear volume is directly proportional to normal force and sliding distance, but inversely proportional to the hardness of material. The expression is

$$Q \propto \frac{ND}{H} \quad (4.1)$$

where

- $Q$  = wear volume (in<sup>3</sup>)
- $N$  = normal load (lb)
- $D$  = sliding distance (in)
- $H$  = hardness ( $\frac{\text{lb}}{\text{in}^2}$ )

Furthermore, Archard defined the wear coefficient,  $K$ , in the following equation.

$$Q = \frac{K}{3} \frac{ND}{H} \quad (4.2)$$

### *Contact Patch Work Model*

Rail vehicle wheels typically operate with both rolling contact and slip. Many researchers have attempted to formulate the wear models to describe the wheel/rail wear due to rolling contact with slip and spin. A general review of these works is discussed in chapter 1. The contact patch work model is used in this work to predict wheel wear. According to Kumar (1984),

"If two contacting surfaces, with a normal load, experience creepage/slip under the influence of an external tangential force, the work done by this force is proportional to the volume of wear of the materials produced in the wear process, when the work used by other processes in the contact is small."

That is

(wear volume at the contact patch)  $\propto$  (work done at the contact patch)

$$Q \propto W_{done} \quad (4.3)$$

where

$Q$  = total wear volume over a time period

$W_{done}$  = total work done over a time period

## 4.2 Application of Contact Patch Work Model to Wheel/Rail Rolling

### Contact

When slip exists at the contact patch between the wheel and rail, there is energy dissipated in the contact patch. This dissipative energy is equivalent to the work done in the contact patch, which is the dot product of the creep force vector and slip vector.

#### *Computation of Work Done in the Contact Patch*

The location of the contact patch is a function of time. The work done in the contact patch during time interval  $t_x$  is

$$(W_{done})_k = \vec{F}_k \cdot \vec{D}_k + \vec{M}_k \cdot \vec{\psi}_k \quad (4.4)$$

where

- $(W_{done})_k$  = work done during time interval  $t_k$   
 $\vec{F}_k$  = creep force during time interval  $t_k$   
 $\vec{M}_k$  = creep moment during time interval  $t_k$   
 $\vec{D}_k$  = slip during time interval  $t_k$   
 $\vec{\psi}_k$  = spin during time interval  $t_k$

So the work done over a time period, T, is

$$W_{done} = \sum_{k=1}^{N_t} \{ \vec{F}_k \cdot \vec{D}_k + \vec{M}_k \cdot \vec{\psi}_k \} \quad (4.5)$$

and

$$T = N_t \Delta t \quad (4.6)$$

where

- $N_t$  = number of time steps  
 $\Delta t$  = time interval

The contact patch work can be computed in two ways. The global point of view considers the wheel as a rigid body. From this point of view, the work done in contact patch is the dot product of the creep force vector and the creepage vector multiplied by the contact patch velocity and time interval under consideration. Alternatively, the contact patch work can be computed by integrating all of the local work done over the entire contact patch. This second method accounts for the distribution of work done in the contact patch.

### Global work determination

From eq. (4.4) and (4.5), the global work done at the contact patch can be expressed as

$$(W_{done})_k = \{(F_X)_k(\xi_X)_k + (F_Y)_k(\xi_Y)_k + (M_Z)_k(\xi_{SP})_k\}V\Delta t \quad (4.7)$$

$$W_{done} |_{global} = \sum_{k=1}^{N_t} (W_{done})_k = V\Delta t \sum_{k=1}^{N_t} \{(F_X)_k(\xi_X)_k + (F_Y)_k(\xi_Y)_k + (M_Z)_k(\xi_{SP})_k\} \quad (4.8)$$

where

- $W_{done} |_{global}$  = global work done over a time period,  $T$
- $(W_{done})_k$  = global work done during time interval  $t_k$
- $(..)_k$  = some quantity during time interval  $t_k$

### Local work determination

The creep force and moment and the slip and spin creepage at each subarea in contact patch are known (see Chapter 2), so the work done at each subarea in contact patch can be computed and summed. The work expression is

$$(W_{done,ij})_k = V\Delta t \left\{ (F_{X,ij})_k \left( \frac{W_X}{V} |_{ij} \right)_k + (F_{Y,ij})_k \left( \frac{W_Y}{V} |_{ij} \right)_k + (M_{Z,ij})_k \left( \frac{\Omega}{V} |_{ij} \right)_k \right\} \quad (4.9)$$

where

- $(W_{done,ij})_k$  = work done at subarea  $(x_i, y_j)$  in contact patch during time interval  $t_k$
- $\left( \frac{W_X}{V} |_{ij} \right)_k$  = normalized longitudinal slip at subarea  $(x_i, y_j)$  in contact patch during time interval  $t_k$
- $\left( \frac{W_Y}{V} |_{ij} \right)_k$  = normalized lateral slip at subarea  $(x_i, y_j)$  in contact patch during time interval  $t_k$
- $\left( \frac{\Omega}{V} |_{ij} \right)_k$  = normalized spin  $\left( \frac{1}{R} \right)$  at subarea  $(x_i, y_j)$  in contact patch during time

- interval  $t_k$
- $(F_{x_{ij}})_k$  = longitudinal creep force at subarea  $(x_i, y_j)$  in contact patch during time interval  $t_k$
- $(F_{y_{ij}})_k$  = lateral creep force at subarea  $(x_i, y_j)$  in contact patch during time interval  $t_k$
- $(M_{z_{ij}})_k$  = creep moment at subarea  $(x_i, y_j)$  in contact patch during time interval  $t_k$

$$W_{done | local} = \sum_{k=1}^{N_t} \sum_{i=1}^{N_x} \sum_{j=1}^{N_y} \{(W_{done_{ij}})_k\} \quad (4.10)$$

where

$N_x$  = number of the subdivision of the contact patch along X-direction

$N_y$  = number of the subdivision of the contact patch along Y-direction

Two cases of the distribution of contact patch work are presented in Fig. 17 and Fig. 18.

### Comparison of Global and Local Work Done

Theoretically,

$$W_{done | global} = W_{done | local} \quad (4.11)$$

Actually, because of the contact patch discretization, a discrepancy exists between the global and local work quantities. Although the difference is unavoidable, the distribution of the work done in the contact patch appear to be reliable. By taking the global quantity to be correct, the previous equation can be revised to account for the difference between the global and the local quantities. The local work is multiplied by a factor,  $\hat{K}$ , which is determined from the ratio of the global and local works as shown below.

$$W_{done | global} = \hat{K} W_{done | local} \quad (4.12)$$

where

$$\hat{K} = \text{some constant}$$

### **Computation of Wear Volume**

Since the work done in the contact patch is found, the contact patch work model can be applied to calculate the wear volume in the contact patch. Similarly, there are two views to compute wear volume, global and local point of views.

#### **Global wear volume determination**

Recalling the contact patch work model eq. (4.3).

$$Q |_{global} \propto W_{done} |_{global} \quad (4.13)$$

Substituting  $W_{done} |_{global}$  eq. (4.7) into above equation,

$$Q |_{global} \propto V \Delta t \sum_{k=1}^{N_t} \{ (F_X)_k (\xi_X)_k + (F_Y)_k (\xi_Y)_k + (M_Z)_k (\xi_{SP})_k \} \quad (4.14)$$

#### **Local wear volume determination**

By applying the contact patch work model, eq. (4.3) can be rewritten

$$(Q_{ij})_k \propto (W_{done,ij})_k \quad (4.15)$$

and sum of the local wear volume can be found

$$Q |_{local} = \sum_{k=1}^{N_t} \sum_{i=1}^{N_x} \sum_{j=1}^{N_y} (Q_{ij})_k \propto \sum_{k=1}^{N_t} \sum_{i=1}^{N_x} \sum_{j=1}^{N_y} (W_{done_{ij}})_k \quad (4.16)$$

in which  $(W_{done_{ij}})_k$  is defined in eq (4.9).

### Comparison of Global and Local Wear Volume

From the comparison of global and local work done, similarly, the relationship for the global and local wear volume is also obtained

$$Q |_{global} = \hat{K} Q |_{local} \quad (4.17)$$

### *Application to Wheel/Rail Rolling Contact Problem*

The work done and the wear volume in contact patch is derived previously, then the same idea is to be applied to wheel/rail rolling contact problem. Fig. 30 shows the illustration of the contact patch location in the wheel/rail contact and the scheme of subscripts adopted in the following derivation.

#### Computation of Work Done along Wheel Profile

For the purpose of obtaining the distribution of wear volume along wheel profile, the local work done and only a single strip of work done along X-direction in the contact patch during time interval  $t_k$  are considered.

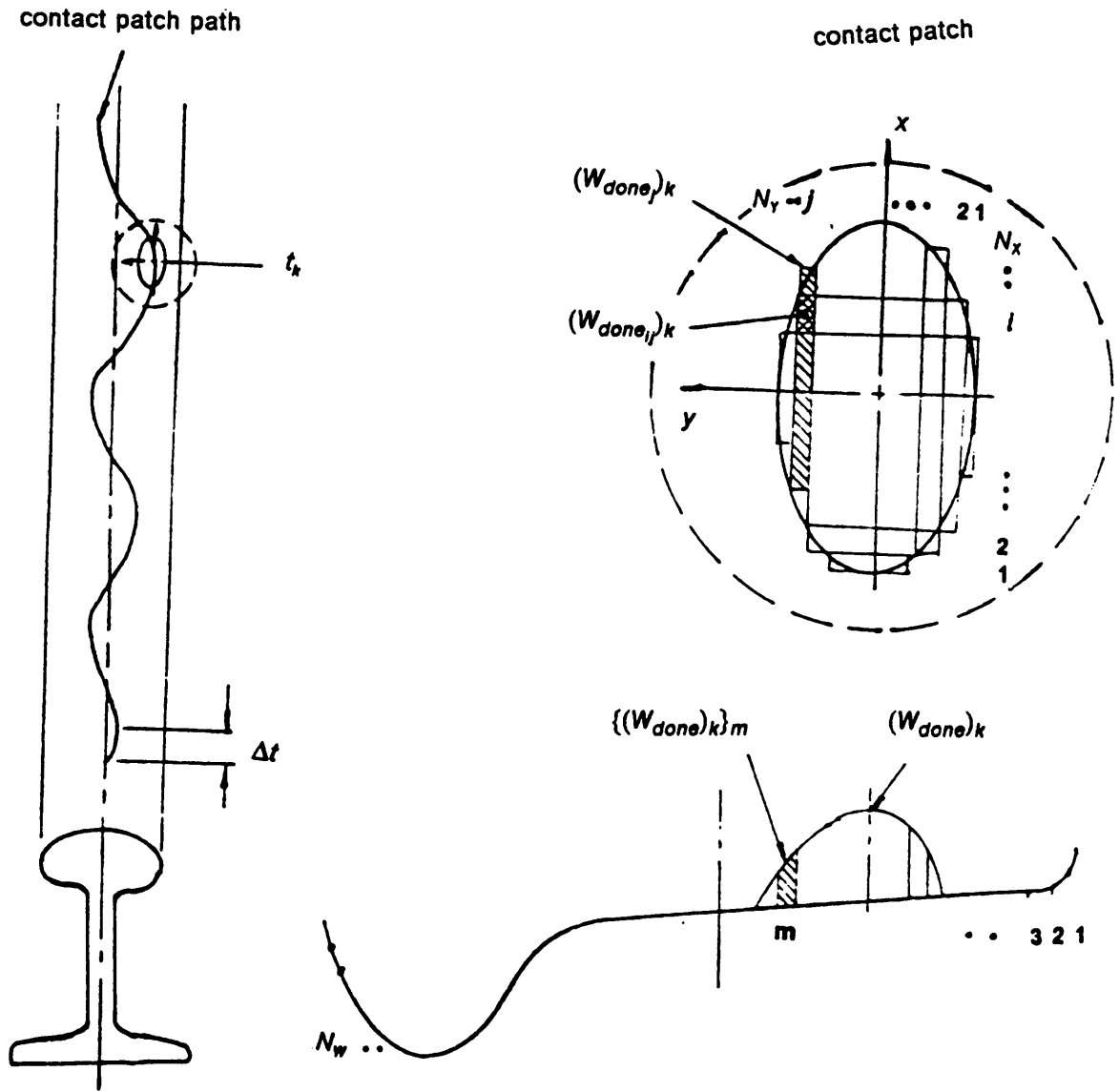


Figure 30. Illustration of the subscript of contact patch for wheel/rail contact

$$(W_{done})_k = \hat{K} \sum_{l=1}^{N_x} (W_{done,l})_k \quad (4.18)$$

where

$(W_{done})_k$  = sum of work done at a strip of the contact patch along X-direction for  $y_l$  during time interval  $t_k$ , ( $y_l$  is the contact patch coordinate)

Furthermore,  $(W_{done})_k$  can be expressed in the wheel coordinate,  $y_m$

$$\{(W_{done})_k\}_m = (W_{done})_k \quad (4.19)$$

where

$\{(W_{done})_k\}_m$  = work done at  $y_m$  along wheel profile during time interval  $t_k$   
 $y_m$  = lateral position expressed in the wheel coordinate

The distribution of the work done along wheel profile over a period of time,  $T$ , is

$$(W_{done})_m = \sum_{k=1}^{N_t} \{(W_{done})_k\}_m \quad (4.20)$$

and the total work done over a period of time,  $T$ , is

$$W_{done} = \sum_{m=1}^{N_w} (W_{done})_m = \sum_{m=1}^{N_w} \sum_{k=1}^{N_t} \{(W_{done})_k\}_m \quad (4.21)$$

where

$W_{done}$  = total work done of the wheel over a period of time  $T$   
 $(W_{done})_m$  = distribution of work done along the wheel profile over a period of time  $T$   
 $N_w$  = number of subdivision of the wheel profile

### Computation of Wear Volume along the Wheel Profile

By applying contact patch work model, the wear volume along the wheel profile can be expressed as

$$(Q)_m = K_W^*(W_{done})_m \quad (4.22)$$

where

$$\begin{aligned} (Q)_m &= \text{wear volume at } y_m \text{ along the wheel profile over a period of time } T \\ K_W^* &= \text{some constant} \end{aligned}$$

By substitution of eq. (4.9), (4.18), (4.19) and (4.20), the total wear volume of the wheel over a period of time,  $T$ , becomes

$$Q = K_W V \Delta t \sum_{k=1}^{N_t} \sum_{m=1}^{N_w} \sum_{l=1}^{N_x} \sum_{j=1}^{N_y} \left\{ (F_{X_{ij}})_k \left( \frac{W_X}{V} |_{ij} \right)_k + (F_{Y_{ij}})_k \left( \frac{W_Y}{V} |_{ij} \right)_k + (M_{Z_{ij}})_k \left( \frac{\Omega}{V} |_{ij} \right)_k \right\}_m \quad (4.23)$$

where

$$K_W = \text{wear index coefficient } (K_W = \hat{K} K_W^*)$$

Also, the total wear volume of the wheel over a period of time,  $T$ , can be expressed in global form

$$Q = K_W V \Delta t \sum_{k=1}^{N_t} \left\{ (F_X)_k (\xi_X)_k + (F_Y)_k (\xi_Y)_k + (M_Z)_k (\xi_{SP})_k \right\} \quad (4.24)$$

The wear index coefficient will be discussed more detail later. Note that eq. (4.23) and (4.24) have the same wear volume.

### 4.3 Expression of Wear Rate

Wear rate is an important physical property. In sliding contact, wear rate is usually expressed by the removed wear volume per unit sliding distance from Archard's model. Because of the complexity of wear phenomena, wear rate is not a simple function. Wear is a function of many variables. Wear rate can be expressed in three forms,

$$\dot{Q} = \frac{\text{wear volume}}{\text{time period}} = \frac{Q}{T} \quad (4.25)$$

$$\hat{Q} = \frac{\text{wear volume}}{\text{sliding distance}} = \frac{Q}{D} \quad (4.26)$$

$$\bar{Q} = \frac{\text{wear volume}}{\text{running distance}} = \frac{Q}{VT} \quad (4.27)$$

The total sliding distance,  $D$ , can be defined as the sum of the sliding distance during each time interval  $t_k$  which is the product of the sliding velocity and the time step. The slip velocity and sliding distance are as follows:

$$\dot{D}_k = \sqrt{(\xi_x)_k^2 + (\xi_y)_k^2} V \quad (4.28)$$

$$D_k = \dot{D}_k(\Delta t) \quad (4.29)$$

$$D = \sum_{k=1}^{N_t} D_k = \sum_{k=1}^{N_t} \dot{D}_k \Delta t = \sum_{k=1}^{N_t} \sqrt{(\xi_x)_k^2 + (\xi_y)_k^2} V \Delta t \quad (4.30)$$

where

$\dot{D}_k$  = sliding velocity during time interval  $t_k$

$D_k$  = sliding distance during time interval  $t_k$

$D$  = total sliding distance over a time period( $T$ )

By substituting eq. (4.24), the three forms of wear rate become

$$\dot{Q} = \frac{Q}{T} = \frac{Q}{N_t \Delta t} = K_W \frac{V}{N_t} \sum_{k=1}^{N_t} \{(F_X)_k(\xi_X)_k + (F_Y)_k(\xi_Y)_k + (M_Z)_k(\xi_{SP})_k\} \quad (4.31)$$

$$\hat{Q} = \frac{Q}{D} = \frac{K_W}{\sum_{k=1}^{N_t} \sqrt{(\xi_X)_k^2 + (\xi_Y)_k^2}} \sum_{k=1}^{N_t} \{(F_X)_k(\xi_X)_k + (F_Y)_k(\xi_Y)_k + (M_Z)_k(\xi_{SP})_k\} \quad (4.32)$$

$$\bar{Q} = \frac{Q}{VT} = \frac{Q}{V(N_t \Delta t)} = \frac{K_W}{N_t} \sum_{k=1}^{N_t} \{(F_X)_k(\xi_X)_k + (F_Y)_k(\xi_Y)_k + (M_Z)_k(\xi_{SP})_k\} \quad (4.33)$$

#### 4.4 Relation Between Archard's Model and Contact Patch Work Model

From eq. (4.2), Archard's model can be expressed

$$Q = \frac{K}{3} \frac{ND}{H} \quad (4.34)$$

where  $K$  is the wear coefficient which is commonly defined based upon Archard's relationship. The wear coefficient can be found in Rabinowicz's report (1980) for different materials sliding under specific conditions, and it is an important physical interpretation of wear behavior. Fig. 31 shows the common range of wear coefficients for typical wear mechanisms.

The relationship between the wear index coefficient and the wear coefficient is interesting. The wear coefficient is to Archard's model for sliding contact, as the wear index coefficient is

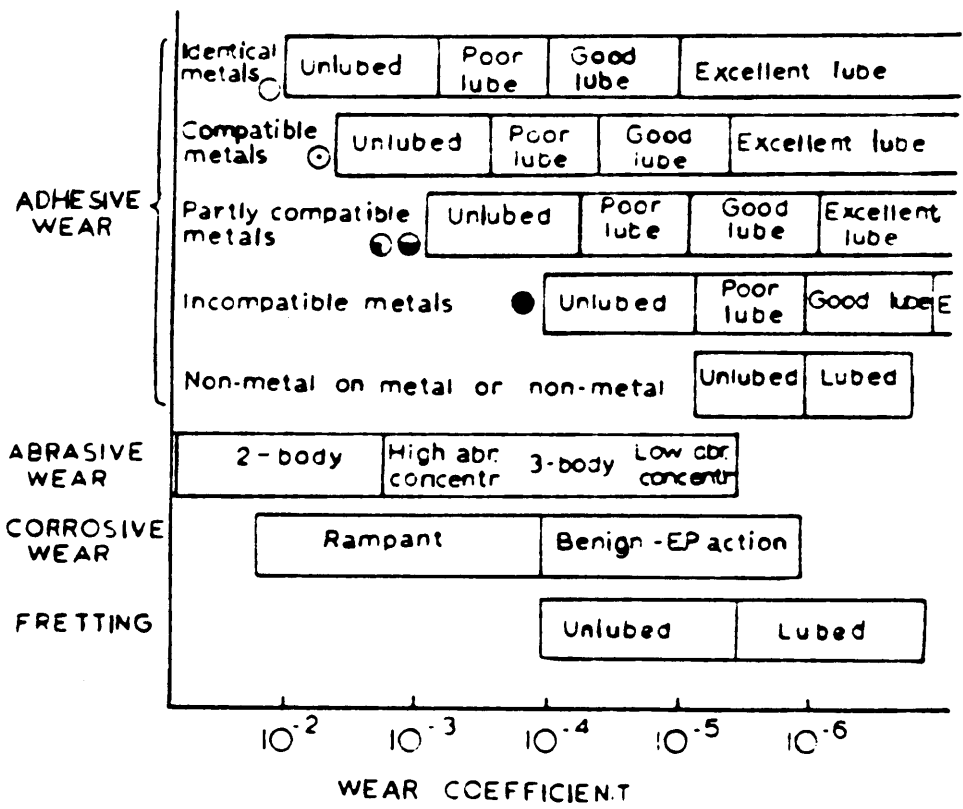


Figure 31. Range of wear coefficient for typical wear mechanisms (Rabinowicz, 1980)

to the contact patch work model for the rolling contact with slip/spin. Recalling the Coulomb friction law,

$$P = \frac{F}{\mu} \quad (4.35)$$

where

$$\begin{aligned} F &= \text{friction force} \\ \mu &= \text{friction coefficient} \\ N &= \text{normal load} \end{aligned}$$

In rolling contact with slip,  $F$  can be considered as the creep force and substituted into eq. (4.2),

$$Q = \frac{K}{3H\mu} FD \quad (4.36)$$

The wear rate expressed in wear volume per unit sliding distance is

$$\hat{Q} = \frac{Q}{D} = \frac{K}{3H\mu} \frac{FD}{D} \quad (4.37)$$

and is multiplied by  $V\Delta t$  in the denominator and nominator respectively,

$$\hat{Q} = \frac{K}{3H\mu} \frac{V\Delta t}{D} F \frac{D}{V} \quad (4.38)$$

By rearranging the above equation and substituting the definition of creepage, eq. (4.38) becomes

$$\hat{Q} = \frac{K}{3H\mu} \frac{V\Delta t}{D} (F \xi) \quad (4.39)$$

Based upon the contact patch work model, the wear rate expressed in wear volume per sliding distance is obtained in eq. (4.32) and rewritten

$$\hat{Q} = \frac{Q}{D} = \frac{1}{D} K_W V \Delta t \sum_{k=1}^{N_t} \{ (F_X)_k (\xi_X)_k + (F_Y)_k (\xi_Y)_k + (M_Z)_k (\xi_{SP})_k \} \quad (4.40)$$

By comparison of eq. (4.39) based on Archard's model for sliding contact and eq. (4.40) based on the contact patch work model for rolling contact with slip, the wear index coefficient is

$$K_W = \frac{K}{3H\mu} \quad (4.41)$$

The above equation is the relationship between the wear index coefficient of the contact patch work model for rolling contact and the wear coefficient defined in Archard's model for sliding contact. It may be stated that the wear index coefficient is equal to the wear coefficient divided by three times the product of the hardness and the friction coefficient of materials.

An example of calculation of wear coefficient is presented. McEwen and Harvey (1985) carried out a series of field wear tests for class D wheels running on BS11 rails. Friction coefficient was assumed to be in the range of 0.45-0.55. In their report, Fig. 10 shows the wear index coefficient is  $1.2 \times 10^{-9} \frac{\text{in}^2}{\text{lb}}$ . In general, hardness of wheel and rail are about 200 kpsi. Therefore, the wear coefficient is computed

$$\begin{aligned} K &= 3K_W \mu H \\ &= 3(1.2 \times 10^{-9} \frac{\text{in}^2}{\text{lb}})(0.5)(200,000 \text{ psi}) \\ &= 3.6 \times 10^{-4} \end{aligned}$$

Fig. 32 is a collection of the wear index coefficients. The wear coefficients are of the order of  $10^{-9}$  and the calculated wear coefficients are of the order of  $10^{-4}$ .

Kumar et al. (1985) used the following wear equation to calculate wear coefficient.

McEwen and Harvey (1985)

$\mu = 0.45 - 0.55$	$K_w \left(\frac{\text{in}^2}{\text{lb}}\right)$	$K$
rail tread (Fig. 7)	$1.18 \times 10^{-9}$	$3.54 \times 10^{-4}$
rail flange (Fig. 10)	$2.14 \times 10^{-9}$	$6.42 \times 10^{-4}$
wheel tread (Fig. 7)	$0.78 \times 10^{-9}$	$4.18 \times 10^{-4}$

Kumar et al. (1985), Table. 2, (no sand)

rail	$K_w \left(\frac{\text{in}^2}{\text{lb}}\right)$	$K$
$\mu = 0.24$	$2.14 \times 10^{-9}$	$1.0 \times 10^{-4}$
$\mu = 0.35$	$4.84 \times 10^{-9}$	$3.36 \times 10^{-4}$
$\mu = 0.5$	$1.53 \times 10^{-9}$	$1.49 \times 10^{-4}$

wheel	$K_w \left(\frac{\text{in}^2}{\text{lb}}\right)$	$K$
$\mu = 0.24$	$2.18 \times 10^{-9}$	$1.1 \times 10^{-4}$
$\mu = 0.35$	$6.30 \times 10^{-9}$	$4.63 \times 10^{-4}$
$\mu = 0.5$	$1.8 \times 10^{-9}$	$1.89 \times 10^{-4}$

**Figure 32. A collection of wear index coefficient and wear coefficient**

$$Q = K \frac{ND}{3\sigma_{yp}}$$

where

$\sigma_{yp}$  = yielding stress

They estimated normal force and sliding distance. According to their experiments,  $\sigma_{yp} = 70$  kpsi for the wheel and  $\sigma_{yp} = 65$  kpsi for the rail. In order to obtain the wear index coefficient, the following is calculated

$$K_W = \frac{K}{3\mu\sigma_{yp}}$$

The numerical result is shown in Fig. 32. It can be noted that the wear index coefficients have the order of  $10^{-9}$ , and that the wear coefficients have the order of  $10^{-4}$ . Both Kumar et al. (1985) and McEwen and Harvey (1985) present the same order of wear index coefficient and wear coefficient. According to Fig. 31, these wear coefficients are for identical metal in poor lubricated adhesive wear. In fact, the experiments were carried out on dry clean surface. This conflict may be the cause of rolling contact different from sliding contact and the existence of variant wear mechanism.

### **Summary**

1. Archard's model for sliding contact and contact patch work model for rolling contact with slip are introduced.
2. The algorithm of the contact patch work model including both the local and global view is applied to wheel/rail rolling contact.

3. Three forms of the wear rate expressed in wear volume per unit running time, per unit sliding distance and per unit running distance are presented. However, the wear volume per unit running distance is usually used to represent the wear rate in rail vehicles.
4. The wear index coefficient defined in eq (4.23) is related to the wear coefficient defined in Archard's model eq. (4.2).

$$K_W = \frac{K}{3H\mu}$$

5. Wear index coefficients found in the rail vehicle literature equates to wear coefficients in the order of  $10^{-4}$ .

## **Chapter 5 : Wear Computation Method and Results**

Chapter 2 describes the wheel/rail contact mechanics to calculate the contact area, creep forces and moment, and creepages. Chapter 3 presents a 5-degree-of-freedom half-car model to simulate the truck lateral motion. Chapter 4 discusses the contact patch work wear model which is applied to the wheel/rail rolling contact problem. This chapter shows the simulation of the wheel wear process combining the previous discussions of the wheel/rail contact mechanics, the truck dynamic response and the contact patch work wear model.

The consecutive wear profiles of the four wheels in the truck are predicted for both tread contact and slight flange contact. Several cases of empty and fully loaded cars with AAR and Heumann wheels running at 45 mph and 60 mph are presented. These wear profiles agree well with experimental results (Marcotte et al., 1980) and a previous analytical approach (Davila, 1986).

## 5.1 Wear Computation method

Fig. 33 shows the flow chart of the simulation of wheel wear process. The simulation is performed by the program WWPPVW (Wang, 1988b) associated with the program WHRAILA (Heller and Cooperrider, 1977a) to calculate the wheel/rail geometric constraints, the program RALIN (Fries and Coffey, 1987) to generate random rail alignment, the program FASTSIM (Kalker, 1981) to compute the creep force and moment and the contact patch work, and the program DYNAMC (Wang, 1988b) to obtain the dynamic response of the half car model. The WWPPVW program accounts for the four-wheel wear processes instead of Davila's assumption (Davila, 1986) of all wheels having the same amount of wear.

Before the simulation, the wheel and rail profiles are digitized as the input data for WHRAILA. The vehicle specifications, see Fig. 21, and the initial conditions of the half car model and the program optional numbers (Wang, 1988b) are defined.

To begin the simulation of the wear process, the wheel/rail geometric constraints are calculated, then the contact position is computed from the dynamic response including the effect of the random rail alignment. Therefore, the geometric constraints, including rolling radii, contact angle and roll angle, can be interpolated at the contact position, and the creepages can be computed. Then the creep force and moment and the contact patch work can be determined.

In the work reported in this thesis actual values of wear index coefficient have not been used. Instead, a set of scale factors has been used in the wear profile computations. Future work should include the use of wear index coefficients.

If the wear volume is more than  $0.03 \text{ in}^3$ , the wear is distributed around the wheel. When the wheels are reprofiled, the wheel/rail geometric constraints need to be recalculated. Finally,

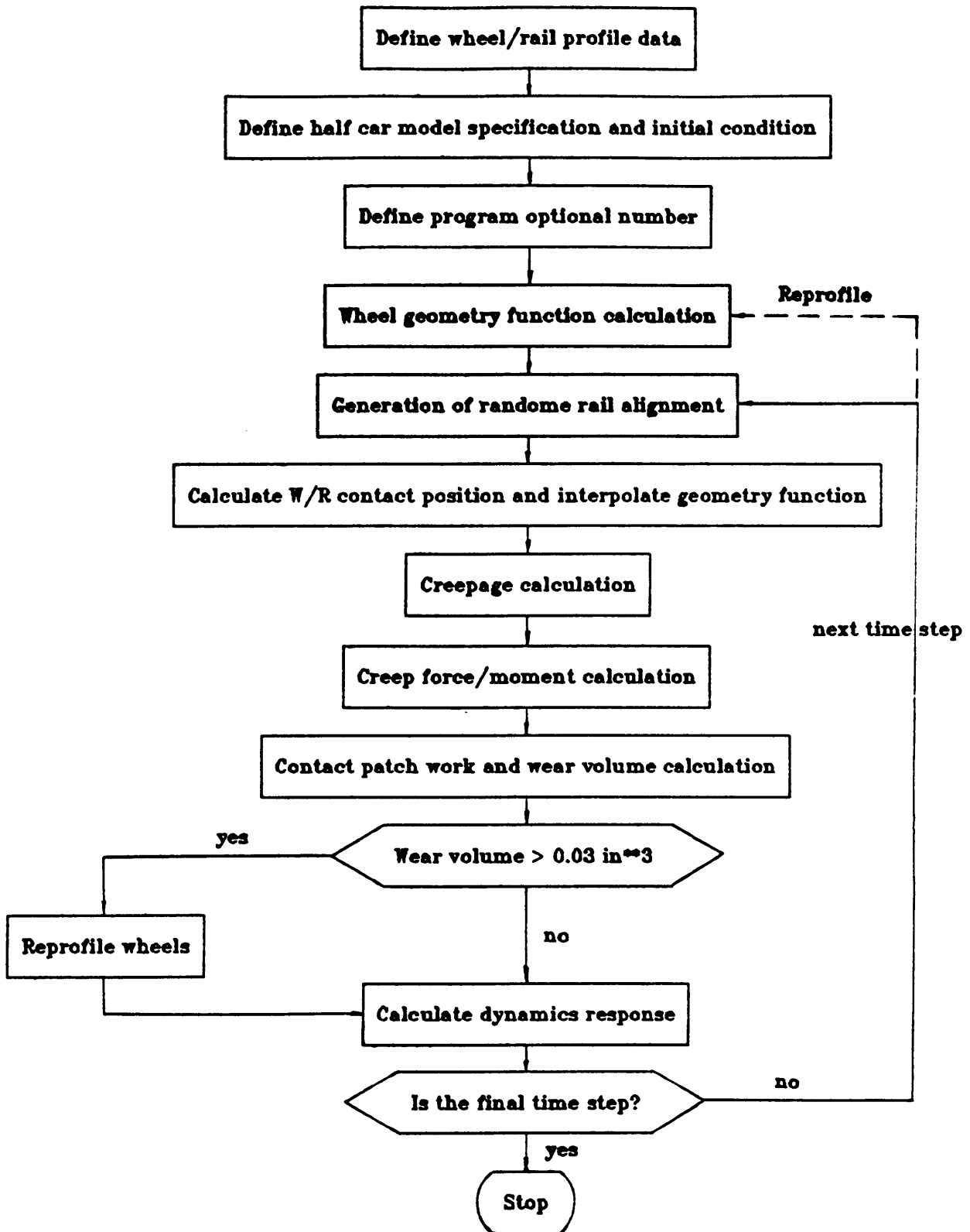


Figure 33. Flow chart of the simulation of wheel wear process

the dynamic response of the half car model is obtained. The simulation goes to the next time step and repeats the same procedure described above until the setup time is reached.

## 5.2 Wear in Tread Contact

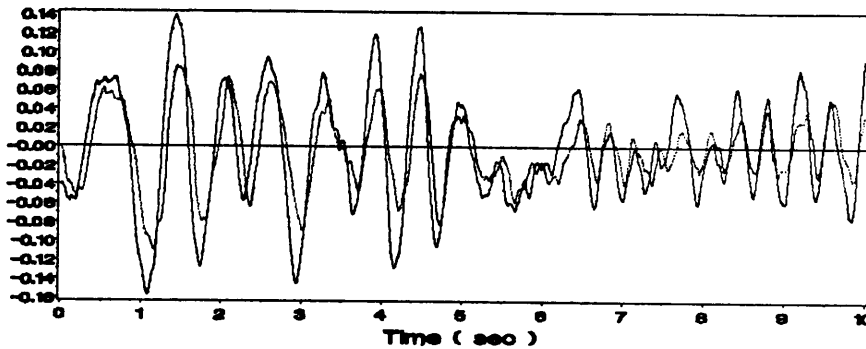
This section presents several cases of tread contact for the new AAR and Heumann wheels running on the new 132-RE rail. Both the AAR and Heumann wheel profiles introduced in Chapter 2 have a linear 1/20 taper over the tread. The main difference between these two wheels is that the Heumann profile has more curvature at the flange to provide a smoother transition between tread and flange contact.

Each case was simulated for 10 s using a time step of 0.001 s for an empty car and 0.0004 s for a fully loaded car by the simulation method discussed in section 5.1. The figures show the front and rear wheelset lateral positions, final wear profiles of the four wheels in the truck, and their consecutive wear profiles. From the time history of the wheelset lateral positions, the contact patch locations on wheel and rail can be computed.

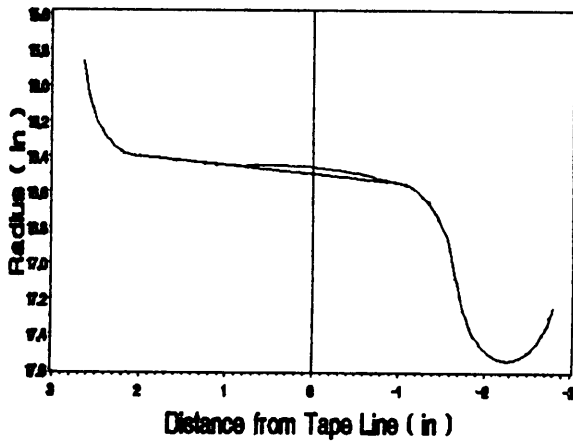
Fig. 34 to Fig. 36 show the case of an empty car with AAR wheels running at 45 mph. In Fig. 34 the front and rear wheelset lateral displacements are shown on the top, and the final wear profiles of the four wheels are presented in the remaining plots. The front wheelset has larger displacement than the rear wheelset, such that the contact patch positions range more widely over the front wheels than the rear ones.

Fig. 35 and Fig. 36 show the consecutive wear profiles for the front and rear wheels. The rear wheels have more wear than the front wheels. The front wheels have 103 profile changes, and the rear wheels have 125. These wear profiles are similar to Davila's prediction (see Fig. 37). He assumed that the distribution of wear volume is parabolic across the contact patch and that each wheel has the same amount of wear.

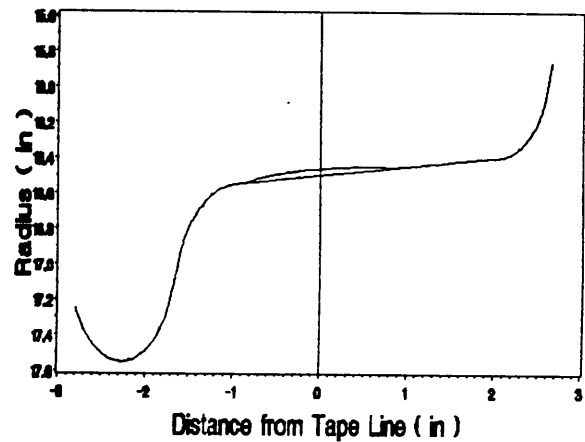
### Front/Rear Wheelset Lateral Displacement ( in )



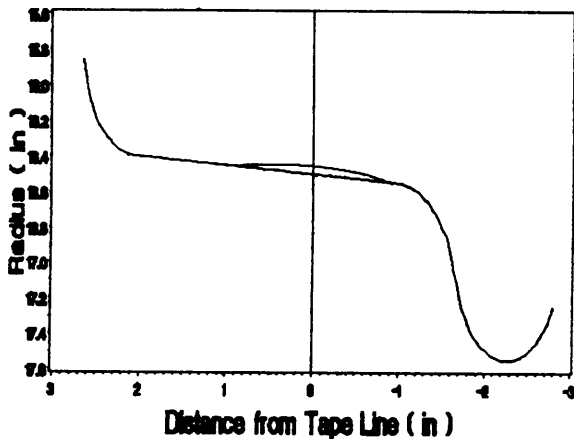
Left-Front Wheel Profile



Right-Front Wheel Profile



Left-Rear Wheel Profile



Right-Rear Wheel Profile

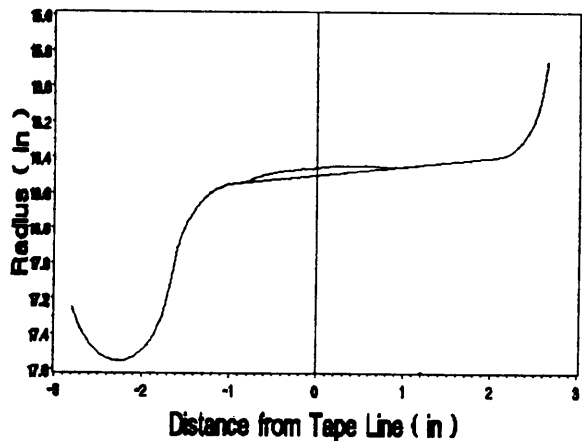
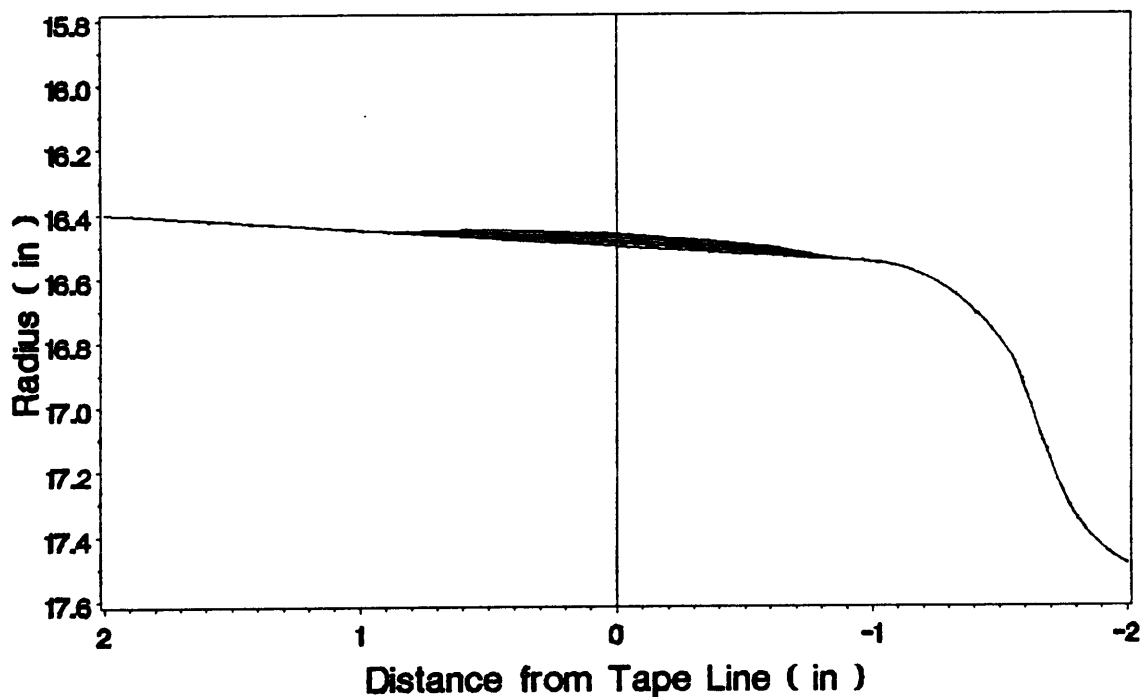


Figure 34. The lateral position of wheelsets and final wheel wear profiles (45,AAR,empty,T)

### Left-Front Wheel Profile



### Left-Rear Wheel Profile

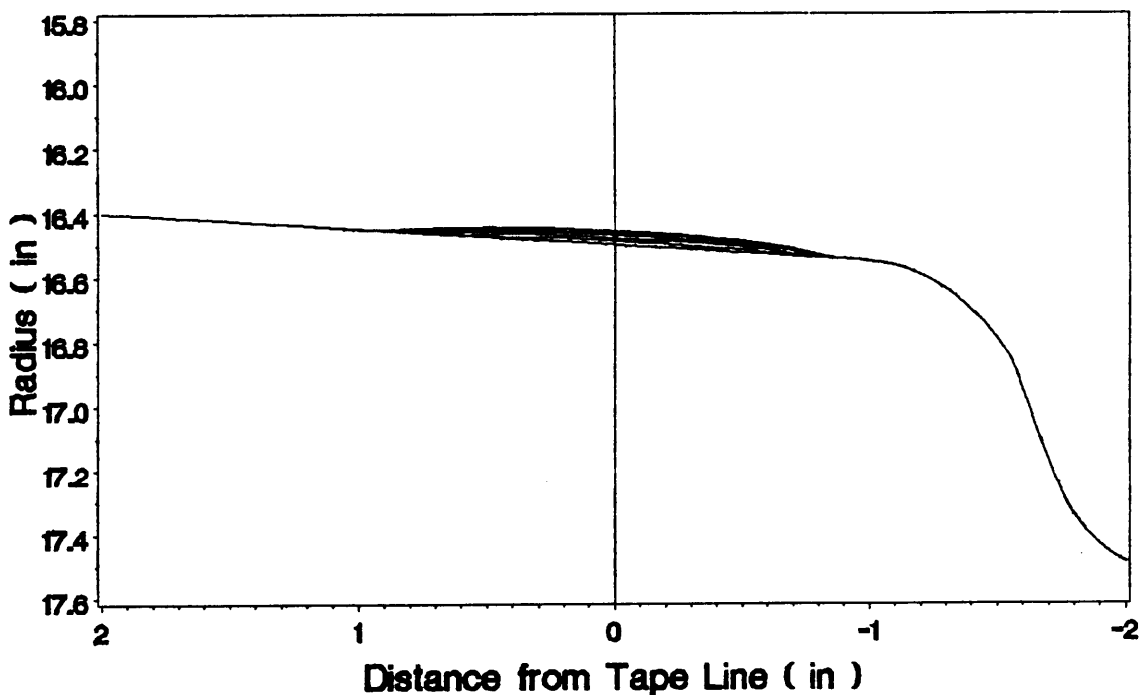
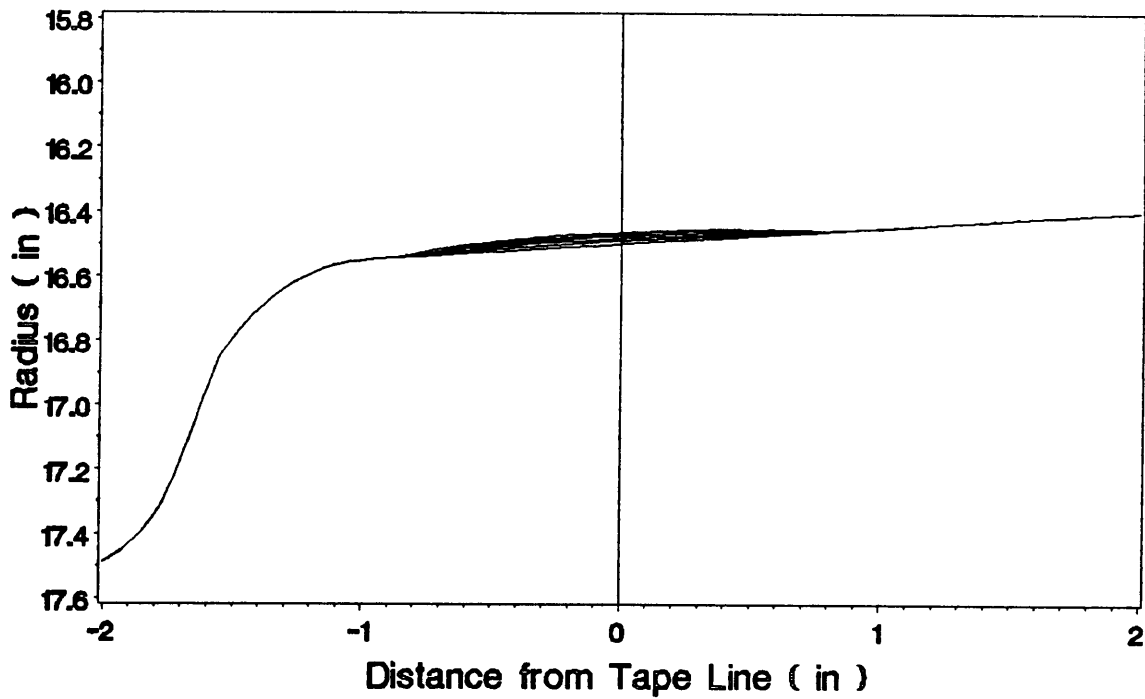


Figure 35. The consecutive wear profiles of the left wheels (45,AAR,empty,T)

### Right-Front Wheel Profile



### Right-Rear Wheel Profile

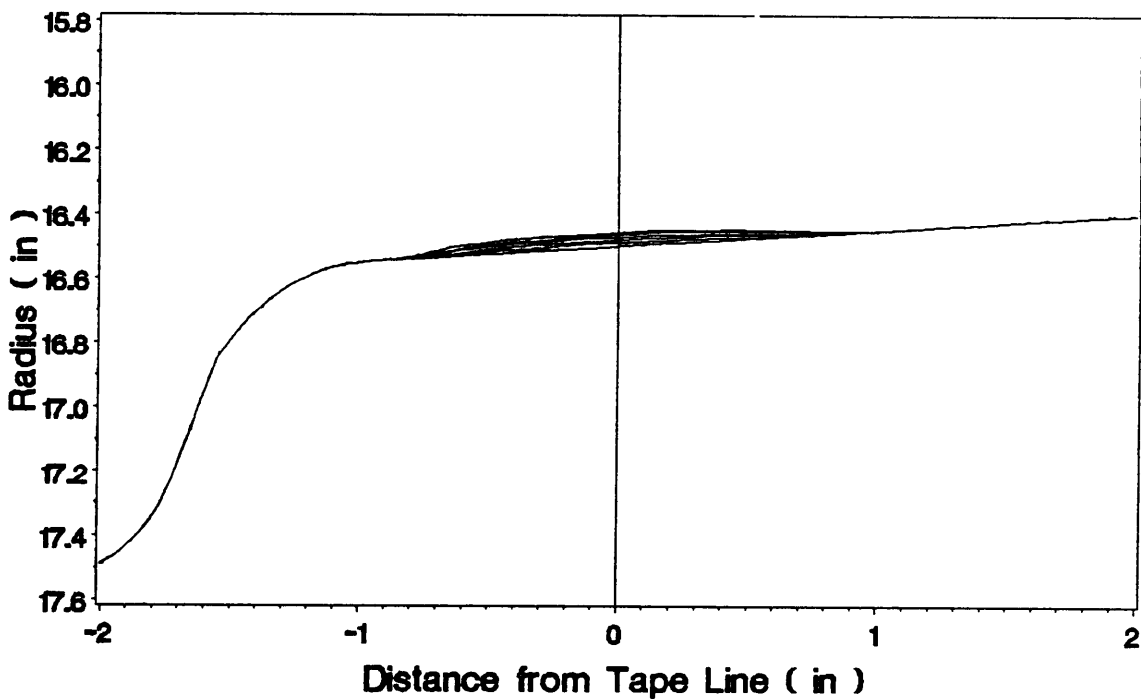


Figure 36. The consecutive wear profiles of the right wheels (45,AAR,empty,T)

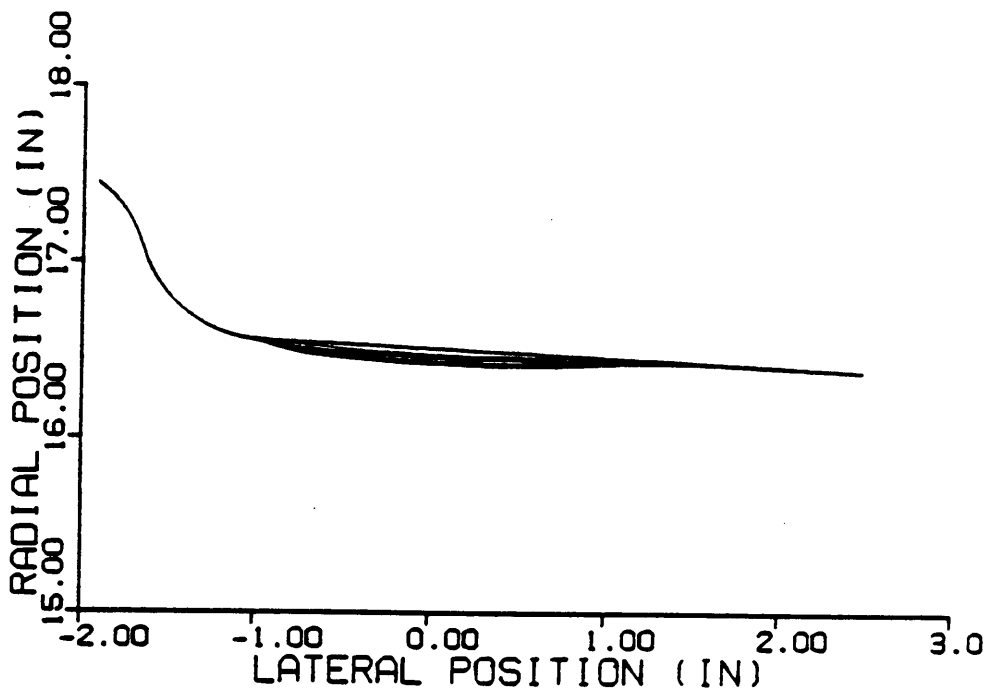


Figure 37. The consecutive wheel wear profiles of Davila's prediction (Davila, 1986)

The relative wear rates ( $\text{in}^3/\text{in}$ ), wear volume per unit running distance, are summarized and scaled in Fig. 38. For 45, AAR, empty, T, the wear rates of the rear wheels are larger than the wear rates of the front wheels. The front wheels have less wear rates than the rear wheels, although the contact patch ranges more widely over the front wheels than the rear ones. The reason may be that the reprofiled rear wheels increase the curvatures and result in large contact patch work.

Another two cases of tread contact of AAR wheels include a fully loaded car running at 45 mph and an empty car running at 60 mph. These have similar final and consecutive wear profiles, as does the previous case. For the case of 60 mph (Fig. 39), the small amount of flange wear which occurs in the front wheels is due to the large oscillating amplitude of the contact patch position over the front wheels. It is concluded that the wheel wear profiles for tread contact are nearly independent of train speeds and load conditions; however, different train speeds and load conditions cause different wear rates.

From Fig. 38, by comparison of the two cases of 45, AAR, empty, T and 60, AAR, empty, T, the wear rates of the front wheels for 60, AAR, empty, T are less than the wear rates of the front wheels for 45, AAR, empty, T. However, the wear rates of the rear wheels for 60, AAR, empty, T are larger than the wear rates of the rear wheels for 45, AAR, empty, T. That is to say the higher train speed causes more wear on the rear wheels but less wear on the front wheels.

From Fig. 38, by looking at the two cases of 45, AAR, empty, T and 45, AAR, full, T, the wear rates are not comparable, because they do not have the same scale factors. However, it still appears that the wear rates of the rear wheels are higher than the wear rates of the front wheels for both cases. Additionally, for the case of 45, AAR, full, T, the wear rates of the rear wheels are about twice as much as those of the front ones, but it is not true for the case of 45, AAR, full, T. It can be noted that the more heavily loaded car causes more wear on the rear wheels.

Case	SC	$\bar{Q}_{RF}$	$\bar{Q}_{LF}$	$\bar{Q}_{RR}$	$\bar{Q}_{LR}$	$N_F$	$N_R$	Ref. figures
45,AAR,empty,T	0.03	0.8126	0.8212	0.9665	1	103	125	Fig.34-Fig.36
45,AAR,full,T	0.04	0.5697	0.5569	1	0.9972	69	123	
60,AAR,empty,T	0.03	0.5749	0.5444	0.9879	1	72	135	Fig.39
45,HEU,empty,T	0.03	0.7961	0.7966	1	0.9971	83	105	
45,HEU,full,T	0.05	0.7022	0.7369	0.9648	1	80	110	
60,HEU,empty,T	0.06	0.8223	0.8006	1	0.9982	62	75	Fig.40-Fig.42
45,AAR,empty,F	0.03	0.9993	1	0.8123	0.8254	130	120	Fig.43-Fig.45
45,AAR,empty,F	0.04	0.9976	1	0.7097	0.7035	105	76	
45,HEU,empty,F	0.05	1	0.9663	0.9105	0.8999	123	100	

SC = scale factor

$\bar{Q}_{RF}$  = relative wear rate (in<sup>3</sup>/in) for right-front wheel

$\bar{Q}_{LF}$  = relative wear rate (in<sup>3</sup>/in) for left-front wheel

$\bar{Q}_{RR}$  = relative wear rate (in<sup>3</sup>/in) for right-rear wheel

$\bar{Q}_{LR}$  = relative wear rate (in<sup>3</sup>/in) for left-rear wheel

$N_F$  = number of front wheels profile changes

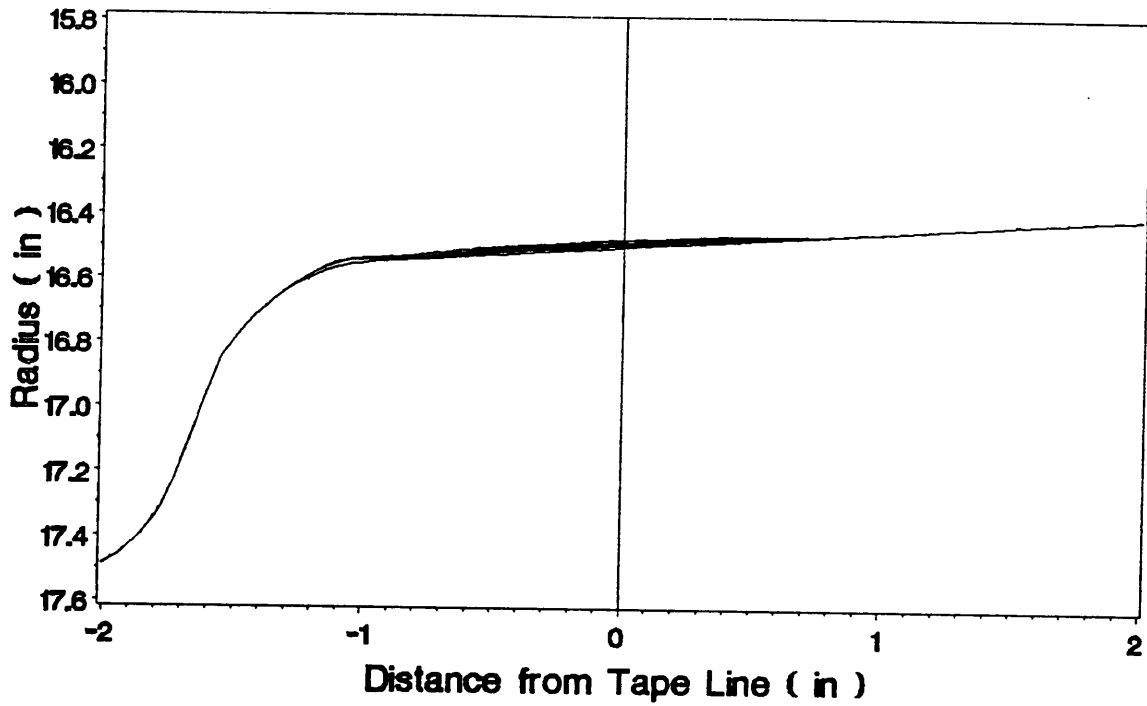
$N_R$  = number of rear wheels profile changes

45,AAR,empty,T = empty car running at 45 (mph) with AAR wheels for tread contact

60,HEU,full,F = fully loaded car running at 60 (mph) with Heumann wheels for flange contact

Figure 38. Summary of the results

### Right-Front Wheel Profile



### Right-Rear Wheel Profile

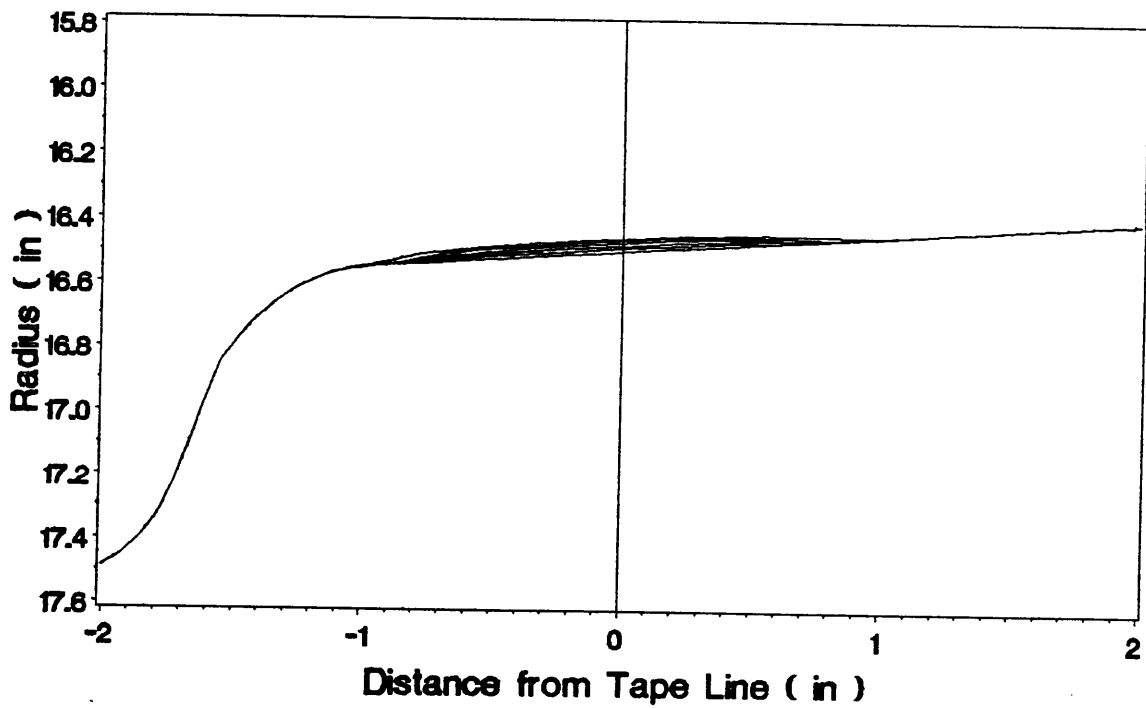


Figure 39. The consecutive wear profiles of the right wheels (60,AAR,empty,T)

The same train speed and load conditions are chosen to simulate the Heumann wheel running on the new 132-RE rail for tread contact. Fig. 40 to Fig. 42 are examples of the empty car with the Heumann wheels running at 60 mph.

The top of Fig. 40 shows the front and rear wheelset lateral displacements. It can be seen that flange contact occurs in the front wheels when the front wheelset lateral displacements are over 0.29 in. Fig. 40 also shows the final wear profiles, and Fig. 41 and Fig. 42 show the consecutive wear profiles. There is some flange wear in the front wheels, but only tread wear occurs in the rear wheels.

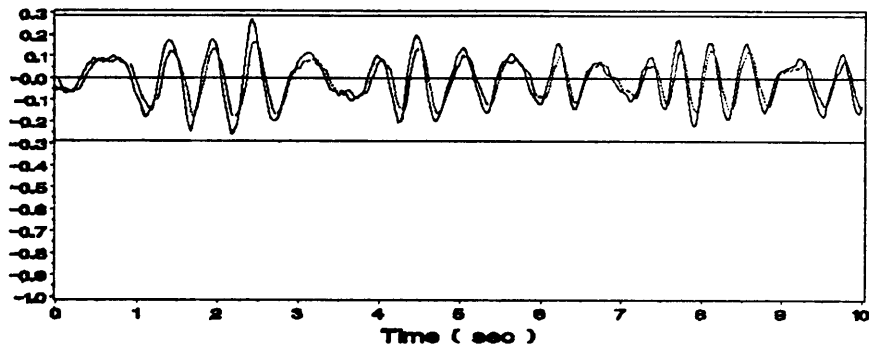
From Fig. 38, it can be noted that the three cases of Heumann wheels have similar characteristics as the AAR Wheels generally. However, Heumann wheels tends to reduce the difference of wear between the front and rear wheels. So, for tread contact the AAR wheels and the Heumann wheels have similar wear profiles. And the wear profiles are similar no matter what the train speeds and load conditions are.

### **5.3 Wear in Flange Contact**

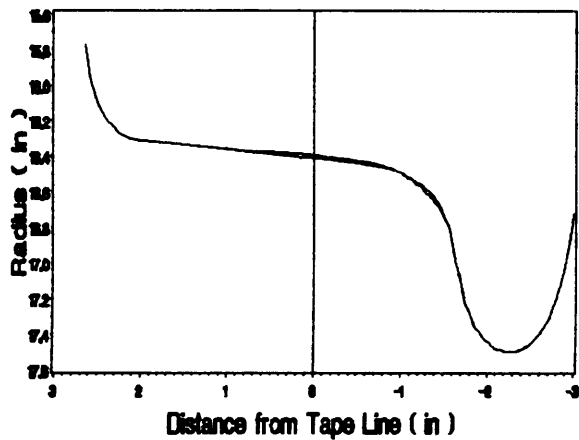
Flange contact usually occurs when trains are running at high speed or on curved tracks. Fig. 39 shows that the empty car running at 60 mph has slight flange wear, because of the higher train speed. In order to simulate flange contact, the random rail alignment magnitude is increased to get the larger wheelset lateral displacement which causes the frequent flange contact.

Three cases of slight flange contact are shown in Fig. 38. A case of the empty car with AAR wheels running at 45 mph is presented from Fig. 43 to Fig. 45. Fig. 43 shows the lateral position of wheelsets and the final wheel wear profiles. Since there are many time steps when the front wheelset lateral position is more than  $\pm 0.29$  in., flange contact occurs frequently.

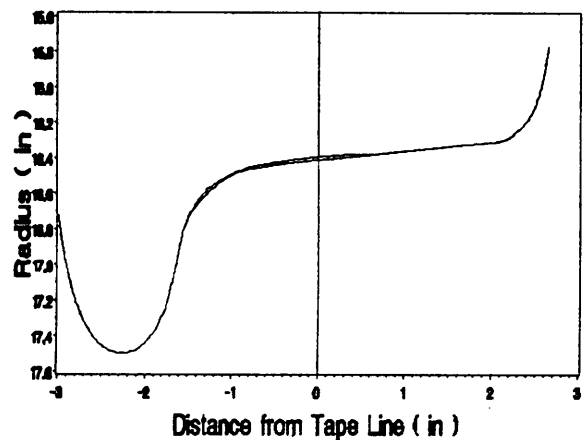
### Front/Rear Wheelset Lateral Displacement ( in )



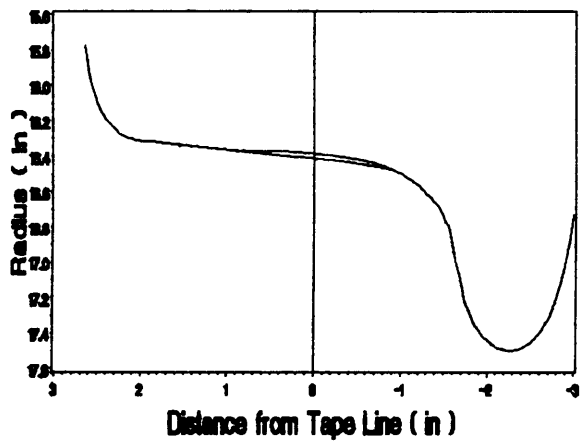
Left-Front Wheel Profile



Right-Front Wheel Profile



Left-Rear Wheel Profile



Right-Rear Wheel Profile

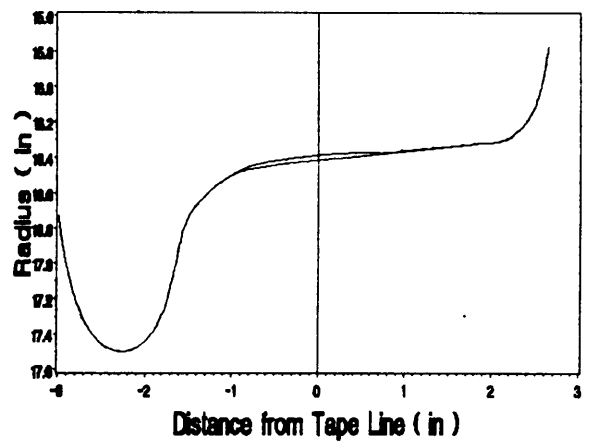
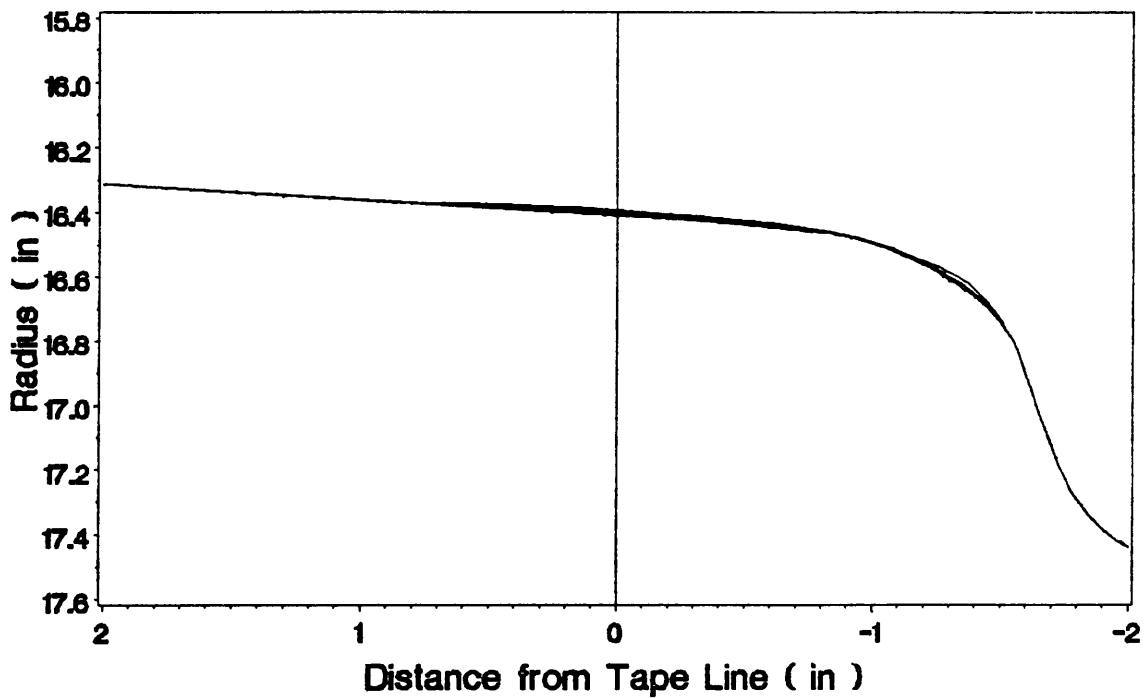


Figure 40. The lateral position of wheelsets and final wheel wear profiles (60,HEU,empty,T)

### Left-Front Wheel Profile



### Left-Rear Wheel Profile

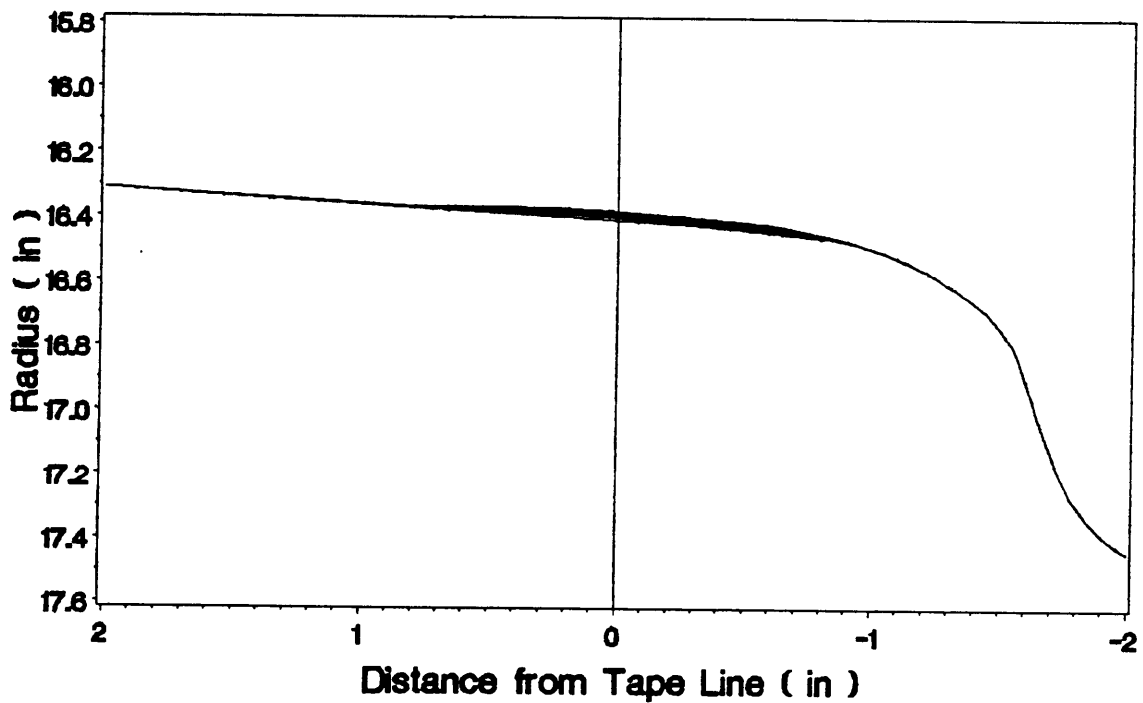
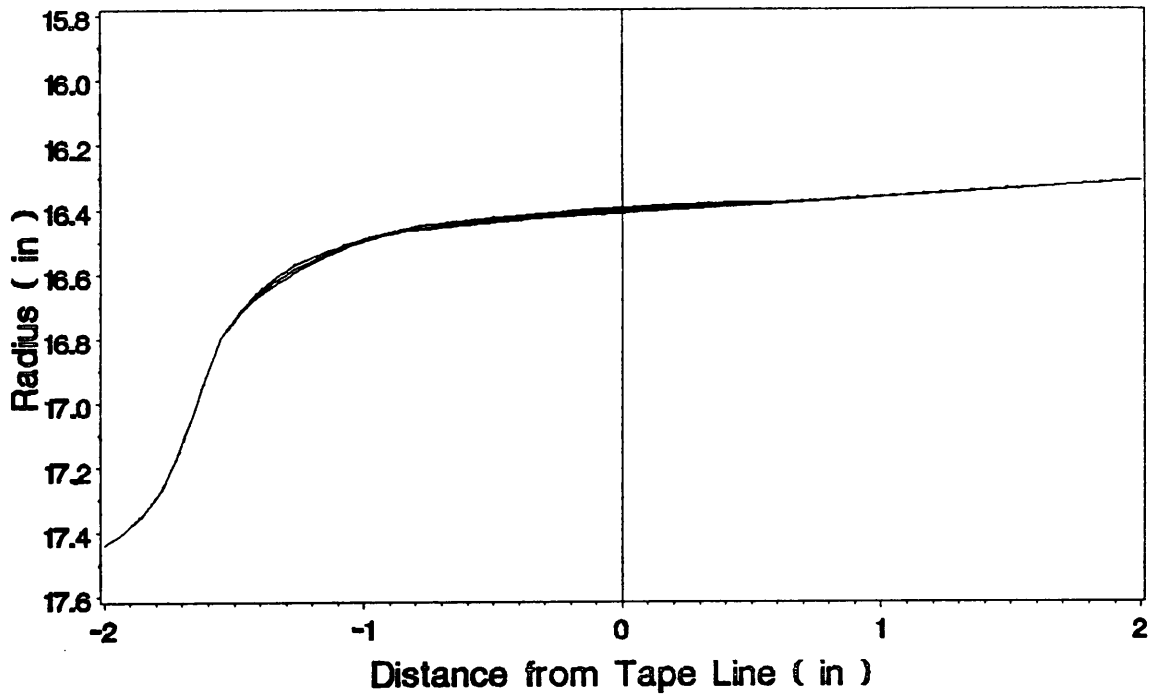


Figure 41. The consecutive wear profiles of the left wheels (60,HEU,empty,T)

### Right-Front Wheel Profile



### Right-Rear Wheel Profile

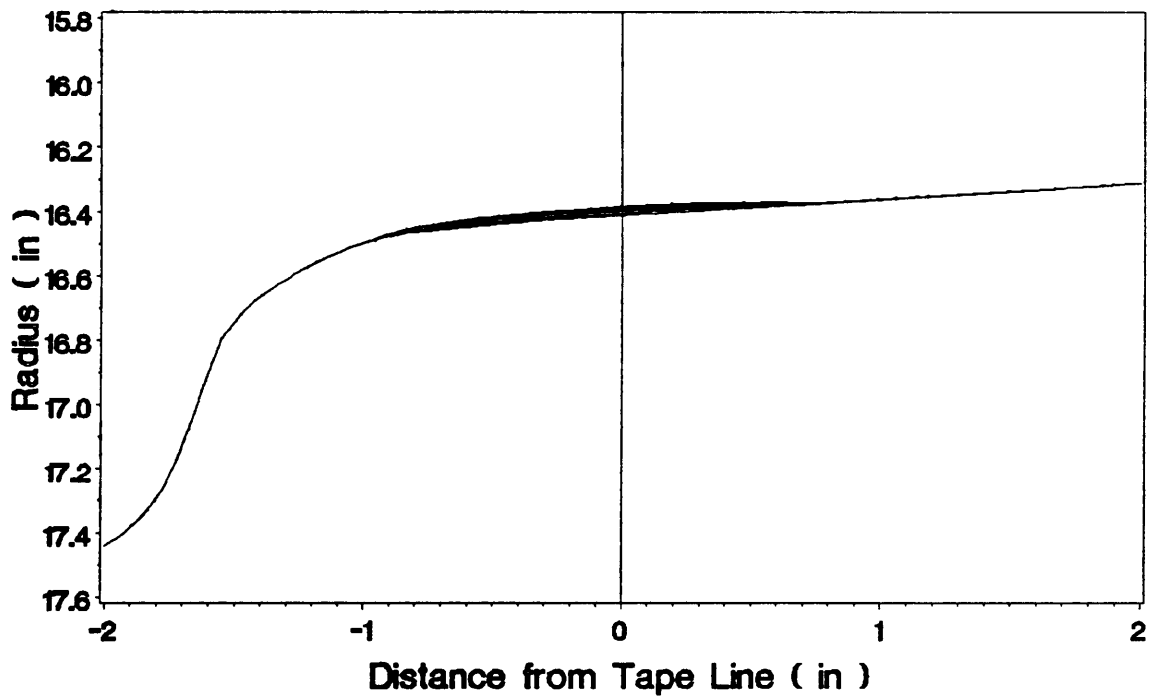
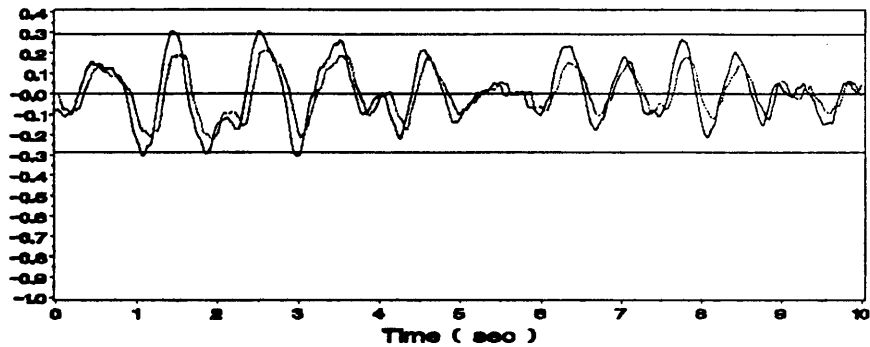
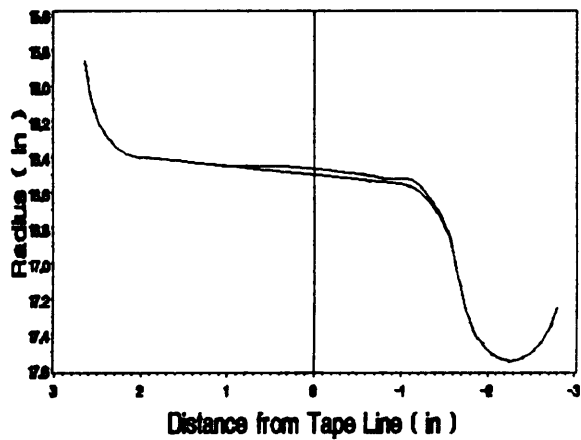


Figure 42. The consecutive wear profiles of the right wheels (60,HEU,empty,T)

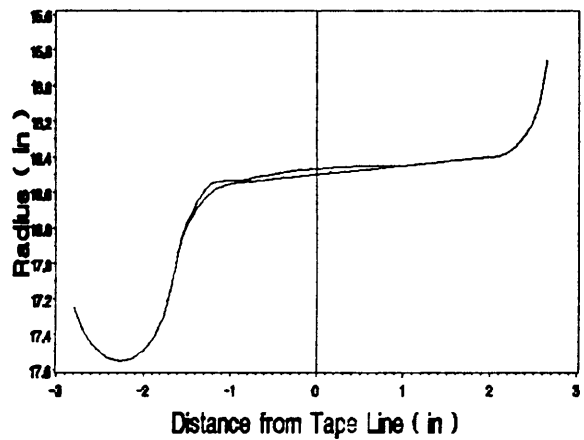
### Front/Rear Wheelset Lateral Displacement ( in )



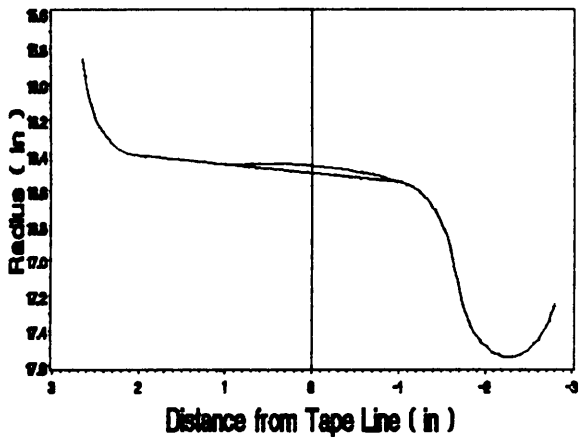
Left-Front Wheel Profile



Right-Front Wheel Profile



Left-Rear Wheel Profile



Right-Rear Wheel Profile

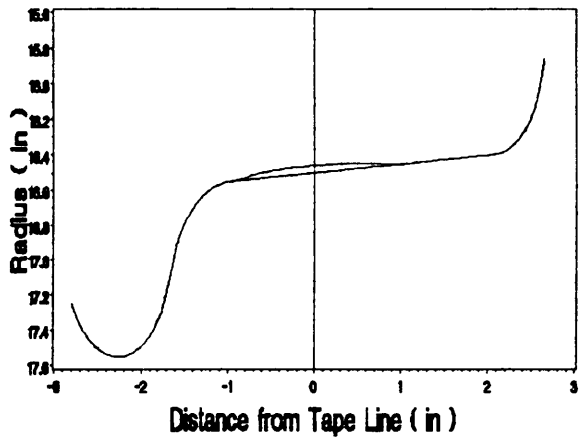
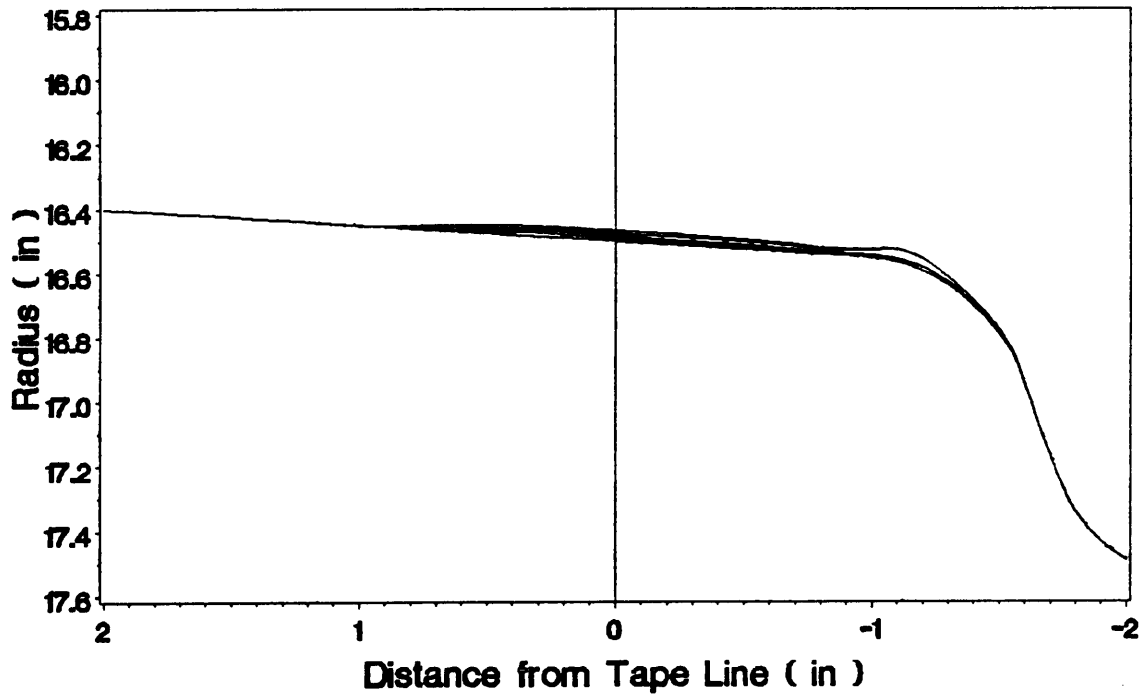


Figure 43. The lateral position of wheelsets and final wheel wear profiles (45,AAR,empty,F)

## Left-Front Wheel Profile



## Left-Rear Wheel Profile

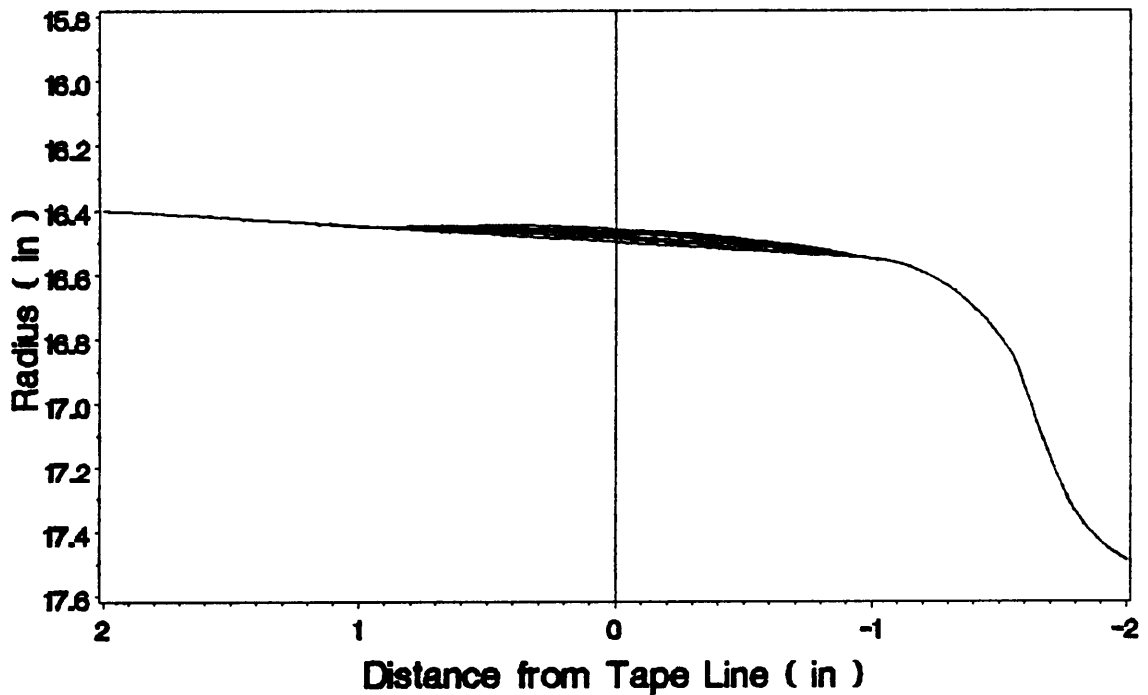
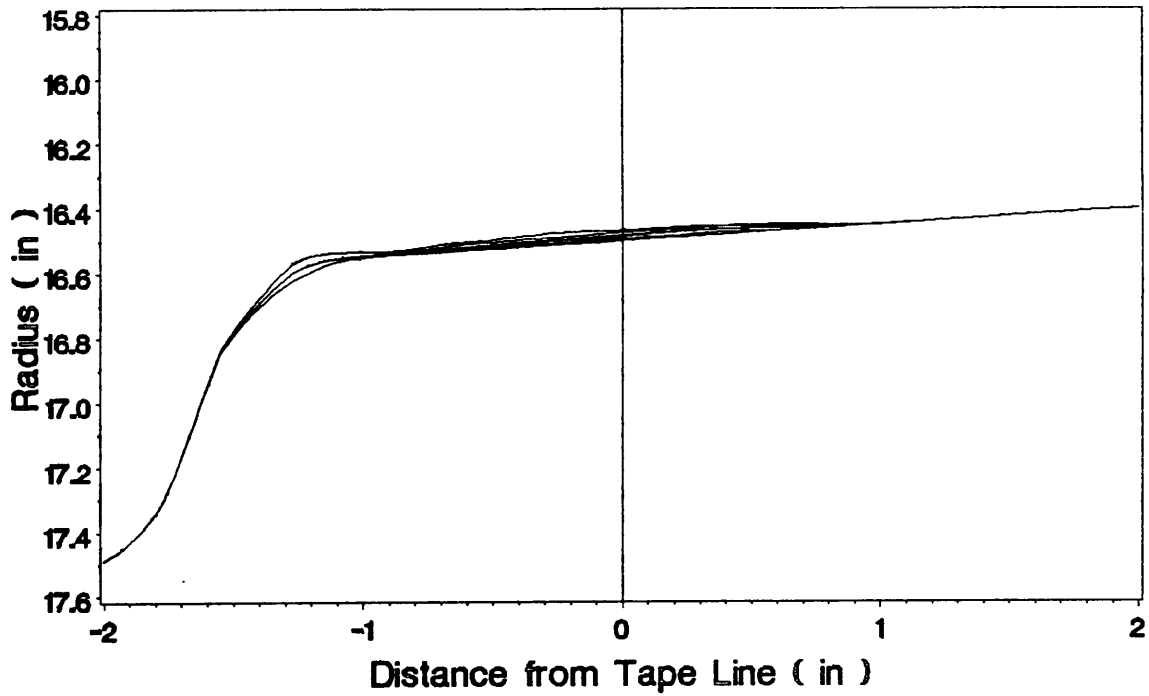


Figure 44. The consecutive wear profiles of the left wheels (45,AAR,empty,F)

## Right-Front Wheel Profile



## Right-Rear Wheel Profile

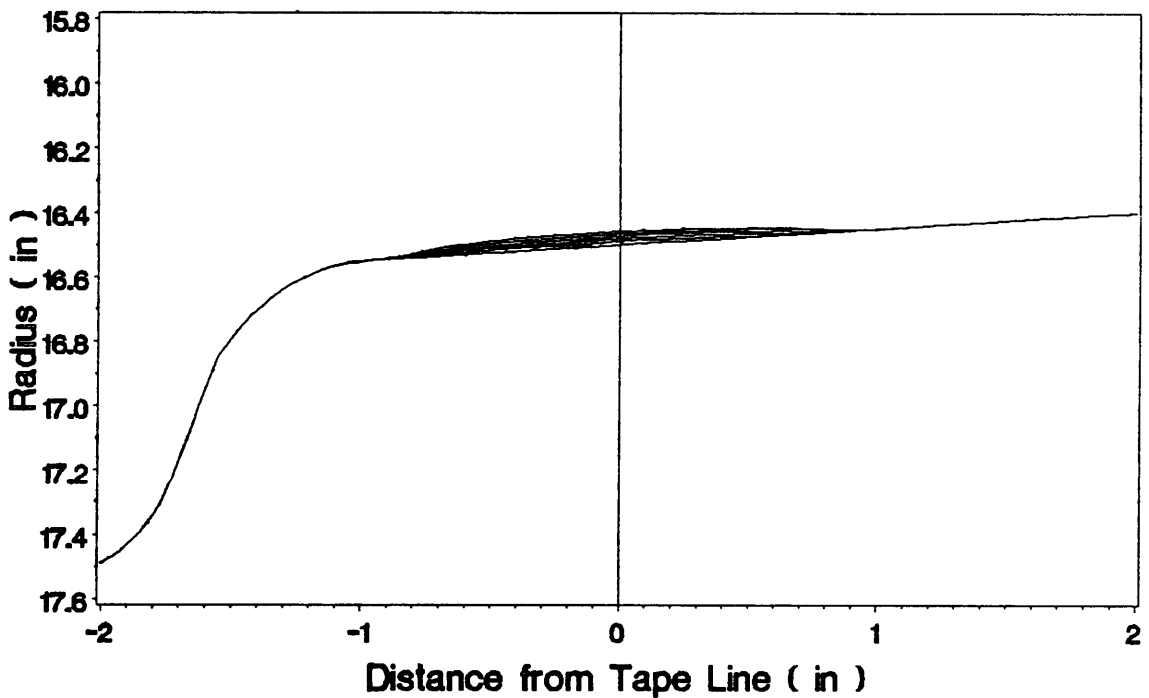


Figure 45. The consecutive wear profiles of the right wheels (45,AAR,empty,F)

Therefore, the wear profiles of the front wheels have a different pattern from the wear profiles of the rear wheels, because the front wheels have slight flange contact and the rear wheels have tread contact. Because of the dynamic response, flange contact occurs on the front wheels at lower speeds than it occurs on the rear wheels and causes higher wear rates on the front wheels than on the rear wheels.

Fig. 44 and Fig. 45 show the consecutive wear profiles. The rear wheels have the similar wear profile as demonstrated in Section 5.2, but the front wheels exhibit the flange wear. The larger lateral displacement of the front wheelset can be seen from the distribution of the lateral position in Fig. 43. The flange contact occurs in the front wheels occasionally, such that only three consecutive wear profiles are observed. From Fig. 38, the wear rates for the front wheels are larger than the wear rates for the rear wheels, since the front wheels are subjected to the flange contact. The front wheels have 130 profile changes, and the rear wheels have 120.

Fig. 46 shows standard AAR wheel wear profiles from the experimental results of Marcotte et al. (1980). Comparing Fig. 45 and Fig. 46, the predicted wear profiles for slight flange contact agree qualitatively with the experimental results of Marcotte et al. (1980). However, the program WWPPVW failed to simulate more severe flange contact. Since the flange contact causes more contact patch work, the wear volume becomes higher. During the simulation, the program fails in calculating the contact patch area by the Hertzian contact theory, because the wheels at the flange become too curved, and the wheel/rail contact becomes conformal contact which is not treated in this work.

Two additional cases for slight flange contact are summarized in Fig. 38. One is the empty car with AAR wheels running at 45 mph ( $SC=0.04$  different from previous case  $SC=0.03$ ), and another is the empty car with Heumann wheels running at 45mph. Both cases have wear profiles similar to the previous cases.

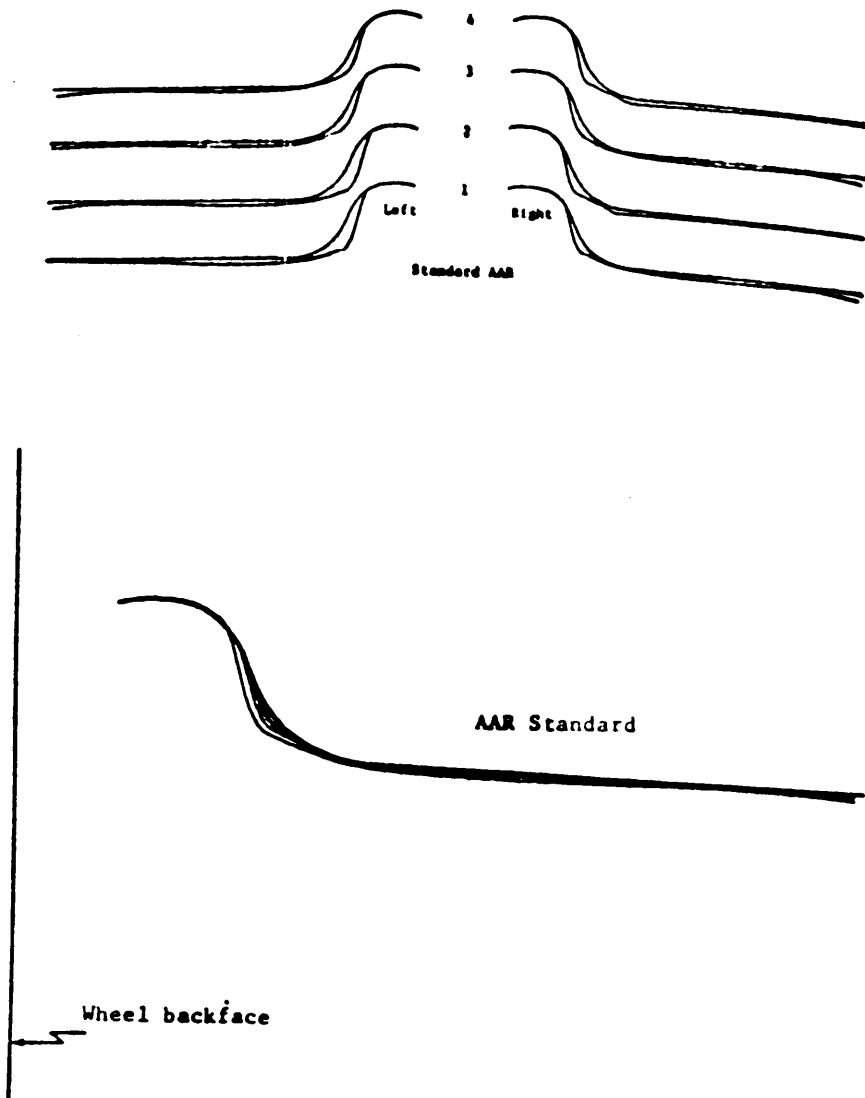


Figure 46. The experimental wear profiles of AAR wheels (Marcotte et al., 1980)

Fig. 38 summarizes the scale factors, the wear rates and the number of profile changes for all the cases presented in this chapter for the different wheels, train speeds and load conditions. Note that wear rates are scaled, and they are comparable only in the cases having the same scale factors (SC).

In comparing the cases of 45,AAR,empty,T and 45,AAR,empty,F, both have the same conditions except the former for tread contact and the latter for slight flange contact. The wear rates of the front wheels for flange contact are larger than the wear rates of the front wheels for tread contact, and the wear rates of the rear wheels are nearly the same for both tread and flange contacts. A comparison of Heumann wheels of 45,HEU,empty,T and 45,HEU,empty,F shows similar wear patterns. It may be concluded that because flange contact occurs only on the front wheels for slight flange contact, the wear rates of the front wheels become large. In addition, because there is no flange contact in rear wheels, the wear rates of the rear wheels remain the same as that for tread contact.

### **Summary**

1. The wheel wear profile prediction of the tread and slight flange contact for empty and fully loaded car with AAR and Heumann wheels running at 45 and 60 mph are presented.
2. For tread contact, the AAR and Heumann wheel wear profiles are slightly curved and similar. Also the wear profiles are nearly independent of train speeds and load conditions; however, the different train speeds and load conditions cause different wear rates.
3. For tread contact, the right and left wheels have nearly the same wear rate, but the rear wheels have more wear than the front wheels. The higher train speed causes more wear on the rear wheels but less wear on the front wheels; also the higher loaded car causes more wear on the rear wheels.

4. For slight flange contact, the flange wear is predictable, but when the flange contact is significant, the simulation fails due to the wheel/rail contact becoming conformal.
5. For slight flange contact, the front wheels encounter flange contact ahead of the rear wheels, so the wear rates of the front wheels becomes large. No flange contact occurs in the rear wheels, hence the wear of the rear wheels remains the same as that for tread contact.
6. These results agree well qualitatively with previous predictions by Davila (1986).
7. The AAR slight flange contact results agree well qualitatively with field wear results present by Marcotte et al. (1980).

## **Chapter 6 : Conclusion and Recommendation**

### **6.1 Conclusion**

The contact patch work wear model is applied to predict the wheel wear profiles in this work. A discretized method is used to determine the contact patch work, and it allows computation of the distribution of the work done in the contact patch. It is the major difference between the current work from Davila's. He assumed that the distribution of the work done in the contact patch is parabolic. This assumption is valid only under certain conditions, for example the case of the partial slip on the contact patch shown in Fig. 17, and it is not correct for some cases, such as the example of full slip region shown in Fig. 18.

The discretized method accounts for the distribution of the contact patch work, so it remedies the weakness of Davila's assumption. However, this discretized method requires substantially more computer time.

All of the results shown in Fig. 38 are performed for 10 seconds. Since the samples collected in 10 seconds might not be representative enough, a longer period of simulation is desirable. However, on the basis of considering the CPU time and the accurate prediction of wheel wear

profiles, a compromise was made. Several cases simulated for 30 s have similar wear profiles as those predicted for 10 s simulations for tread contact. Therefore, the 10 s simulation appears to be acceptable.

This work includes the prediction of the wheel wear profile for both tread contact and slight flange contact, and the outcomes of the simulation agree with the experimental results. Since flange contact causes more wear, and it results in the wheel profile being too curved, the wheel/rail contact becomes conformal. The conformal contact makes the Hertzian contact theory inapplicable in calculating the contact area, and it makes the further simulation impossible.

Some characteristics of the wheel wear process of the half car model for the tread and slight flange contacts are observed. The right and left wheels have nearly the same wear rates, but the rear wheels have more wear than the front ones. Furthermore, the higher train speed causes more wear on the rear wheels but less wear on the front wheels. Also, the flange contact occurs in the front wheels ahead of the rear wheels.

The 5-degree-of-freedom half-car model is implemented to describe the truck dynamic response, and the hunting phenomenon on tangent track is observed. In addition, when wheels become worn, the perturbation of the spin angular velocity is no longer negligible. The equation of wheelset spin is added to determine the perturbation of the spin angular velocity. Both the truck response and the spin angle of wheelset are employed to obtain the creepages.

This work also relates the wear index coefficient for rolling contact and the wear coefficient for sliding contact. Both of the coefficients are connected with the hardness of materials and with the friction coefficient of contact area. The wear index coefficient found in rail vehicle literature are of the order of  $10^{-9} \frac{\text{in}^2}{\text{lb}}$  for dry clean surface. The wear index coefficient equates to wear coefficient in the order of  $10^{-4}$ .

The wear predictions in tread contact agree well qualitatively with previous predictions by Davila (1986). Also, the AAR slight flange contact results agree well qualitatively with field wear results presented by Marcotte et al. (1980).

## **6.2 Recommendations**

Since the discretized method of the calculation of the contact patch work consumes enormous CPU time for simulations, it would be beneficial to conduct the simulations from the point of view of statistics. A statistical method could obtain the probability density function of the creepages along the wheel profile, and calculate the distribution of the contact patch work along the wheel profile according to the density function. This statistical method will not only reduce the CPU time but also resolve the concern for the shortness of the simulations runs used in this work.

When the wheel is highly worn, and the wheel and rail contact becomes conformal, then the Hertzian contact theory is no longer acceptable. In this work, the program WWPPVW fails to calculate the contact area due to the conformal contact, so further research treating the wheel and rail contact as non-Hertzian is necessary, and the determination of the contact area and the creep force and moment needs also to be based on the non-Hertzian contact.

Once the non-Hertzian contact is treated, it is foreseeable that to simulate wheel wear for much larger wear volume is possible. It will become more practical to predict wheel flange wear and to compare to field worn profiles.

The current work focuses on the wheel and rail contact on the tangent track, and the tread contact is the major concern. For railway vehicles, the flange contact and the curving motion are equally or even more interesting, since the curving motion causes the flange contact and

the flange contact has more wear than the tread contact. So, to introduce a curving model for rail vehicle in predicting flange wear is a worthwhile challenge.

Although the wear index coefficient is related to the wear coefficient, during the simulation the wear index coefficient is not really used; instead, a scale factor is introduced to perform the simulation. It is another challenge to explore the employ of the wear index coefficient in the wear simulation. This would give a measure of the actual distances traveled for a given wear volume.

# Appendix A. Derivation of Equations of Motion for a Wheelset

This appendix presents the derivation of the equations of motion of a wheelset by using Newton-Euler's equation. Section A.1 defines the nomenclature. Section A.2 describes the coordinate systems of a wheelset. Section A.3 shows the complete derivation of equations of motion. In addition, the wheelset external force and moment are defined, and they are the external force and moment acting on a wheelset.

## A.1 Nomenclature

The nomenclature used to develop equations of motion for wheelset are as follows

$X'''$ ,  $Y'''$ ,  $Z'''$  = Equilibrium coordinate,  $X'''$  along the center line of the track

$X''$ ,  $Y''$ ,  $Z''$  = Intermediate coordinate rotated an angle  $\psi$  about  $Z'''$

$X'$ ,  $Y'$ ,  $Z'$  = Wheelset coordinate rotated an angle  $\phi$  about  $X''$

$\bar{i}'''$ ,  $\bar{j}'''$ ,  $\bar{k}'''$  = Unit vector of equilibrium coordinate system,  $X'''$ ,  $Y'''$ ,  $Z'''$

$\vec{i}'' , \vec{j}'' , \vec{k}''$	=	Unit vector of intermediate coordinate system, $X'' , Y'' , Z''$
$\vec{i}' , \vec{j}' , \vec{k}'$	=	Unit vector of wheelset coordinate system, $X' , Y' , Z'$
$\vec{e}_{1R} , \vec{e}_{2R} , \vec{e}_{3R}$	=	Unit vector of contact plane axes of right wheel
$\vec{e}_{1L} , \vec{e}_{2L} , \vec{e}_{3L}$	=	Unit vector of contact plane axes of left wheel
$\vec{\omega}_W$	=	angular velocity of wheelset
$\phi$	=	roll angular displacement about $X''$ axis
$\psi$	=	yaw angular displacement about $Z''$ axis
$\beta$	=	perturbation angular displacement from a nominal angular velocity $\Omega$ about $Y'$ axis
$\Omega$	=	nominal angular velocity, $\frac{V}{R_0}$
$R_0$	=	nominal wheelset rolling radius
$R_R$	=	rolling radius of contact point at the right wheel
$R_L$	=	rolling radius of contact point at the left wheel
$V$	=	wheelset moving speed
$\vec{V}_W$	=	velocity of wheel
$\vec{V}_T$	=	velocity of rail
$\vec{\omega}_W$	=	angular velocity of wheel
$\vec{\omega}_T$	=	angular velocity of rail
$\vec{R}_R$	=	position vector of right contact point
$\vec{R}_L$	=	position vector of left contact point
$\vec{H}'$	=	angular momentum of wheelset in body coordinate
$\vec{\omega}_{axis}$	=	angular velocity of body coordinate relative to equilibrium coordinate

Others are consistent with those in Chapter 3.

## A.2 Coordinate System of the Wheelset

The coordinate systems of the wheelset references to Fig. 47.  $(X''', Y''', Z''')$  are the equilibrium coordinates in which the direction of  $X'''$  is along the center line of track.  $(X'', Y'', Z'')$  represent the intermediate coordinates which are rotated  $\psi$  about  $Z'''$ .  $(X', Y', Z')$  are defined as the wheelset coordinates which are rotated  $\phi$  about  $X''$ . By assuming small angle and neglecting the higher order terms, the transformation equations between the unit vectors for the coordinate systems are

$$\begin{bmatrix} \vec{i}' \\ \vec{j}' \\ \vec{k}' \end{bmatrix} = \begin{bmatrix} 1 & 0 & 0 \\ 0 & \cos \phi & \sin \phi \\ 0 & -\sin \phi & \cos \phi \end{bmatrix} \begin{bmatrix} \vec{i}'' \\ \vec{j}'' \\ \vec{k}'' \end{bmatrix} \quad (\text{A.1})$$

$$\begin{bmatrix} \vec{i}'' \\ \vec{j}'' \\ \vec{k}'' \end{bmatrix} = \begin{bmatrix} \cos \psi & \sin \psi & 0 \\ -\sin \psi & \cos \psi & 0 \\ 0 & 0 & 1 \end{bmatrix} \begin{bmatrix} \vec{i}''' \\ \vec{j}''' \\ \vec{k}''' \end{bmatrix} \quad (\text{A.2})$$

$$\begin{bmatrix} \vec{i}' \\ \vec{j}' \\ \vec{k}' \end{bmatrix} = \begin{bmatrix} 1 & \psi & 0 \\ -\psi & 1 & \phi \\ 0 & -\phi & 1 \end{bmatrix} \begin{bmatrix} \vec{i}''' \\ \vec{j}''' \\ \vec{k}''' \end{bmatrix} \quad (\text{A.3})$$

In additions, the contact patch coordinate system at the right and left wheel are shown in Fig. 48. The transformation equations between the contact patch coordinates and the equilibrium coordinates for small angle and neglecting higher order terms are

$$\begin{bmatrix} \vec{e}_{1L} \\ \vec{e}_{2L} \\ \vec{e}_{3L} \end{bmatrix} = \begin{bmatrix} 1 & \psi & 0 \\ -\psi & 1 & (\delta_L + \phi) \\ 0 & -(\delta_L + \phi) & 1 \end{bmatrix} \begin{bmatrix} \vec{i}''' \\ \vec{j}''' \\ \vec{k}''' \end{bmatrix} \quad (\text{A.4})$$

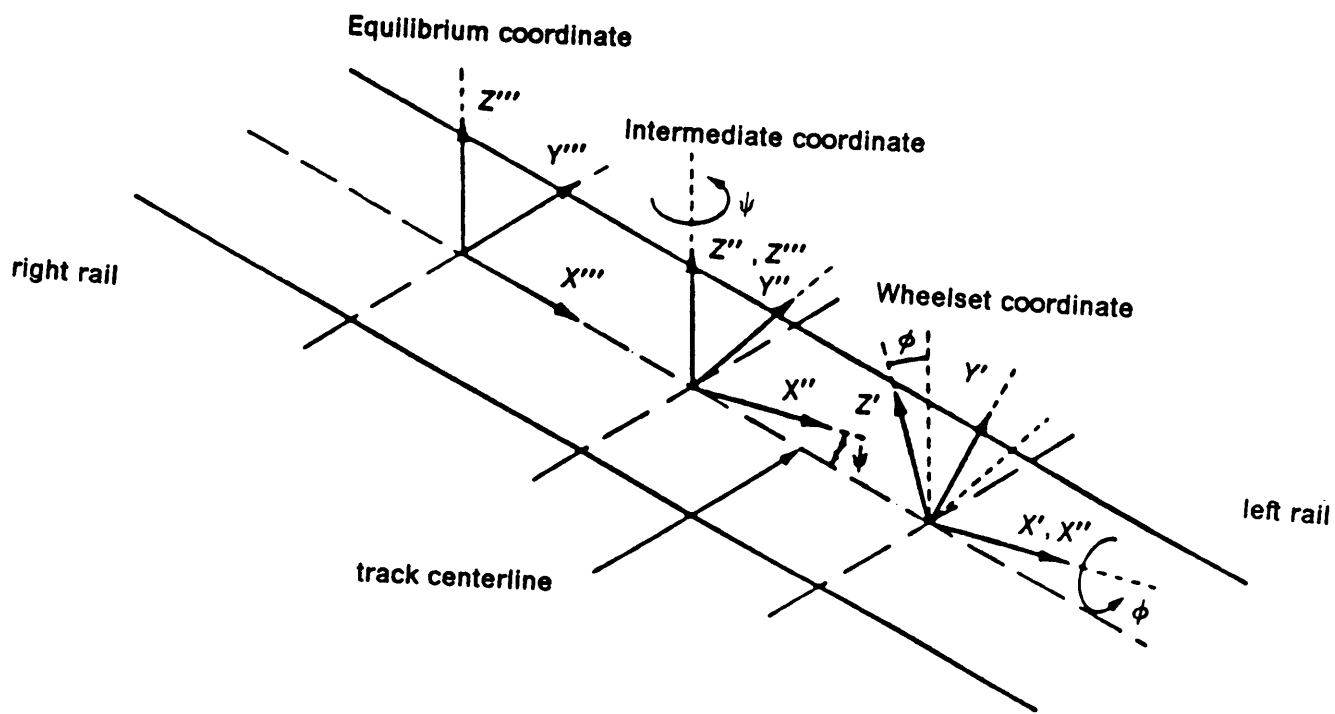


Figure 47. Coordinate system of wheelset

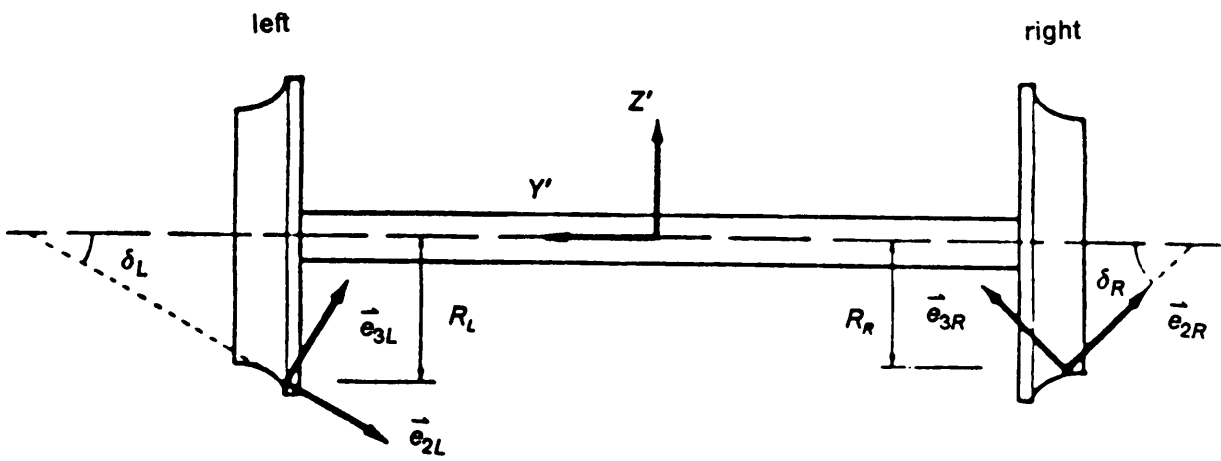


Figure 48. Contact patch coordinate system

$$\begin{bmatrix} \vec{e}_{1R} \\ \vec{e}_{2R} \\ \vec{e}_{3R} \end{bmatrix} = \begin{bmatrix} 1 & \psi & 0 \\ -\psi & 1 & -(\delta_R - \phi) \\ 0 & (\delta_R - \phi) & 1 \end{bmatrix} \begin{bmatrix} \vec{i}''' \\ \vec{j}''' \\ \vec{k}''' \end{bmatrix} \quad (\text{A.5})$$

### A.3 Wheelset Equations

Newton-Euler's equations is used to derive the equations of motion of the wheelset. The angular velocity and the angular momentum of the wheelset are derived and expressed in the equilibrium coordinates. The angular velocity of the wheelset is

$$\vec{\omega} = \dot{\phi} \vec{i}'' + (\Omega + \dot{\beta}) \vec{j}' + \dot{\psi} \vec{k}'' \quad (\text{A.6})$$

And  $\vec{\omega}$  can be expressed in the body coordinates ( $X', Y', Z'$ )

$$\vec{\omega} = \omega_X \vec{i}' + \omega_Y \vec{j}' + \omega_Z \vec{k}' \quad (\text{A.7})$$

where

$$\omega_X = \dot{\phi} \quad (\text{A.8})$$

$$\omega_Y = \Omega + \dot{\beta} + \dot{\psi} \sin \phi \quad (\text{A.9})$$

$$\omega_Z = \dot{\psi} \cos \phi \quad (\text{A.10})$$

The angular momentum of the wheelset in the body coordinates is

$$\begin{aligned} \vec{H}' &= I_{WX} \omega_X \vec{i}' + I_{WY} \omega_Y \vec{j}' + I_{WZ} \omega_Z \vec{k}' \\ &= H_X'' \vec{i}''' + H_Y'' \vec{j}''' + H_Z'' \vec{k}''' \end{aligned} \quad (\text{A.11})$$

where

$$H_X''' = I_{WX} \omega_X \cos \psi - I_{WY} \omega_Y \cos \phi \sin \psi + I_{WZ} \omega_Z \sin \phi \sin \psi \quad (\text{A.12})$$

$$H_Y''' = I_{WX} \omega_X \sin \psi + I_{WY} \omega_Y \cos \phi \cos \psi - I_{WZ} \omega_Z \sin \phi \cos \psi \quad (\text{A.13})$$

$$H_Z''' = I_{WY} \omega_Y \sin \phi + I_{WZ} \omega_Z \cos \phi \quad (\text{A.14})$$

The rate change of the angular momentum of wheelset in the body coordinate is

$$\frac{d\vec{H}'}{dt} = I_{WX} \dot{\omega}_X \vec{i}' + I_{WY} \dot{\omega}_Y \vec{j}' + I_{WZ} \dot{\omega}_Z \vec{k}' + \vec{\omega}_{axis} \times \vec{H}' \quad (\text{A.15})$$

where  $\vec{\omega}_{axis}$  is the angular velocity of the body coordinates.

$$\begin{aligned} \vec{\omega}_{axis} &= \dot{\phi} \vec{i}'' + \dot{\psi} \vec{k}''' \\ &= \dot{\phi} \vec{i}' + \dot{\psi} \sin \phi \vec{j}' + \dot{\psi} \cos \phi \vec{k}' \end{aligned} \quad (\text{A.16})$$

Therefore,

$$\begin{aligned} \frac{d\vec{H}'}{dt} &= I_{WX} \ddot{\phi} \vec{i}' + I_{WY} (\ddot{\beta} + \ddot{\psi} \sin \phi + \dot{\psi} \dot{\phi} \cos \phi) \vec{j}' + I_{WZ} (\ddot{\psi} \cos \phi + \dot{\psi} \dot{\phi} \sin \phi) \vec{k}' \\ &+ (\dot{\phi} \vec{i}' + \dot{\psi} \sin \phi \vec{j}' + \dot{\psi} \cos \phi \vec{k}') \times (I_{WX} \omega_X \vec{i}' + I_{WY} \omega_Y \vec{j}' + I_{WZ} \omega_Z \vec{k}') \end{aligned} \quad (\text{A.17})$$

By differentiating (A.12)-(A.14) and assuming small angle, the rate change of the angular momentum in the equilibrium coordinates ( $X'''$ ,  $Y'''$ ,  $Z'''$ ) becomes

$$\frac{d\vec{H}'''}{dt} = \dot{H}_X''' \vec{i}''' + \dot{H}_Y''' \vec{j}''' + \dot{H}_Z''' \vec{k}''' \quad (\text{A.18})$$

where

$$\dot{H}_X''' = I_{WX} \ddot{\phi} - I_{WY} \Omega \dot{\psi} \quad (\text{A.19})$$

$$\dot{H}_Y''' = I_{WY}\ddot{\beta} \quad (\text{A.20})$$

$$\dot{H}_Z''' = I_{WY}\Omega\dot{\phi} + I_{WZ}\ddot{\psi} \quad (\text{A.21})$$

From Newton-Euler's equations,

$$\sum \vec{F} = M\vec{R} \quad (\text{A.22})$$

$$\sum \vec{M} = \frac{d\vec{H}}{dt} \quad (\text{A.23})$$

Based on the Equilibrium Coordinate ( $X'''$ ,  $Y'''$ ,  $Z'''$ ),

$$\sum \vec{F} = \vec{F}_L + \vec{F}_R + \vec{N}_L + \vec{N}_R + \vec{F}_S - W_A \vec{k}''' \quad (\text{A.24})$$

$$\sum \vec{M} = \vec{R}_R \times (\vec{F}_R + \vec{N}_R) + \vec{R}_L \times (\vec{F}_L + \vec{N}_L) + \vec{M}_L + \vec{M}_R + \vec{M}_S \quad (\text{A.25})$$

$$\vec{R} = \ddot{x} \vec{i}''' + \ddot{y} \vec{j}''' + \ddot{z} \vec{k}''' \quad (\text{A.26})$$

$$\frac{d\vec{H}}{dt} = \{I_{WX}\ddot{\phi} - I_{WY}\Omega\dot{\psi}\} \vec{i}''' + \{I_{WY}\ddot{\beta}\} \vec{j}''' + \{I_{WY}\Omega\dot{\phi} + I_{WZ}\ddot{\psi}\} \vec{k}''' \quad (\text{A.27})$$

where

- $\vec{F}_L$  = creep force at the left wheel
- $\vec{F}_R$  = creep force at the right wheel
- $\vec{M}_L$  = creep moment at the left wheel
- $\vec{M}_R$  = creep moment at the right wheel
- $\vec{N}_L$  = normal force at the left wheel
- $\vec{N}_R$  = normal force at the right wheel
- $\vec{F}_s$  = suspension force
- $\vec{M}_s$  = suspension moment
- $\vec{R}_L$  = position vector of the contact point for the left wheel
- $\vec{R}_R$  = position vector of the contact point for the right wheel

The creep forces between the wheel and rail are considered as the two dimensional forces, so the creep forces vector at the left and right wheels are

$$\vec{F}_L = F'_{XL} \vec{e}_{1L} + F'_{YL} \vec{e}_{2L} \quad (A.28)$$

$$\begin{aligned} &= \{F'_{XL} \cos \psi - F'_{YL} \cos(\delta_L + \phi) \sin \psi\} \vec{i}''' \\ &\quad + \{F'_{XL} \sin \psi + F'_{YL} \cos(\delta_L + \phi) \cos \psi\} \vec{j}''' \\ &\quad + \{-F'_{YL} \sin(\delta_L + \phi)\} \vec{k}''' \end{aligned} \quad (A.29)$$

$$= F_{XL} \vec{i}''' + F_{YL} \vec{j}''' + F_{ZL} \vec{k}''' \quad (A.30)$$

$$\vec{F}_R = F'_{XR} \vec{e}_{1R} + F'_{YR} \vec{e}_{2R} \quad (A.31)$$

$$\begin{aligned} &= \{F'_{XR} \cos \psi - F'_{YR} \cos(\delta_R - \phi) \sin \psi\} \vec{i}''' \\ &\quad + \{F'_{XR} \sin \psi + F'_{YR} \cos(\delta_R - \phi) \cos \psi\} \vec{j}''' \end{aligned}$$

$$+ \{-F'_{YR} \sin(\delta_R - \phi)\} \vec{k}''' \quad (\text{A.32})$$

$$= F_{XR} \vec{i}''' + F_{YR} \vec{j}''' + F_{ZR} \vec{k}''' \quad (\text{A.33})$$

in which  $F'_{XL}$ ,  $F'_{YL}$ ,  $F'_{XR}$  and  $F'_{YR}$  are supported by the program FASTSIM which is discussed in Chapter 2. The creep moment between the wheel and rail accounts for only the vertical direction, so the creep moments at the right and left wheels are

$$\begin{aligned} \vec{M}_L &= M'_{ZL} \vec{e}_{3L} \\ &= \{M'_{ZL} \sin(\delta_L + \phi) \sin \psi\} \vec{i}''' - \{M'_{ZL} \sin(\delta_L + \phi) \cos \psi\} \vec{j}''' \\ &\quad + \{M'_{ZL} \cos(\delta_L + \phi)\} \vec{k}''' \end{aligned} \quad (\text{A.34})$$

$$= M_{XL} \vec{i}''' + M_{YL} \vec{j}''' + M_{ZL} \vec{k}''' \quad (\text{A.35})$$

$$\begin{aligned} \vec{M}_R &= M'_{ZR} \vec{e}_{3R} \\ &= \{-M'_{ZR} \sin(\delta_R - \phi) \sin \psi\} \vec{i}''' + \{M'_{ZR} \sin(\delta_R - \phi) \cos \psi\} \vec{j}''' \\ &\quad + \{M'_{ZR} \cos(\delta_R - \phi)\} \vec{k}''' \end{aligned} \quad (\text{A.36})$$

$$= M_{XR} \vec{i}''' + M_{YR} \vec{j}''' + M_{ZR} \vec{k}''' \quad (\text{A.37})$$

In which  $M'_{ZL}$  and  $M'_{ZR}$  are supported by the program FASTSIM. The normal forces and the position vectors of the contact points for the left and right wheels are

$$\begin{aligned} \vec{N}_L &= N_L \vec{e}_{3L} \\ &= \{N_L \sin(\delta_L + \phi) \sin \psi\} \vec{i}''' - \{N_L \sin(\delta_L + \phi) \cos \psi\} \vec{j}''' \end{aligned}$$

$$+ \{N_L \cos(\delta_L + \phi)\} \vec{k}''' \quad (\text{A.38})$$

$$= N_{XL} \vec{i}''' + N_{YL} \vec{j}''' + N_{ZL} \vec{k}''' \quad (\text{A.39})$$

$$\vec{N}_R = N_R \vec{e}_{3R}$$

$$= \{-N_R \sin(\delta_R - \phi) \sin \psi\} \vec{i}''' + \{N_R \sin(\delta_R - \phi) \cos \psi\} \vec{j}''' \\ + \{N_R \cos(\delta_R - \phi)\} \vec{k}''' \quad (\text{A.40})$$

$$= N_{XR} \vec{i}''' + N_{YR} \vec{j}''' + N_{ZR} \vec{k}''' \quad (\text{A.41})$$

$$\vec{R}_L = [- (A - \Delta_L) \cos \phi \sin \psi - R_L \sin \phi \sin \psi] \vec{i}''' \\ + [(A + \Delta_L) \cos \phi \cos \psi + R_L \sin \phi \cos \psi] \vec{j}''' \\ + [- (A + \Delta_L) \sin \phi - R_L \cos \phi] \vec{k}''' \quad (\text{A.42})$$

$$= R_{XL} \vec{i}''' + R_{YL} \vec{j}''' + R_{ZL} \vec{k}''' \quad (\text{A.43})$$

$$\vec{R}_R = [(A + \Delta_R) \cos \phi \sin \psi - R_R \sin \phi \sin \psi] \vec{i}''' \\ + [- (A + \Delta_R) \cos \phi \cos \psi + R_R \sin \phi \cos \psi] \vec{j}''' \\ + [- (A + \Delta_R) \sin \phi - R_R \cos \phi] \vec{k}''' \quad (\text{A.44})$$

$$= R_{XR} \vec{i}''' + R_{YR} \vec{j}''' + R_{ZR} \vec{k}''' \quad (\text{A.45})$$

By substituting eq. (A.24) - (A.45) into Newton-Euler's equations (eq. (A.22) and (A.23)), the equations of motion of the wheelset are summarized

**longitudinal equation**

$$M\ddot{x} = F_{XL} + F_{XR} + N_{XL} + N_{XR} + F_{XS} \quad (\text{A.46})$$

**lateral equation**

$$M\ddot{y} = F_{YL} + F_{YR} + N_{YL} + N_{YR} + F_{YS} \quad (\text{A.47})$$

**vertical equation**

$$M\ddot{z} = F_{ZL} + F_{ZR} + N_{ZL} + N_{ZR} + F_{ZS} \quad (\text{A.48})$$

**roll equation**

$$\begin{aligned} I_{WX}\ddot{\phi} - I_{WY}\Omega\dot{\psi} = & R_{YR}(F_{ZR} + N_{ZR}) - R_{ZR}(F_{YR} + N_{YR}) + R_{YL}(F_{ZL} + N_{ZL}) \\ & - R_{ZL}(F_{YL} + N_{YL}) + M_{XL} + M_{XR} + M_{XS} \end{aligned} \quad (\text{A.49})$$

**spin equation**

$$\begin{aligned} I_{WY}\ddot{\beta} = & R_{ZR}(F_{XR} + N_{XR}) - R_{XR}(F_{ZR} + N_{ZR}) + R_{ZL}(F_{XL} + N_{XL}) \\ & - R_{XL}(F_{ZL} + N_{ZL}) + M_{YL} + M_{YR} + M_{YS} \end{aligned} \quad (\text{A.50})$$

**yaw equation**

$$\begin{aligned} I_{WZ}\ddot{\psi} + I_{WY}\Omega\dot{\phi} = & R_{YR}(F_{YR} + N_{YR}) - R_{YR}(F_{XR} + N_{XR}) + R_{XL}(F_{YL} + N_{YL}) \\ & - R_{YL}(F_{XL} + N_{XL}) + M_{ZL} + M_{ZR} + M_{ZS} \end{aligned} \quad (\text{A.51})$$

For the purpose of getting  $N_L$  and  $N_R$ , the vertical (A.48) and the roll (A.49) equations are re-arranged

$$N_{ZL} + N_{ZR} = M\ddot{z} - F_{ZL} - F_{ZR} - F_{ZS} \quad (\text{A.52})$$

$$N_{ZR}R_{YR} - N_{YR}R_{ZR} + N_{ZL}R_{YL} - N_{YL}R_{ZL} = I_{WX}\ddot{\phi} - I_{WY}\Omega\dot{\psi}$$

$$-R_{YR}F_{ZR} + R_{ZR}F_{YR} - R_{YL}F_{ZL} + R_{ZL}F_{YL} - M_{XL} - M_{XR} - M_{XS} \quad (A.53)$$

By substituting the components of the normal forces, (A.39) and (A.41), into (A.52) and (A.53), eq. (A.52) and (A.53) become

$$N_L \cos(\delta_L + \phi) + N_R \cos(\delta_R - \phi) = F_Z^* \quad (A.54)$$

$$N_L [R_{YL} \cos(\delta_L + \phi) + R_{ZL} \sin(\delta_L + \phi) \cos \psi] \\ + N_R [R_{YR} \cos(\delta_R - \phi) - R_{ZR} \sin(\delta_R - \phi) \cos \psi] = M_\Phi^* \quad (A.55)$$

where

$$F_Z^* = M\ddot{z} - F_{ZL} - F_{ZR} - F_{ZS} \quad (A.56)$$

$$M_\Phi^* = I_{WX}\ddot{\phi} - I_{WY}\Omega\dot{\psi} - R_{YR}F_{ZR} + R_{ZR}F_{YR} - R_{YL}F_{ZL} + R_{ZL}F_{YL} \\ - M_{XL} - M_{XR} - M_{XS} \quad (A.57)$$

So  $N_L$  and  $N_R$  can be solved,

$$N_L = \frac{1}{\Delta} \begin{vmatrix} F_Z^* & \cos(\delta_R - \phi) \\ M_\Phi^* & [R_{YR} \cos(\delta_R - \phi) - R_{ZR} \sin(\delta_R - \phi) \cos \psi] \end{vmatrix} \quad (A.58)$$

$$N_R = \frac{1}{\Delta} \begin{vmatrix} \cos(\delta_L + \phi) & F_Z^* \\ [R_{YL} \cos(\delta_L + \phi) + R_{ZL} \sin(\delta_L + \phi) \cos \psi] & M_\Phi^* \end{vmatrix} \quad (A.59)$$

where

$$\Delta = \begin{vmatrix} \cos(\delta_L + \phi) & \cos(\delta_R - \phi) \\ [R_{YL} \cos(\delta_L + \phi) + R_{ZL} \sin(\delta_L + \phi) \cos \psi] & [R_{YR} \cos(\delta_R - \phi) - R_{ZR} \sin(\delta_R - \phi) \cos \psi] \end{vmatrix} \quad (A.60)$$

In order to obtain the wheelset external force and moment, the lateral and yaw equations is considered, and the following components are interested

$$N_L \cos(\delta_L + \phi) = \frac{[-R_{YR} + R_{ZR} \tan(\delta_R - \phi) \cos \psi] \dot{F}_Z + M_\phi}{R_{YL} - R_{YR} + [R_{ZR} \tan(\delta_R - \phi) + R_{ZL} \tan(\delta_L + \phi)] \cos \psi} \quad (\text{A.61})$$

$$N_R \cos(\delta_R - \phi) = \frac{[R_{YL} + R_{ZL} \tan(\delta_L + \phi) \cos \psi] \dot{F}_Z - M_\phi}{R_{YL} - R_{YR} + [R_{ZR} \tan(\delta_R - \phi) + R_{ZL} \tan(\delta_L + \phi)] \cos \psi} \quad (\text{A.62})$$

From the position vectors,  $\vec{R}_R$  and  $\vec{R}_L$ , assuming small  $\phi, \psi, \delta_R, \delta_L$ ,

$$\vec{R}_R = (A\psi) \vec{i}''' + (-A - \Delta_R + R_R\phi) \vec{j}''' + (-A\phi - R_R) \vec{k}''' \quad (\text{A.63})$$

$$\vec{R}_L = (-A\psi) \vec{i}''' + (A - \Delta_L + R_L\phi) \vec{j}''' + (A\phi - R_L) \vec{k}''' \quad (\text{A.64})$$

Furthermore, the vertical motion is assumed vanishingly, i.e.,  $\ddot{z} = 0$ . The roll and yaw motion can be neglected, i.e.,  $(\ddot{\phi}, \ddot{\psi}) = 0$ . There is no creep force at Z-direction, i.e.,  $(F_{ZL}, F_{ZR}) = 0$ . There is no creep moment at X- and Y-direction, i.e.,  $(M_{XL}, M_{YL}, M_{XR}, M_{YR}) = 0$ . Hence eq.(A.56) and (A.57) become

$$\dot{F}_Z = W_A - F_{ZS} \quad (\text{A.65})$$

$$M_\phi = A\phi(F_{YL} - F_{YR}) - (R_R F_{YR} + R_L F_{YL}) \quad (\text{A.66})$$

By substituting (A.65) and (A.66) into (A.61) and (A.62) and using the fact that  $A \gg \Delta_L$ ,  $A \gg \Delta_R$ ,  $F_{ZS} = 0$  and  $M_{XS} = 0$  at equilibrium, eq. (A.61) and (A.62) become

$$N_L \cos(\delta_L + \phi) \approx \frac{W_A}{2} + \frac{\phi}{2} (F_{YL} - F_{YR}) - \frac{1}{2A} (R_R F_{YR} + R_L F_{YL}) \quad (\text{A.67})$$

$$N_R \cos(\delta_R - \phi) \approx \frac{W_A}{2} - \frac{\phi}{2} (F_{YL} - F_{YR}) + \frac{1}{2A} (R_R F_{YR} + R_L F_{YL}) \quad (\text{A.68})$$

Similarly,

$$N_L \sin(\delta_L + \phi) \approx \frac{W_A}{2} - \frac{1}{2A} (R_R F_{YR} + R_L F_{YL})(\delta_L + \phi) \quad (A.69)$$

$$N_R \sin(\delta_R - \phi) \approx \frac{W_A}{2} - \frac{1}{2A} (R_R F_{YR} + R_L F_{YL})(\delta_R - \phi) \quad (A.70)$$

and the gravitational force is defined as,

$$\begin{aligned} F_g &= -N_R \sin(\delta_R - \phi) + N_L \sin(\delta_L + \phi) \\ &= [W_A - \frac{1}{A} (R_R F_{YR} + R_L F_{YL})] (\frac{\delta_L - \delta_R}{2} + \phi) \end{aligned} \quad (A.71)$$

Cooperrider et al.(1975) indicated that the gravitational force has a positive effect on train stability.

By substituting the components of the forces (eq. (A.24) - (A.45)) and assuming small angle, the lateral equation (A.47) becomes

$$\begin{aligned} M\ddot{y} &= (F'_{XL} + F'_{XR})\psi + (F'_{YL} + F'_{YR}) \\ &\quad - [W_A - \frac{1}{A} (R_R F_{YR} + R_L F_{YL})] (\frac{\delta_L - \delta_R}{2} + \phi) + F_{YS} \end{aligned} \quad (A.72)$$

Because  $\frac{1}{A} (R_R F'_{YR} + R_L F'_{YL})$  is relatively smaller than  $W_A$ , the lateral equation becomes

$$M\ddot{y} = (F'_{XL} + F'_{XR})\psi + (F'_{YL} + F'_{YR}) - W_A (\frac{\delta_L - \delta_R}{2} + \phi) + F_{YS} \quad (A.73)$$

By operating the similar substitution and assumption, the yaw equation (A.48) becomes

$$\begin{aligned} I_{WZ}\ddot{\psi} + I_{WY}\Omega\dot{\phi} &= F'_{XR}(A + \Delta_R - R_R\phi) - F'_{XL}(A - \Delta_L + R_L\phi) + A\psi W_A \frac{\delta_L + \delta_R}{2} \\ &\quad + M'_{ZL} + M'_{ZR} + M_{ZS} \end{aligned} \quad (A.74)$$

From the lateral (A.73) and yaw (A.74) equations, the wheelset external force,  $F_{ext}$ , and the wheelset external moment,  $M_{ext}$ , can be defined respectively.

$$F_{ext} = (F'_{XL} + F'_{XR})\psi + (F'_{YL} + F'_{YR}) - W_A \left( \frac{\delta_L - \delta_R}{2} + \phi \right) \quad (A.75)$$

in which the first two terms are due to the creep forces and the last term is due to the normal force.

$$M_{ext} = F'_{XR}(A + \Delta_R - R_R\phi) - F'_{XL}(A - \Delta_L + R_L\phi) + M'_{ZL} + M'_{ZR} \\ + A\psi W_A \frac{\delta_L + \delta_R}{2} \quad (A.76)$$

in which the last term is due to the normal force, and the others are due to the creep forces or moments.

## Appendix B. Derivation of Creepage and Spin for a Wheelset

This appendix derives the expression of the creepages for a wheelset including the right and left wheels. The notation are the same as those in Appendix A. The coordinate system of the wheelset is shown in Fig. 48.

As defined in eq. (2.1) - (2.3), the **longitudinal creepage** in the body coordinates is

$$\zeta'_X = \frac{V'_{WX} - V'_{TX}}{V} \quad (B.1)$$

The **lateral creepage** in the body coordinates is

$$\zeta'_Y = \frac{V'_{WY} - V'_{TY}}{V} \quad (B.2)$$

The **spin creepage** in the body coordinates is

$$\zeta'_{SP} = \frac{\omega'_{WZ} - \omega'_{TZ}}{V} \quad (B.3)$$

where

- $V'_{wx}$  = lateral velocity of wheel
- $V'_{wy}$  = lateral velocity of wheel
- $V'_{wy}$  = lateral velocity of wheel
- $V'_{ry}$  = lateral velocity of rail
- $\omega'_{wz}$  = angular velocity of wheel in vertical direction
- $\omega'_{tz}$  = angular velocity of rail in vertical direction
- $V$  = nominal velocity

The position vector of the contact point at the left wheel is

$$\vec{R}'_L = x\vec{i}''' + y\vec{j}''' + z\vec{k}''' + (A - \Delta_L)\vec{j}' - R_L\vec{k}' \quad (B.4)$$

$$\begin{aligned} &= [x - (A - \Delta_L) \cos \phi \sin \psi - R_L \sin \phi \sin \psi] \vec{i}''' \\ &\quad + [y + (A - \Delta_L) \cos \phi \cos \psi + R_L \sin \phi \cos \psi] \vec{j}''' \\ &\quad + [z + (A - \Delta_L) \sin \phi - R_L \cos \phi] \vec{k}''' \end{aligned} \quad (B.5)$$

By differentiating the position vector, the velocity of the left wheel is obtained

$$\begin{aligned} \vec{V}_{WL} &= [\dot{x} - (A - \Delta_L)\dot{\psi} \cos \phi \cos \psi] \vec{i}''' + [\dot{y} + R_L\dot{\phi} \cos \phi \cos \psi] \vec{j}''' \\ &\quad + [\dot{z} + (A - \Delta_L)\dot{\phi} \cos \phi] \vec{k}''' \end{aligned} \quad (B.6)$$

$$= V'_{wXL} \vec{i}''' + V'_{wYL} \vec{j}''' + V'_{wZL} \vec{k}''' \quad (B.7)$$

The velocity of left rail at the contact point is

$$\vec{V}_{TL} = \left(\frac{V}{R_0} + \dot{\beta}\right) R_L \vec{i}''' = \left(\frac{V}{R_0} + \dot{\beta}\right) R_L \cos \psi \vec{i}' = V'_{TXL} \vec{i}' \quad (B.8)$$

By substituting eq. (B.7) and (B.8) into eq. (B.1) and (B.2), the **longitudinal and lateral creepages** at the left wheel are obtained

$$\zeta'_{XL} = \frac{V'_{WXL} - V'_{TXL}}{V} = \frac{\vec{V}_{WL} \cdot \vec{e}_{1L} - V'_{TXL}}{V} \quad (B.9)$$

$$= \frac{1}{V} \left[ V \left( 1 - \frac{R_L}{R_0} \right) - \dot{\beta} R_L \cos \psi - (A - \Delta_L) \dot{\psi} \cos \phi \cos \psi \right] \cos \psi \quad (B.10)$$

$$\zeta'_{YL} = \frac{V'_{WYL} - V'_{TYL}}{V} = \frac{\vec{V}_{WL} \cdot \vec{e}_{2L} - 0}{V} \quad (B.11)$$

$$= \left( \frac{1}{V} \right) [\dot{y} \cos \psi + R_L \cos \phi \cos^2 \psi \dot{\phi} - \dot{x} \sin \psi] \cos(\delta_L + \phi) \\ + \left( \frac{1}{V} \right) [\dot{z} + (A - \Delta_L) \dot{\phi} \cos \phi] \sin(\delta_L + \phi) \quad (B.12)$$

To find the spin creepage, the angular velocity of the wheelset (A.7) is recalled

$$\vec{\omega}_W = \dot{\phi} \vec{i}' + (\Omega + \dot{\beta} + \dot{\psi} \sin \phi) \vec{j}' + \dot{\psi} \cos \phi \vec{k}' \quad (B.13)$$

and the rail angular velocity is zero for tangent track.

$$\vec{\omega}_T = 0 \quad (B.14)$$

Then, substituting (B.13) and (B.14) into (B.3), the **spin creepage** for the left wheel is

$$\zeta'_{SPL} = \frac{\vec{\omega}_W \cdot \vec{e}_{3L}}{V} \quad (B.15)$$

$$= \frac{1}{V} [\dot{\psi} \cos(\delta_L + \phi) - \Omega \sin \delta_L] \quad (B.16)$$

When assuming small angle and neglecting the higher-order term, the creepages of the left wheel, eq. (B.10), (B.12) and (B.16), become

$$\xi'_{XL} = \frac{1}{V} \left\{ V \left[ 1 - \left( \frac{R_L}{R_0} \right) \right] - \dot{\beta} R_L - A \dot{\psi} \right\} \quad (B.17)$$

$$\xi'_{YL} = \frac{1}{V} \{ \dot{y} + R_L \dot{\phi} - V \psi \} \quad (B.18)$$

$$\xi'_{SPL} = \frac{1}{V} \{ \dot{\psi} - \Omega \delta_L \} \quad (B.19)$$

Notice that  $\xi'_{XL}$ ,  $\xi'_{YL}$  and  $\xi'_{SPL}$  are the input data of the program FASTSIM, they are used to determine the creep forces and moment ( $F'_{XL}$ ,  $F'_{YL}$ ,  $M'_{ZL}$ ) (see Section 2.4 for detail). Similarly, the creepages,  $\xi'_{XR}$ ,  $\xi'_{YR}$  and  $\xi'_{SPR}$ , for the right wheel can be obtained by the following procedures. The position vector of the contact point at the right wheel is

$$\vec{R}'_R = x \vec{i}''' + y \vec{j}''' + z \vec{k}''' - (A + \Delta_R) \vec{j}' - R_R \vec{k}' \quad (B.20)$$

$$\begin{aligned} &= [x + (A + \Delta_R) \cos \phi \sin \psi - R_R \sin \phi \sin \psi] \vec{i}''' \\ &\quad + [y - (A + \Delta_R) \cos \phi \cos \psi + R_R \sin \phi \cos \psi] \vec{j}''' \\ &\quad + [z - (A + \Delta_R) \sin \phi - R_R \cos \phi] \vec{k}''' \end{aligned} \quad (B.21)$$

The velocity of right wheel at contact point is

$$\begin{aligned} \vec{V}_{WR} &= [\dot{x} - (A + \Delta_R) \dot{\psi} \cos \phi \cos \psi] \vec{i}''' + [\dot{y} + R_R \dot{\phi} \cos \phi \cos \psi] \vec{j}''' \\ &\quad + [\dot{z} - (A + \Delta_R) \dot{\phi} \cos \phi] \vec{k}''' \end{aligned} \quad (B.22)$$

$$= V'_{WXR} \vec{i}''' + V'_{WYR} \vec{j}''' + V'_{WZR} \vec{k}''' \quad (B.23)$$

The velocity of right rail at contact point is

$$\vec{V}_{TR} = \left( \frac{V}{R_0} + \dot{\beta} \right) R_R \vec{i}''' = \left( \frac{V}{R_0} + \dot{\beta} \right) R_R \cos \psi \vec{i}' = V'_{TXR} \vec{i}' \quad (B.24)$$

Substitution of eq. (B.21) - (B.24) into eq. (B.1) - (B.3), the creepages for the right wheel can be derived

$$\xi'_{XR} = \frac{V'_{WXR} - V'_{TXR}}{V} = \frac{\vec{V}_{WR} \cdot \vec{e}_{1R} - V'_{TXR}}{V} \quad (B.25)$$

$$= \frac{1}{V} \left\{ \left[ V \left( 1 - \frac{R_R}{R_0} \cos \psi \right) + (A + \Delta_R) \dot{\psi} \cos \phi \cos \psi \right] \cos \psi \right\} \quad (B.26)$$

$$\xi'_{YR} = \frac{V'_{WYR} - V'_{TYR}}{V} = \frac{\vec{V}_{WR} \cdot \vec{e}_{2R} - 0}{V}$$

$$= \left( \frac{1}{V} \right) \left[ \dot{y} \cos \psi + R_R \cos \phi \cos^2 \psi \dot{\phi} - \dot{x} \sin \psi \right] \cos(\delta_R - \phi) \\ - \left( \frac{1}{V} \right) \left[ \dot{z} + (A + \Delta_R) \dot{\phi} \cos \phi \right] \sin(\delta_L - \phi) \quad (B.27)$$

$$\xi'_{SPR} = \frac{\vec{\omega}_W \cdot \vec{e}_{3R}}{V} = \frac{1}{V} \left[ \dot{\psi} \cos(\delta_R - \phi) + \Omega \sin \delta_R \right] \quad (B.28)$$

When assuming small angle and neglecting the higher-order term, the creepages of the right wheel become

$$\xi'_{XR} = \frac{1}{V} \left\{ V \left[ 1 - \left( \frac{R_R}{R_0} \right) \right] - \dot{\beta} R_R + A \dot{\psi} \right\} \quad (B.29)$$

$$\xi'_{YR} = \frac{1}{V} \left\{ \dot{y} + R_R \dot{\phi} - V \psi \right\} \quad (B.30)$$

$$\xi'_{SPR} = \frac{1}{V} \left\{ \dot{\psi} + \Omega \delta_R \right\} \quad (B.31)$$

## Appendix C. Derivation of Equations of Motion for the 5 d.o.f. Half-Car Model

This appendix discusses the derivation of the equations of motion for the 5-degree-of-freedom half-car model from Lagrange's equation. The kinetic energy, potential energy, dissipative energy and generalized forces are obtained, then they are substituted into Lagrange's equation to derive equations of motion.

Lagrange's equation is as follows

$$\frac{d}{dt} \left( \frac{\partial T}{\partial \dot{q}_i} \right) - \left( \frac{\partial T}{\partial q_i} \right) + \frac{\partial V}{\partial q_i} + \frac{\partial D}{\partial \dot{q}_i} = Q_{q_i} \quad (C.1)$$

where

- $T$  = kinetic energy
- $V$  = potential energy
- $D$  = dissipative energy
- $q_i$  = generalized coordinates ( $Y_T, \Psi_T, \Psi_W, Y_C, \Phi_C$ )
- $Q_{q_i}$  = generalized forces

## Kinetic Energy

$$T = \sum_{i=1}^N \left\{ \frac{1}{2} m_i \vec{R}_{G_i} \cdot \vec{R}_{G_i} + \frac{1}{2} \vec{\omega}_i^T \cdot [I]_i^G \cdot \vec{\omega}_i \right\} \quad (C.2)$$

where

- $T$  = total kinetic energy
- $N$  = number of the rigid bodies
- $m_i$  = mass of the rigid body  $i$
- $\vec{R}_{G_i}$  = velocity of the c.g. of the rigid body  $i$
- $\vec{\omega}_i$  = angular velocity of the rigid body  $i$
- $[I]_i^G$  = moment of inertia of the rigid body  $i$  with respect to its c.g.

kinetic energy of wheelsets:

$$T_W = \frac{1}{2} M_W [(\dot{Y}_T + L\dot{\Psi}_T)^2 + (\dot{Y}_T - L\dot{\Psi}_T)^2] + \frac{1}{2} (2I_{WZ})(\dot{\Psi}_T + \dot{\Psi}_W)^2 \quad (C.3)$$

kinetic energy of sideframes:

$$T_F = \frac{1}{2} (2M_F)\dot{Y}_T^2 + \frac{1}{2} (2M_F)D^2\dot{\Psi}_W^2 + \frac{1}{2} (2I_{FZ})\dot{\Psi}_T^2 \quad (C.4)$$

kinetic energy of bolster:

$$T_B = \frac{1}{2} (M_B)(\dot{Y}_C + H_2\dot{\Phi}_C)^2 + \frac{1}{2} I_{BZ}(\dot{\Psi}_T + \dot{\Psi}_W)^2 + \frac{1}{2} I_{BX}\dot{\Phi}_C^2 \quad (C.5)$$

kinetic energy of car body:

$$T_C = \frac{1}{2} \left( \frac{M_C}{2} \right) \dot{Y}_C^2 + \frac{1}{2} \left( \frac{I_{CX}}{2} \right) \dot{\Phi}_C^2 \quad (C.6)$$

the total kinetic energy:

$$T = T_W + T_F + T_B + T_C \quad (C.7)$$

$$\frac{d}{dt} \left( \frac{\partial T}{\partial \dot{Y}_T} \right) = (2M_W + 2M_F) \ddot{Y}_T \quad (C.8)$$

$$\frac{d}{dt} \left( \frac{\partial T}{\partial \dot{\Psi}_T} \right) = (2M_W L^2 + 2I_{WZ} + 2I_{FZ} + I_{BZ}) \ddot{\Psi}_T + (2I_{WZ} + I_{BZ}) \ddot{\Psi}_W \quad (C.9)$$

$$\frac{d}{dt} \left( \frac{\partial T}{\partial \dot{\Psi}_W} \right) = (2I_{WZ} + I_{BZ}) \ddot{\Psi}_T + (2I_{WZ} + 2M_F D^2 + I_{BZ}) \ddot{\Psi}_W \quad (C.10)$$

$$\frac{d}{dt} \left( \frac{\partial T}{\partial \dot{Y}_C} \right) = \left( M_B + \frac{M_C}{2} \right) \ddot{Y}_C + M_B H_2 \ddot{\Phi}_C \quad (C.11)$$

$$\frac{d}{dt} \left( \frac{\partial T}{\partial \dot{\Phi}_C} \right) = M_B H_2 \ddot{Y}_C + \left( M_B H_2^2 + I_{BX} + \frac{I_{CX}}{2} \right) \ddot{\Phi}_C \quad (C.12)$$

$$\frac{\partial T}{\partial Y_T} = 0 \quad (C.13)$$

$$\frac{\partial T}{\partial \Psi_T} = 0 \quad (C.14)$$

$$\frac{\partial T}{\partial \Psi_W} = 0 \quad (C.15)$$

$$\frac{\partial T}{\partial Y_C} = 0 \quad (C.16)$$

$$\frac{\partial T}{\partial \Phi_C} = 0 \quad (C.17)$$

## Potential Energy

$$V = \sum_{i=1}^M \left\{ \frac{1}{2} K_i \vec{R}_i \cdot \vec{R}_i \right\} + \sum_{i=1}^N \{ m_i g h_i \} \quad (\text{C.18})$$

where

- $V$  = total potential energy
- $M$  = number of the springs
- $K$  = spring constant
- $\vec{R}_i$  = relative displacement of spring  $i$
- $N$  = number of the rigid bodies
- $m_i$  = mass of the rigid body  $i$
- $g$  = gravitational constant
- $h_i$  = elevation of the rigid body  $i$

strain energy due to  $K_{BY}$  :

$$V_{K_{BY}} = \frac{1}{2} (2K_{BY})(Y_T - H_2\Phi_C - Y_C)^2 \quad (\text{C.19})$$

strain energy due to  $K_{BZ}$  :

$$V_{K_{BZ}} = \frac{1}{2} K_{BZ}(\bar{Z}_W + D\Phi_C - D\bar{\Phi}_W)^2 + \frac{1}{2} K_{BZ}(\bar{Z}_W - D\Phi_C + D\bar{\Phi}_W)^2 \quad (\text{C.20})$$

strain energy due to  $K_{B\Psi}$  :

$$V_{K_{B\Psi}} = \frac{1}{2} K_{B\Psi} \Psi_W^2 \quad (\text{C.21})$$

strain energy due to  $K_{C\Psi}$  :

$$V_{K_{C\Psi}} = \frac{1}{2} K_{C\Psi} (\Psi_T + \Psi_W)^2 \quad (\text{C.22})$$

potential energy due to gravity:

$$V_w = (2M_W + 2M_F)g\bar{Z}_W \quad (C.23)$$

the total potential energy:

$$V = V_{K_{BY}} + V_{K_{BZ}} + V_{K_{B\Psi}} + V_{K_{C\Psi}} + V_w \quad (C.24)$$

$$\frac{\partial V}{\partial Y_T} = 2K_{BY}(Y_T - H_2\Phi_C - Y_C) \quad (C.25)$$

$$\frac{\partial V}{\partial \Psi_T} = K_{C\Psi}(\Psi_T + \Psi_W) \quad (C.26)$$

$$\frac{\partial V}{\partial \Psi_W} = K_{C\Psi}\Psi_T + (K_{B\Psi} + K_{C\Psi})\Psi_W \quad (C.27)$$

$$\frac{\partial V}{\partial Y_C} = -2K_{BY}(Y_T - H_2\Phi_C - Y_C) \quad (C.28)$$

$$\frac{\partial V}{\partial \Phi_C} = -2K_{BY}H_2(Y_T - H_2\Phi_C - Y_C) + 2K_{BZ}D^2(\Phi_C - \bar{\Phi}_W) \quad (C.29)$$

### **Dissipative Energy**

$$D = \sum_{i=1}^M \left\{ \frac{1}{2} C_i \vec{R}_i \cdot \vec{R}_i \right\} \quad (C.30)$$

where

$D$  = total dissipative energy

$M$  = number of the dampers

$C$  = damping coefficient

$\vec{R}_i$  = relative velocity of damper  $i$

dissipative energy due to  $C_{BY}$  :

$$D_{C_{BY}} = \frac{1}{2} (2C_{BY})(\dot{Y}_T - H_2\dot{\Phi}_C - \dot{Y}_C)^2 \quad (C.31)$$

dissipative energy due to  $C_{BZ}$  :

$$D_{C_{BZ}} = \frac{1}{2} C_{BZ}(\dot{Z}_W + D\dot{\Phi}_C - D\dot{\Phi}_W)^2 + \frac{1}{2} C_{BZ}(\dot{Z}_W - D\dot{\Phi}_C + D\dot{\Phi}_W)^2 \quad (C.32)$$

dissipative energy due to  $C_{B\Psi}$  :

$$D_{C_{B\Psi}} = \frac{1}{2} C_{B\Psi}\dot{\Psi}_W^2 \quad (C.33)$$

dissipative energy due to  $C_{C\Psi}$  :

$$D_{C_{C\Psi}} = \frac{1}{2} C_{C\Psi}(\dot{\Psi}_T + \dot{\Psi}_W)^2 \quad (C.34)$$

the total dissipative energy:

$$D = D_{C_{BY}} + D_{C_{BZ}} + D_{C_{B\Psi}} + D_{C_{C\Psi}} \quad (C.35)$$

$$\frac{\partial D}{\partial \dot{Y}_T} = 2C_{BY}(\dot{Y}_T - H_2\dot{\Phi}_C - \dot{Y}_C) \quad (C.36)$$

$$\frac{\partial D}{\partial \dot{\Psi}_T} = C_{C\Psi}(\dot{\Psi}_T + \dot{\Psi}_W) \quad (C.37)$$

$$\frac{\partial D}{\partial \dot{\Psi}_W} = C_{C\Psi}\dot{\Psi}_T + (C_{B\Psi} + C_{C\Psi})\dot{\Psi}_W \quad (C.38)$$

$$\frac{\partial D}{\partial \dot{Y}_C} = -2C_{BY}(\dot{Y}_T - H_2\dot{\Phi}_C - \dot{Y}_C) \quad (C.39)$$

$$\frac{\partial D}{\partial \dot{\Phi}_C} = -2C_{BY}H_2(\dot{Y}_T - H_2\dot{\Phi}_C - \dot{Y}_C) + 2C_{BZ}D^2(\dot{\Phi}_C - \dot{\Phi}_W) \quad (C.40)$$

## Generalized Force

$$Q_{q_j} = \sum_{i=1}^N \left\{ \vec{F}_i \cdot \frac{\partial \vec{R}_{A_i}}{\partial q_j} + \vec{M}_{A_i} \cdot \frac{\partial \vec{\omega}_i}{\partial q_j} \right\} \quad (C.41)$$

where

- $Q$  = generalized force
- $N$  = number of the rigid bodies
- $\vec{F}_i$  = total external force on the rigid body  $i$
- $\vec{R}_{A_i}$  = position vector at any point  $A$
- $\vec{M}_{A_i}$  = total external moment about point  $A$
- $\omega_i$  = angular velocity of the rigid body  $i$
- $Q_{q_j}$  = generalized forces ( $Q_{Y_T}$ ,  $Q_{\Psi_T}$ ,  $Q_{\Psi_W}$ ,  $Q_{Y_C}$ ,  $Q_{\Phi_C}$ )

$$Q_{Y_T} = F_f + F_r \quad (C.42)$$

$$Q_{\Psi_T} = (F_f - F_r)L + M_f + M_r \quad (C.43)$$

$$Q_{\Psi_W} = M_f + M_r \quad (C.44)$$

$$Q_{Y_C} = 0 \quad (C.45)$$

$$Q_{\Phi_C} = 0 \quad (C.46)$$

By substituting (3.1)-(3.4) into (C.42)-(C.44), the generalized forces are expressed in terms of the creep forces and moments. The generalized force for the generalized coordinate  $Y_T$ ,

$$Q_{Y_T} = F_{Xfr}(\Psi_W + \Psi_T) + F_{Yfr} - W_A \Phi_{(r+n)} \quad (C.47)$$

where

$$F_{Xfr} = F'_{XLf} + F'_{XRf} + F'_{XLr} + F'_{XRr} \quad (C.48)$$

$$F_{Yfr} = F'_{YLf} + F'_{YRf} + F'_{YLr} + F'_{YRr} \quad (C.49)$$

$$\Phi_{(r+\ell)} = \left( \frac{\delta_{Lr} - \delta_{Rr}}{2} \right) + \Phi_{Wr} + \left( \frac{\delta_{Lf} - \delta_{Rf}}{2} \right) + \Phi_{Wf} \quad (C.50)$$

The generalized force for the generalized coordinate  $\Psi_w$ ,

$$Q_{\Psi_w} = AF_{X(R-L)} + F_{\Delta} - F_{\Phi} + M_{fr}(\Psi_w + \Psi_T) + M_{Zfr} \quad (C.51)$$

where

$$F_{X(R-L)} = F'_{XRf} + F'_{XRr} - F'_{XLf} + F'_{XLr} \quad (C.52)$$

$$F_{\Delta} = F'_{XRf}\Delta_{Rf} + F'_{XRr}\Delta_{Rr} + F'_{XLf}\Delta_{Lf} + F'_{XLr}\Delta_{Lr} \quad (C.53)$$

$$F_{\Phi} = (F'_{XRf}R_{Rf} + F'_{XLf}R_{Lf})\Phi_{Wf} + (F'_{XRr}R_{Rr} + F'_{XLr}R_{Lr})\Phi_{Wr} \quad (C.54)$$

$$M_{fr} = AW_A \left( \frac{\delta_{Lr} + \delta_{Rr}}{2} + \frac{\delta_{Lf} + \delta_{Rf}}{2} \right) \quad (C.55)$$

$$M_{Zfr} = M'_{ZLf} + M'_{ZRf} + M'_{ZLr} + M'_{ZRr} \quad (C.56)$$

The generalized force for the generalized coordinate  $\Psi_T$ ,

$$Q_{\Psi_T} = M_{FF}(\Psi_w + \Psi_T) + AF_{X(R-L)} + LF_{Y(f-r)} + W_A\Phi_{(r-\ell)} + F_{\Delta} - F_{\Phi} + M_{Zfr} \quad (C.57)$$

where

$$F_{Y(f-r)} = F'_{YLf} + F'_{YRf} - F'_{YLr} - F'_{YRr} \quad (C.58)$$

$$F_{X(f-r)} = F'_{XLf} + F'_{XRf} - F'_{XLr} - F'_{XRr} \quad (C.59)$$

$$M_{FF} = M_{fr} + LF_{X(f-r)} \quad (C.60)$$

$$\Phi_{(f-r)} = \left( \frac{\delta_{Lf} - \delta_{Rf}}{2} \right) + \Phi_{Wr} - \left( \frac{\delta_{Lf} - \delta_{Rf}}{2} \right) - \Phi_{Wf} \quad (C.61)$$

By the substitution of partial derivative of kinetic energy (C.8)-(C.17), potential energy (C.25)-(C.29), dissipative energy (C.36)-(C.40), and generalized forces (C.42)-(C.46) into Lagrange's equation (C.1), the equations of motion are obtained

**truck lateral ( $Y_T$ ) :**

$$(2M_W + 2M_F)\ddot{Y}_T + 2C_{BY}(\dot{Y}_T - H_2\dot{\Phi}_C - \dot{Y}_C) + 2K_{BY}(Y_T - H_2\Phi_C - Y_C) = F_f + F_r \quad (C.62)$$

**truck yaw ( $\Psi_T$ ) :**

$$\begin{aligned} (2M_W L^2 + 2I_{WZ} + 2I_{FZ} + I_{BZ})\ddot{\Psi}_T + (2I_{WZ} + I_{BZ})\ddot{\Psi}_W + C_{C\Psi}(\dot{\Psi}_T + \dot{\Psi}_W) + K_{C\Psi}(\Psi_T + \Psi_W) \\ = M_f + M_r + (F_f - F_r)L \end{aligned} \quad (C.63)$$

**truck warp ( $\Psi_W$ ) :**

$$\begin{aligned} (2I_{WZ} + I_{BZ})\ddot{\Psi}_T + (2M_F D^2 + 2I_{WZ} + I_{BZ})\ddot{\Psi}_W + C_{C\Psi}\dot{\Psi}_T + (C_{B\Psi} + C_{C\Psi})\dot{\Psi}_W \\ + K_{C\Psi}\Psi_T + (K_{B\Psi} + K_{C\Psi})\Psi_W = M_f + M_r \end{aligned} \quad (C.64)$$

**car body lateral ( $Y_C$ ) :**

$$\begin{aligned} (M_B + \frac{M_C}{2})\ddot{Y}_C + M_B H_2 \ddot{\Phi}_C - 2C_{BY}(\dot{Y}_T - H_2\dot{\Phi}_C - \dot{Y}_C) \\ - 2K_{BY}(Y_T - H_2\Phi_C - Y_C) = 0 \end{aligned} \quad (C.65)$$

car body roll ( $\Phi_C$ ) :

$$M_B H_2 \ddot{\Phi}_C + (M_B H_2^2 + I_{BX} + \frac{I_{CX}}{2}) \ddot{\Phi}_C - 2C_{BY} H_2 (\dot{Y}_T - H_2 \dot{\Phi}_C - \dot{Y}_C) + 2C_{BZ} D^2 \dot{\Phi}_C - 2K_{BY} H_2 (Y_T - H_2 \Phi_C - Y_C) + 2K_{BZ} D^2 \Phi_C = 2C_{BZ} D^2 \dot{\Phi}_W + 2K_{BZ} D^2 \overline{\Phi}_W \quad (C.66)$$

In order to simplify the equations, the following symbols are defined

$$M_T = (2M_W + 2M_F) \quad (C.67)$$

$$I_{TT} = (2M_W L^2 + 2I_{WZ} + 2I_{FZ} + I_{BZ}) \quad (C.68)$$

$$I_{TW} = (2I_{WZ} + I_{BZ}) \quad (C.69)$$

$$I_{WW} = (2M_F D^2 + 2I_{WZ} + I_{BZ}) \quad (C.70)$$

$$C_{BC} = (C_{B\Psi} + C_{C\Psi}) \quad (C.71)$$

$$K_{BC} = (K_{B\Psi} + K_{C\Psi}) \quad (C.72)$$

$$M_{BC} = (M_B + \frac{M_C}{2}) \quad (C.73)$$

$$I_{CC} = (M_B H_2^2 + I_{BX} + \frac{I_{CX}}{2}) \quad (C.74)$$

$$C_{CC} = (2C_{BY} H_2^2 + 2C_{BZ} D^2) \quad (C.75)$$

$$K_{CC} = (2K_{BY} H_2^2 + 2K_{BZ} D^2) \quad (C.76)$$

then, the equations of motion become

**truck lateral :**

$$M_T \ddot{Y}_T + 2C_{BY}(\dot{Y}_T - H_2 \dot{\Phi}_C - \dot{Y}_C) + 2K_{BY}(Y_T - H_2 \Phi_C - Y_C) = F_f + F_r \quad (C.77)$$

**truck yaw :**

$$I_{TT} \ddot{\Psi}_T + I_{TW} \ddot{\Psi}_W + C_{C\Psi}(\dot{\Psi}_T + \dot{\Psi}_W) + K_{C\Psi}(\Psi_T + \Psi_W) = M_f + M_r + (F_f - F_r)L \quad (C.78)$$

**truck warp :**

$$I_{TW} \ddot{\Psi}_T + I_{WW} \ddot{\Psi}_W + C_{C\Psi} \dot{\Psi}_T + C_{BC} \dot{\Psi}_W + K_{C\Psi} \Psi_T + K_{BC} \Psi_W = M_f + M_r \quad (C.79)$$

**car body lateral :**

$$M_{BC} \ddot{Y}_C + M_B H_2 \ddot{\Phi}_C - 2C_{BY}(\dot{Y}_T - H_2 \dot{\Phi}_C - \dot{Y}_C) - 2K_{BY}(Y_T - H_2 \Phi_C - Y_C) = 0 \quad (C.80)$$

**car body roll :**

$$\begin{aligned} M_B H_2 \ddot{Y}_C + I_{CC} \ddot{\Phi}_C - 2C_{BY} H_2 (\dot{Y}_T - \dot{Y}_C) + C_{CC} \dot{\Phi}_C - 2K_{BY} H_2 (Y_T - Y_C) + K_{CC} \Phi_C \\ = 2C_{BZ} D^2 \overline{\Phi}_W + 2K_{BZ} D^2 \overline{\Phi}_W \end{aligned} \quad (C.81)$$

and the equations of motion are expressed in matrix form,

$$\begin{aligned}
 & \begin{bmatrix} M_T & 0 & 0 & 0 & 0 \\ 0 & I_{TT} & I_{TW} & 0 & 0 \\ 0 & I_{TW} & I_{WW} & 0 & 0 \\ 0 & 0 & 0 & M_{BC} & M_B H_2 \\ 0 & 0 & 0 & M_B H_2 & I_{CC} \end{bmatrix} \begin{bmatrix} \ddot{Y}_T \\ \ddot{\Psi}_T \\ \ddot{\Psi}_W \\ \ddot{Y}_C \\ \ddot{\Phi}_C \end{bmatrix} \\
 & + \begin{bmatrix} 2C_{BY} & 0 & 0 & -2C_{BY} & -2C_{BY}H_2 \\ 0 & C_{C\Psi} & C_{C\Psi} & 0 & 0 \\ 0 & C_{C\Psi} & C_{BC} & 0 & 0 \\ -2C_{BY} & 0 & 0 & 2C_{BY} & 2C_{BY}H_2 \\ -2C_{BY}H_2 & 0 & 0 & 2C_{BY}H_2 & C_{CC} \end{bmatrix} \begin{bmatrix} \dot{Y}_T \\ \dot{\Psi}_T \\ \dot{\Psi}_W \\ \dot{Y}_C \\ \dot{\Phi}_C \end{bmatrix} \\
 & + \begin{bmatrix} 2K_{BY} & 0 & 0 & -2K_{BY} & -2K_{BY}H_2 \\ 0 & K_{C\Psi} & K_{C\Psi} & 0 & 0 \\ 0 & K_{C\Psi} & K_{BC} & 0 & 0 \\ -2K_{BY} & 0 & 0 & 2K_{BY} & 2K_{BY}H_2 \\ -2K_{BY}H_2 & 0 & 0 & 2K_{BY}H_2 & K_{CC} \end{bmatrix} \begin{bmatrix} Y_T \\ \Psi_T \\ \Psi_W \\ Y_C \\ \Phi_C \end{bmatrix} \\
 & = \begin{bmatrix} F_f + F_r \\ M_f + M_r + (F_f - F_r)L \\ M_f + M_r \\ 0 \\ 2C_{BZ}D^2\bar{\Phi}_W + 2K_{BZ}D^2\bar{\Phi}_W \end{bmatrix} \tag{C.82}
 \end{aligned}$$

## References:

AREA (American Railway Engineering Association), 1984, *Manual for Railway Engineering*, Chapter 4.

Archard, J. F., 1953, "Contact and Rubbing of Flat Surfaces", *Journal of Applied Physics*, Vol. 24, pp. 981-988.

Bolton, P. J., 1980, "Wear of BS11 Rail Steels in Rolling/Sliding Contact with Class "D" Type Steels", British Railways Technical Note TNMET21, February.

Bolton, P. J., Clayton, P., 1984, "Rolling-Sliding Wear Damage in Rail and Tyre Steels", *Wear*, Vol. 93, pp. 145-165.

Boocock, D., 1969, "Steady-State Motion of Railway Vehicles on Curved Tracks" *Journal of Mechanical Engineering Science*, Vol. 11, No. 6, December, pp. 556-566.

Carter, F. C., 1926, "On the Action of A Locomotive Driving Wheel", *Proceedings Royal Society*, A(112), pp. 151-157.

Clayton, P., Allery, M. B. P., and Bolton, P. J., 1983, "Surface Damage Phenomena in Rails", *Contact Mechanics and Wear of Rail/Wheel Systems*, University of Waterloo Press, pp. 419-443.

Cooperrider, N. K., Law, E. H., Hull, R., Kadala, P. S., and Tuten, J. M., 1975, "Analytical and Experimental Determination of Wheel Rail Constraint Relationships", FRA-OR&D-76-244, December 30, 1975.

Cooperrider, N. K., Law, E. H., and Fries, R. H., 1981, "Freight Car Dynamics: Field Test Results and Comparison with Theory", FRA report FRA/OR&D-81/46, June.

Czichos, H., 1980, "System Approach to Wear Problems", *Wear Control Handbook*, edited by Peterson, M. B., and Winer, W. O., sponsored by the Research Committee on Lubrication, ASME, New York, pp. 17-34.

Davila, C. 1986, "Prediction of Wheel Wear Profile By Analytical Methods", Master's Thesis, Department of Mechanical Engineering, VPISU, Blacksburg, VA.

Detwiler, P. O. and Nagurka, M. L., 1985, "Track Geometry Modeling for Rail Vehicle Studies", ASME DSC-Vol. 1, November 1985.

Doyle, G. R., 1979, "Conventional Versus Self-Steering Radial Truck for High-Speed Passenger Trains", ASME Report 79-RT-3, ASME/IEEE Joint Railroad Conference, 1979.

Elkins, J. A., Eickhoff, B. M., 1979, "Advances in Non-Linear Wheel/Rail Force Prediction Methods and Their Validation", Presented at the ASME Winter Conference, New York, December.

Elkins, J. A., Jollay, J. P., Leary, J. F., and Rownd, K. C., 1983, "A Generalized Truck Wheel Predictor-Extension From F.A.S.T.", *Proceeding of Economics and Performance of Freight Car Trucks*, October, Montreal, pp. 231-246.

Elkins, J. A., Blader, F. B., and Leary, J. F., 1986, "Interim report on the AAR wheel profile project", Association of American Railroads, Transportation Test Center, September.

Fries, R. H., and Coffey, B. M., 1987, "A State-Space Approach to the Synthesis of Random Vertical and Crosslevel Rail Irregularities". ASME 87-WA/DSC-38.

Garg, V. K., and Dukkipati, R. V., 1984, *Dynamics of Railway Vehicle Systems*, Academic Press, Inc., Orlando, Florida.

Ghonem, H., and Kalousek, J., 1981, "The use of Angle-of-Attack Measurement to Estimate Rail Wear under Steady State Rolling Conditions", Proceedings of the International Conference on Wheel/Rail Load and Displacement Measurement Techniques, Cambridge, Massachusetts, September, pp.13-1 to 13-34.

Heller, R., and Cooperrider, N. K., 1977a, "User's Manual for Asymmetric Wheel and Rail Contact Characterization Program", FRA-ORD-78/05, Dec. 1977 Interim Report.

Heller, R., Tuten, J. M., Kadala, P. S., and Law, E. H., 1977b, "Analog and Digital Computer Simulation of Coulomb Friction", FRA-OR&D-78/05, August 30, 1977.

IMSL Library Reference Manual, 1982, Vol. 1, IMSL LIB-0009, International Mathematical and Statistical Libraries, Inc., Houston, Texas.

Jamison, W. E., 1982, "Wear of Steel in Combined Rolling and Sliding", *ASLE Transaction*, Vol. 25, pp. 71-78.

Kalker, J. J., 1967a, "A Strip Theory for Rolling with Slip and Spin", *Proceedings KNAW*, B70, pp. 10-62.

Kalker, J. J., 1967b, "On the Rolling Contact of Two Elastic Bodies in the Presence of Dry Friction", Ph.D. dissertation, Delft University of Technology, Delft, Netherlands.

Kalker, J. J., 1967c, "On the Rolling Contact of Two Elastic Bodies in the Presence of Dry Friction: Numerical Results", Delft University of Technology, Delft, Netherlands.

Kalker, J. J., 1979, "Survey of Wheel-Rail Rolling Contact Theory", *Vehicle System Dynamics*, Vol. 5, pp. 317-358.

Kalker, J. J., 1982, "A Fast Algorithm for the Simplified Theory of Rolling Contact", *Vehicle System Dynamics*, Vol. 11, pp. 1-13.

Kalkstein, J. L., and Zaremba, L. A., 1981, "Safety Life Cycle Methods for Evaluating Railway Wheelsets", The Aerospace Corporation, 1981

Kalousek, J., Roval, G., and Ghonem, H., 1983, "Lateral Creepage and its Effect on Wear in Rail Wheel Interface", *Contact Mechanics and Wear of Rail/Wheel Systems*, University of Waterloo Press, pp. 373-388.

Knothe, K., and Hung, L. T., 1985, "Determination of the Tangential Stress and the Wear for the Wheel-Rail Rolling Contact Problem", *The Dynamics of Vehicles on Roads and on Tracks: Proceedings of 9th IAVSD Symposium*, Linkoping, Sweden, pp. 264-273.

Kumar, S., and Rao, D. L. Prasanna, 1984, "Wheel-Rail Contact Wear, Work, and Lateral Force for Zero Angle of Attack-A Laboratory Study", *Journal of Dynamic Systems, Measurement, and Control*, Vol. 106, pp. 319-326.

Kumar, S., Krishnamoorthy, P. K., and Rao, D. L. Prasanna, 1985, "Wheel Rail Wear and Adhesion with and without Sand for A North American Locomotive", *ASME Rail Transportation*, pp. 41-48.

Marcotte, P. P., Caldwell, W. N., and List, H. A., 1978, "Performance Analysis and Testing of a Conventional Three-Piece Freight Car Truck Retrofitted to Provide Axle Steering", ASME Winter Annual Meeting, Dec. 1978. CN Rail Research Internal Report No. 154, Nov.

Marcotte, P. P., Mathewson, K. J. R., and Caldwell, W. N., 1980, "Improved Wheel Tread Profiles for Heavy Freight Vehicles", *Journal of Engineering for Industry* Vol. 102, August, pp. 263-271.

Marcotte, P. P., Mathewson, K. J. R., and Young, R., 1981, "A Practical Model of Rail Vehicle Curve Negotiation", Presented at the 7th Symposium of the IAVSD, Cambridge, UK, September.

McEwen, I. J., Harvey, R. F., 1985, "Full-Scale Wheel-on-Rail Wear Testing: Comparisons with Service Wear and a Developing Theoretical Predictive Method", *ASLE Transaction*, Vol. 41, pp. 80-88.

Nagurka, M. L., Bell, C. E., Hedrick, J. K., and Wormley, D. N. , 1982, "Computational Methods for Rail Vehicle Steady State Curving Analysis", *Computational Methods in Ground Transportation Vehicles*, presented at the Winter Annual Meeting of the ASME, Phoenix, Arizona, November 14-19, pp. 153-179.

Nagurka, M. L., 1983, "Curving Performance of Rail Passenger Vehicles", Doctoral Dissertation, Department of Mechanical Engineering, MIT, Cambridge, Massachusetts, 02139.

Newland, D. E., 1969, "Steering a Flexible Railway Truck on Curved Tracks", *Journal of Engineering for Industry*, ASME Transactions, Series B, Vol. 91, No. 3, August, pp.908-918.

Olver, A. V., Spikes, H. A., and MacPherson, P. B., 1985, "Wear in Rolling Contacts", *Wear of Materials 1985*, presented at the International Conference on Wear of Materials, Vancouver, B.C. Canada, April, pp. 254-272.

Rabinowicz, E., 1980, "Wear Coefficients-Metals", *Wear Control Handbook*, edited by Peterson, M. B., and Winer, W. O., sponsored by the Research Committee on Lubrication, ASME, New York, pp. 475-506.

Roney, M. D., 1983, "Economic Aspects of the Wear of Rail on Canadian Railways", *Contact Mechanics and Wear of Rail/Wheel Systems* , University of Waterloo Press, pp. 271-291.

Shen, Z. Y., Hedrick, J. K., and Elkins, J. A., 1983, "A Comparison of Alternative Creep Force Models for Rail Vehicle Dynamics Analysis", *The Dynamics of Vehicles on roads and on tracks: Proceedings of 8th IAVSD Symposium*, Cambridge, MA, pp. 591-605.

Timoshenko, S. P., and Goodier, J. N., 1970, *Theory of Elasticity*, 3rd Ed., McGraw-Hill Book Company, New York, NY.

Vermeulen, O. J., and Johnson, K. L., 1964, "Contact of Non-spherical Elastic Bodies Transmitting Tangential Forces", *ASME Journal of Applied Mechanics*, Vol. 31, pp. 338-340.

White, R. C., Limbert, D. A., Hedrick, J. K., and Cooperrider, N. K., 1978, "Guideway-Suspension Tradeoffs in Rail Vehicle Systems", Arizona State University Engineering Research Center Report, ERC-R-78035, January 31, 1978.

Wang, B. T., and Fries, R. H., 1988a, "Determination of Creep Force, Moment, and Work Distribution in Rolling Contact with Slip", submitted for presentation at 1988 ASME Winter Annual Meeting.

Wang, B. T., 1988b, "Program Code WWPPVW: the Prediction of Wheel Wear Profiles", Dep. of Mechanical Engineering, Virginia Polytechnic Institute and State University, Blacksburg, VA.

**The vita has been removed from  
the scanned document**